

# **Development and evaluation of an algorithm to optimize the crystal identification of a multi-layered high resolution scintillator**

David Pérez González

Masterarbeit in Physik

vorgelegt der

Fakultät für Mathematik, Informatik und Naturwissenschaften der  
RWTH Aachen

im Juli 2021

angefertigt am

Institute of Experimental Molecular Imaging  
in der Arbeitsgruppe  
Physics of Molecular Imaging

bei

Univ.-Prof. Dr.-Ing. Volkmar Schulz  
Zweitgutachter: PD Dr. rer. nat. Oliver Pooth

# Acknowledgement

Firstly, I would like to thank Prof. Dr. Volkmar Schulz for giving me the opportunity to work in his research group and PD Dr. Oliver Pooth for kindly accepting to be the second proofreader of this thesis.

My special acknowledgment and thanks go to Dr. David Schug for guiding me through the various obstacles that a work of this magnitude entails. In addition, his approach to problems and his continuous drive to achieve the best results have taught me invaluable lessons.

Furthermore, thanks to the whole PMI group for being there, even during a pandemic, to help me with different small problems that otherwise would have delayed the submission of this thesis.

I would also like to mention the remarkable support I have received from my friends in Aachen, who, over the last two years, have become my German family.

My family deserves an extra chapter to thank them for the sacrifice, support and unconditional love they have given me throughout my life. Thank you for constantly reminding me of what is important in this life.

At last, but of course, not least, I would like to dedicate a special and deep gratitude to the support received from Regina Sophia Tieke. She deserves a monument.

# Glossary

<b>APD</b>	avalanche photo-diode
<b>COG</b>	center of gravity
<b>CPM</b>	crystal position map
<b>cps</b>	counts per second
<b>CPU</b>	central processing unit
<b>CT</b>	computed tomography
<b>DCM</b>	dark count map
<b>DCR</b>	dark count rate
<b>DOI</b>	depth of interaction
<b>DPC</b>	digital photon counter
<b>dSiPM</b>	digital silicon-photomultiplier
<b><sup>18</sup>F-FDG</b>	[ <sup>18</sup> F]-Fluorodeoxyglucose
<b>FOV</b>	field of view
<b>FWHM</b>	full width at half maximum
<b>HVD</b>	horizontal vertical diagonal active (=1) or not active (=0) neighbours of main pixel
<b>LOR</b>	line of response
<b>LUT</b>	lookup table
<b>MRI</b>	magnetic resonance imaging
<b>NEMA</b>	National Electrical Manufacturers Association
<b>PET</b>	positron emission tomography
<b>PDPC</b>	Philips Digital Photon Counting
<b>PMT</b>	photomultiplier tube
<b>ROI</b>	region of interest
<b>SiPM</b>	silicon-photomultiplier
<b>SPAD</b>	single photon avalanche diode
<b>TU Delft</b>	Delft University of Technology

# Contents

<b>1</b>	<b>Introduction</b>	<b>1</b>
<b>2</b>	<b>Fundamentals</b>	<b>3</b>
2.1	PET . . . . .	3
2.1.1	Basic principles . . . . .	3
2.1.1.1	Radioactive decay ( $\beta^+$ ) . . . . .	4
2.1.1.2	Annihilation of the Positron . . . . .	5
2.1.1.3	Gamma Interaction with Matter . . . . .	6
2.1.2	Detection of $\gamma$ -Photons . . . . .	8
2.1.2.1	Scintillators . . . . .	8
2.1.2.2	Photo Detectors . . . . .	9
2.1.3	Performance Parameters . . . . .	11
2.1.3.1	Energy Resolution . . . . .	11
2.1.3.2	Coincidence Resolution Time . . . . .	11
2.1.3.3	Image Spatial Resolution . . . . .	12
2.1.3.4	Count Rate Performance . . . . .	12
2.1.3.5	Sensitivity . . . . .	13
2.2	MRI . . . . .	13
2.3	PET/MRI . . . . .	13
<b>3</b>	<b>Hypmed</b>	<b>15</b>
3.1	Basic Idea . . . . .	15
3.2	DOI and Parallax Error . . . . .	17
3.3	DOI-Capable Detectors . . . . .	19
3.3.1	Crystal Identification . . . . .	21
3.3.2	Inter-Crystal Scattering . . . . .	22
<b>4</b>	<b>Materials and Data Compilation</b>	<b>23</b>
4.1	HYPMED Detector . . . . .	23
4.1.1	Scintillator . . . . .	24
4.1.2	Photosensor . . . . .	26
4.1.3	Light Guide and Glue . . . . .	29
4.2	Temperature Control . . . . .	29
4.3	Sources . . . . .	30
4.4	Hardware Control: SPU and DAPS . . . . .	30
4.5	Principles of Data Collection and Pre-Processing . . . . .	31
4.5.1	Sensor Tile Calibration . . . . .	31
4.5.2	Data Collection . . . . .	32
4.5.3	Data Pre-Processing: Center of Gravity . . . . .	33

## CONTENTS

<b>5 Optimization of Crystal Identification</b>	<b>34</b>
5.1 First Measurements: Front Irradiation . . . . .	34
5.1.1 Singles Configuration . . . . .	35
5.1.2 Coincidences Configuration . . . . .	35
5.2 Region of Interests . . . . .	37
5.3 Crystal Identification Algorithm . . . . .	40
5.3.1 Light Accumulation Point Finder . . . . .	41
5.3.2 Crystal Position Map Construction . . . . .	42
5.3.3 Crystal Position Map Tweaking . . . . .	45
5.3.4 Segmentation of Flood Maps: Look Up Table . . . . .	48
5.3.5 Crystal Identification . . . . .	49
5.4 Results and Discussion . . . . .	50
5.5 Conclusion and Outlook . . . . .	55
<b>6 Evaluation of HYPMED detector</b>	<b>56</b>
6.1 Energy Resolution Evaluation . . . . .	56
6.1.1 Energy Calibration . . . . .	56
6.1.2 Energy Resolution . . . . .	59
6.1.3 Results and Discussion . . . . .	61
6.1.4 Conclusion and Outlook . . . . .	63
6.2 Coincidence Resolution Time Evaluation . . . . .	64
6.2.1 Time Difference Calibration . . . . .	64
6.2.2 Coincidence Resolution Time . . . . .	65
6.2.3 Results and Discussion . . . . .	66
6.2.4 Conclusion and Outlook . . . . .	66
6.3 Additional Method and Measurement . . . . .	66
6.3.1 Inter-Crystal Scattering Filter . . . . .	66
6.3.1.1 Results and Discussion . . . . .	67
6.3.1.2 Conclusion and Outlook . . . . .	70
6.3.2 Side Irradiation Measurement . . . . .	70
6.3.2.1 Measurement Setup . . . . .	70
6.3.2.2 Analysis . . . . .	72
6.3.2.3 Results and Discussion . . . . .	72
6.3.2.4 Conclusion and Outlook . . . . .	73
<b>7 Outcome and Outlook</b>	<b>74</b>
7.1 Summary and Conclusion . . . . .	74
7.2 Outlook . . . . .	75
<b>Bibliography</b>	<b>76</b>
<b>A Appendix</b>	<b>82</b>
A.1 Enlarged Figures . . . . .	82
A.1.1 Flood Maps . . . . .	82
A.1.2 CPMs . . . . .	84
A.1.3 Flood map with layered filtered scintillation events . . . . .	86
A.1.4 Optical photon counts for photopeak position . . . . .	88

# Chapter 1

## Introduction

Breast cancer is one of the most common diseases among women [28]. However, early detection and consequent convenient treatment may reduce its lethality and help women to recover faster [28]. Current whole-body imaging techniques may not provide sufficient accuracy to detect early stages of breast cancer. Therefore, new approaches with organ-specific imaging tools are under research to achieve a more precise diagnostic capability [63].

One of the most widely used techniques to detect cancer is positron emission tomography (PET), which is a functional imaging technique. In recent years, its combination with a magnetic resonance imaging (MRI) technique, which provides complementary anatomical information, has proven to be one of the best combined techniques for an early detection of cancer [47].

In light of the above, several entities across Europe, including our working group, decided to create an European project, called HYPMED, to assess the possibility of developing a breast PET insert for a simultaneous PET/MRI system. The breast PET insert consists of two ring-shaped modules with PET detectors covering the breast of the patient.

To obtain images in PET, the positron must be emitted inside the patient to be studied. This requires a positron-emitting compound, which is called a radio-tracer. The positron emitted by the radio-tracer annihilates with an electron close to the location of the radio-tracer. As products of the annihilation, two  $\gamma$ -photons are emitted in opposite directions. PET detectors, which are basically scintillators coupled with photosensors, are placed around the emission point to measure the  $\gamma$ -photons. If their energy and time of arrival are derived, the location of the emission point, i.e. the location of the radio-tracer, can be determined [11].

The selected design of the breast PET insert in HYPMED reduces the possible interference of signals from other parts of the body and enhances the detection of the  $\gamma$ -photons, which increases the sensitivity of the system and reduces the dose of radio-tracers. To increase the spatial resolution, the scintillators may be segmented into smaller crystals [63].

However, due to the size of the insert, the distance the  $\gamma$ -photons travel before interacting within the scintillator crystal, which is called the depth of interaction (DOI), plays an important role in determining the distribution of the radiotracer [38].

Our working group developed a multi-layered high resolution scintillator that aims to return DOI information and thus provides better performance than conventional PET detectors.

In these kind of scintillators, the measured distribution of the scintillation light generated by the  $\gamma$ -photon is used to calculate the 2D coordinates of its interaction position within the scintillator. By gathering sufficient interaction positions, a crystal position map (CPM) based on them can provide a method to identify the most likely crystal with which

the  $\gamma$ -photon interacts [73]. If more than one CPM is generated, an optimization of the crystal identification can be performed and thus the distribution of the radio tracer can be reconstructed more accurately. Furthermore, if the CPMs are automatically generated, a quick evaluation of the detector's performance is possible.

Therefore, the main focus of this thesis is to find an optimal crystal identification algorithm with the help of four different CPMs, which shall be generated automatically, to provide a routine to quickly evaluate the HYPMED detectors.

The main parameters that can be quickly evaluated to assess the performance of a PET detector are the energy resolution and the coincidence resolution time.

To better understand the role of these parameters in PET and the corresponding underlying physics, Chapter 2 describes the fundamental aspects of PET and its technical background. Additionally, this chapter explains briefly the fundamental concepts of the magnetic resonance imaging (MRI) technique and its integration with PET.

In Chapter 3, the HYPMED project is introduced and the importance of DOI and crystal identification on it are discussed.

Chapter 4 describes the materials employed to carry out the necessary measurements for the completion of this thesis' goal. Hereafter, this chapter explains the data acquisition steps and the pre-processing of the collected data.

Subsequent steps to optimize the crystal identification of the HYPMED detector are presented in Chapter 5, while Chapter 6 evaluates its performance by analyzing its energy resolution and its coincidence resolution time.

At last, Chapter 7 concludes with the outcomes and possible outlooks of this thesis.

# Chapter 2

## Fundamentals

This chapter provides an overview about the fundamentals of positron emission tomography (PET) and its corresponding underlying physics. Additionally, the chapter briefly introduces the Magnetic resonance imaging (MRI) technique and its integration with PET.

### 2.1 PET

This section describes the basic principles of PET, the detection of  $\gamma$ -photons in PET and the performance parameters that are important in PET. Further detailed explanations about these topics are to be found in the following references: [3, 11, 49], which are also the main reference sources for this section.

#### 2.1.1 Basic principles

When a positron interacts with an electron, they both annihilate. Subsequently, two  $\gamma$ -photons are emitted in almost exactly opposite directions. The principle of positron emission tomography (PET) is the detection of both  $\gamma$ -photons and the localization of the origin of their emission.

For clinical images to be obtained, radio-tracers are injected into a living body. Radio-tracers are biomolecules labelled with a radionuclide that emits positrons. One of the most widely used radio-tracers is the fluorodeoxyglucose ( $^{18}\text{F}$ -FDG). It is a radioactive labelled glucose that acts as the normal glucose molecule. Since the cancer cells absorb a higher amount of glucose compared to healthy cells, concentrations of FDG are mostly disposed around the tumour [36]. Its lifetime is short (around minutes to hours), which reduces the amount of activity that the living body receives [14].

The emitted positron may encounter an electron in the tissue close to the positron emission point and thus both particles annihilate. In general, the annihilation outputs two  $\gamma$ -photons with the energy of 511 keV, and opposite directions, close to 180° (see Section 2.1.1.2). This expected energy and collinearity are exploited by placing a ring-shaped scanner whose field of view (FOV) surrounds a living body, as shown in Figure 2.1. Usually, the PET scanner is formed by scintillators glued to photo-detectors, which acquire the information about detected  $\gamma$ -photon events (see Section 2.1.2).

## 2.1. PET

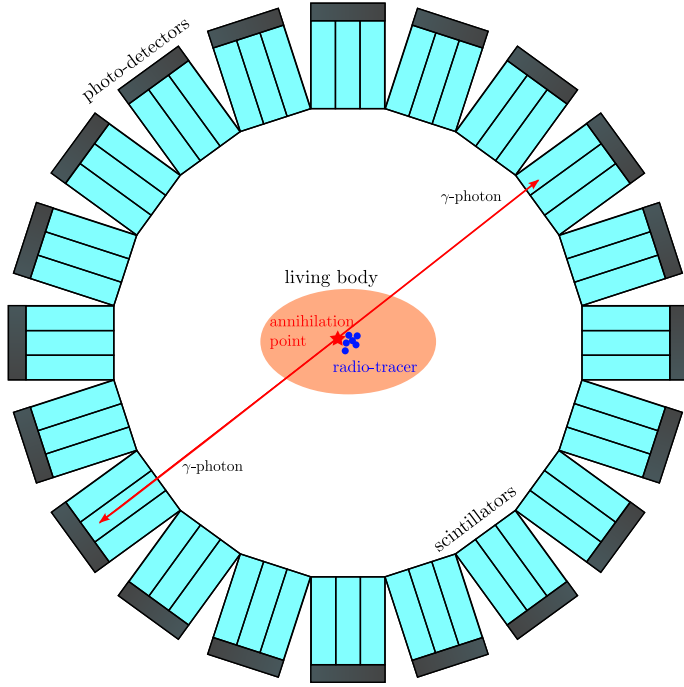


**Figure 2.1:** A sketch of a ring-shaped scanner surrounding a living body. Figure follows discussions and illustrations in [49].

If both  $\gamma$ -photons are detected in coincidence, it is assumed that the annihilation occurred along the line connecting the two points of detection, namely line of response (LOR). Recording several millions of LORs allows to use statistical image reconstruction techniques to calculate the distribution of the radio-tracer in the image space. Thus, the tumour can be localized in the living body.

### 2.1.1.1 Radioactive decay ( $\beta^+$ )

The radio-tracers, which are used in PET, contain a radionuclide that decays per  $\beta^+$  decay. In this case, a proton ( $p$ ) of the radionuclide decays into a neutron ( $n$ ) by emitting a positron ( $e^+$ ) and an electron-neutrino ( $\nu_e$ ), see Equation 2.1.1. A Feynman diagram of this process is shown in Figure 2.2. To understand the theory behind general  $\beta$  decay, an english translation of Fermi's theory for  $\beta$  decay can be found in [18] or [78].

$$p \rightarrow n + e^+ + \nu_e \quad (2.1.1)$$

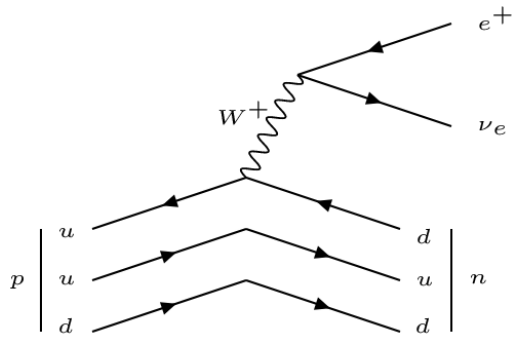


**Figure 2.2:** Feynman diagram of  $\beta^+$  decay: The proton ( $p$ ) decays into a neutron ( $n$ ) by converting an up-quark ( $u$ ) into a down-quark ( $d$ ) via weak interaction with a weak boson ( $W^+$ ) which emits a positron alongside an electronic neutrino ( $\nu_e$ ).

## 2.1. PET

$\beta^+$  decays can only happen with protons belonging to a nucleus. As the mass of a proton is smaller than the mass of a neutron, the required energy to allow the decay is released by the difference in binding energies of the nucleus. In this case, the daughter nucleus must have a greater binding energy than the mother nucleus, which results in a lower total energy. Thus, to describe the decay with nuclei, Equation 2.1.1 can be reformulated as Equation 2.1.2, where  $X$  is the mother nucleus and  $Y$  the daughter nucleus,  $Z$  the number of protons in the nucleus and  $A$  the sum of protons and neutrons.



The energy  $Q$ , which is obtained by this decay, is determined by the difference of masses between the initial nucleus and the final elements. The corresponding equation is shown in 2.1.3, where  $M$  denotes mass and  $c$  the speed of light.

$$\frac{Q}{c^2} = M(X) - M(Y) - M(e^+) - M(\nu_e) \quad (2.1.3)$$

If the transition is not between the ground states of two nuclei, gamma-ray emission from excited states may occur.

As the  $\beta^+$  decay is a three-body decay,  $Q$  is shared between the daughter nucleus and mainly both the positron with rest mass  $511\text{keV}/c^2$  and the electron-neutrino  $\nu_e$  with negligible mass. The kinetic energy is split between positron and neutrino due to the difference in mass with the nucleus. Thus, they both show a continuous energy spectrum with a range from zero up to a maximum endpoint energy  $E_{max}$  equal to  $Q$ . The mean kinetic energy of the emitted positrons is approximately  $0.33 \cdot E_{max}$  [11].

The rate at which nuclei spontaneously undergo radioactive decay is characterized by the parameter called the half-life of the radionuclide  $T_{1/2}$ . Half-life is the time it takes half of the unstable nuclei present to decay. It takes the form of an exponential function as we can see in Equation 2.1.4, where  $N$  is the number of nuclei at time  $t$ , and  $N_0$  the initial number of nuclei at  $t = 0$ .

$$N(t) = N_0 \cdot \left(\frac{1}{2}\right)^{-\frac{t}{T_{1/2}}} = N_0 \cdot e^{-\frac{\ln(2)}{T_{1/2}}t} \quad (2.1.4)$$

By deriving the Equation 2.1.4, the rate of decay of unstable nuclei at any instant in time can be calculated. The obtained Equation 2.1.5 is defined as activity  $A$ .

$$A(t) = \frac{N_0 \cdot \ln(2)}{T_{1/2}} \cdot e^{-\frac{\ln(2)}{T_{1/2}}t} = A_0 \cdot e^{-\frac{\ln(2)}{T_{1/2}}t} \quad (2.1.5)$$

The SI unit for radioactivity is the becquerel (Bq). One becquerel (1 Bq) equals one disintegration per second.

### 2.1.1.2 Annihilation of the Positron

The emitted positron loses kinetic energy due to interactions with the surrounding matter. There are four types of interaction [3]:

1. *Inelastic collisions* with atomic electrons. It is the main process of loss of kinetic energy.
2. *Elastic scattering* with atomic electrons. Momentum and energy are conserved.
3. *Inelastic scattering* with a nucleus. Bremsstrahlung radiation is emitted.
4. *Elastic scattering* with a nucleus. Energy is neither transferred nor radiated.

## 2.1. PET

All interactions deflect the positron path. Therefore, the distance between its emission and the annihilation of the positron and electron is imprecisely measured. This distance, called positron range, lies normally between 1 mm and 10 mm in tissue [11].

Before the annihilation, the positron may combine with an electron to form a metastable intermediate species, which is named positronium [3]. Both particles keep their trajectories near the center of mass and act like a hydrogen atom, but without nucleus. Positronium's lifetime is about 100 ps [3], which delays the emission of  $\gamma$ -photons. However, positronium is formed only in one-third of the times when the positron is in water and human tissue. Hence, direct annihilation is the most likely process on these materials [3].

During annihilation, electromagnetic radiation is emitted. As mentioned before, the most probable radiation form is two  $\gamma$ -photons of 511 keV (the rest-mass equivalent of each particle) with opposite directions, as the momentum of the positron and electron is close to zero. It can involve more than two  $\gamma$ -photons, but this happens only in about 0.003 % of the annihilations [11].

If positron and electron do have a momentum when annihilation occurs, the two  $\gamma$ -photons are not emitted exactly in opposite directions. In water, this happens in around 65 % of the annihilations [3], which contributes to a further uncertainty in the localisation of the nuclear decay event. The angular distribution nearly follows a Gaussian shape with a full width at half maximum (FWHM) of 0.5° and a mean value around 0.25° [52]. This effect is called acollinearity.

Together with the finite distance travelled by the positron before annihilation, acollinearity sets a fundamental lower limit of the spatial resolution that can be achieved in positron emission tomography [39].

### 2.1.1.3 Gamma Interaction with Matter

To reach the detector, the  $\gamma$ -photons must travel through the tissue of the living body. On that path, they may interact with the surrounding matter. Three main interactions may occur: Rayleigh scattering, photoelectric effect and Compton scattering [59]. However, in PET, the latter ones are the most important (see Figure 2.3). Apart from introducing the different interaction types, this section describes the attenuation of the  $\gamma$ -photon beam when travelling through matter.

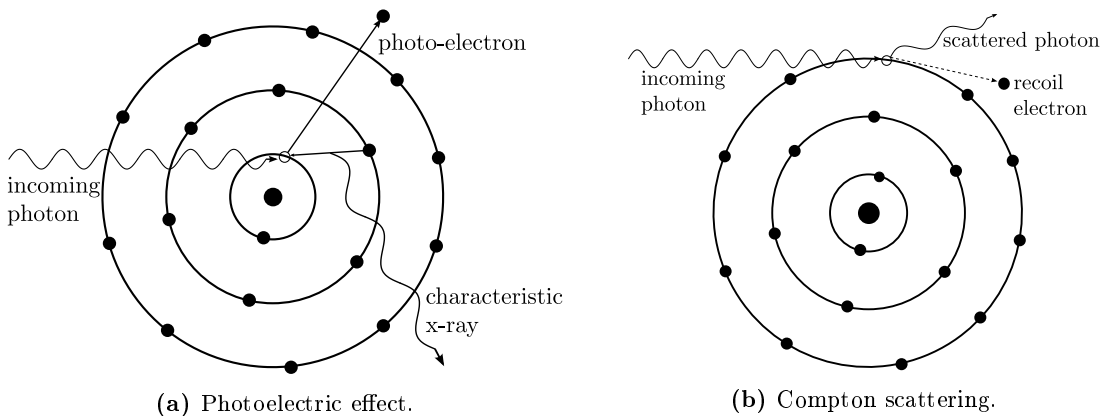


**Figure 2.3:** Important interactions in PET: (a) **Photoelectric effect**. The incoming  $\gamma$ -photon transfers all its energy to the atomic electron which escapes from the atom. (b) **Compton scattering**. Elastic scattering of the incoming  $\gamma$ -photon with an orbital electron. The  $\gamma$ -photon transfers part of its energy to the electron and changes direction due to momentum conservation. Figure follows illustrations in [3].

## 2.1. PET

### Rayleigh scattering [59]

In the first part of Rayleigh scattering (elastic scattering), an incoming  $\gamma$ -photon temporarily excites an electron. When the excited electron drops back to its initial energy level, a  $\gamma$ -photon with the same amount of energy as the incoming  $\gamma$ -photon is emitted. The outgoing  $\gamma$ -photon is slightly deflected with respect to the incoming  $\gamma$ -photon. Events detected in imaging systems due to  $\gamma$ -photons which are Rayleigh-scattered in the patient's body occur more likely with increasing tissue density.

### Photoelectric effect [59]

For the photoelectric effect, the incoming  $\gamma$ -photon interacts with an electron located in the inner shell of an atom. If the  $\gamma$ -photon energy is transferred to the electron and is equal or higher than its binding energy, the electron gets expelled from its shell. Its kinematic energy is then equal to the energy of the  $\gamma$ -photon minus the binding energy of the electron. The kinematic energy of the electron is lost and transferred as it travels through the tissue and interacts with the surrounding matter. The vacancy in the electron shell is immediately filled with another electron from a higher shell. As the higher shell has more energy, some of the intrinsic energy is emitted as a  $\gamma$ -ray with a characteristic energy. Figure 2.3a shows a schematic drawing of the process.

### Compton scattering

Compton scattering is an inelastic interaction in which the incoming  $\gamma$ -photon possesses much more energy than the electron that it interacts with [59]. In this case, the electron belongs to the outer shell of the atom and only receives part of  $\gamma$ -photon's energy. With this energy, a recoil is produced and the electron is ejected forward in comparison with the incoming  $\gamma$ -photon, which changes its direction with any angle. Figure 2.3b shows a schematic drawing of the process.

If the incoming  $\gamma$ -photon has an energy of 511 keV and interacts with tissue or scintillators, Compton scattering is the predominant interaction [52]. Compton scattered  $\gamma$ -photons have less energy than 511 keV when arriving at the detector and can therefore be identified if the energy resolution is good enough. Therefore, it is a significant process in PET.

## Attenuation

The interaction mechanisms discussed so far combine to attenuate the incident  $\gamma$ -photon beam as it passes through matter due to the removal of  $\gamma$ -photons by scattering events [59]. A complete absorption may also be possible and is a further important aspect for scintillation events, which are described in Section 2.1.2.1.

The actual total attenuation of the incident  $\gamma$ -photon intensity is described by an exponential function, as shown in Equation 2.1.6, where  $I(0)$  represents the unattenuated beam intensity,  $I(x)$  the intensity measured after a distance  $x$  in a material and  $\mu$  the attenuation coefficient of the material [3].

$$I(x) = I(0)e^{-\mu x} \quad (2.1.6)$$

Attenuation depends on the electron density of the material and the  $\gamma$ -photon energy. The probability that the  $\gamma$ -photon is attenuated in a material per unit of distance is represented by the attenuation coefficient. For 511-keV  $\gamma$ -photons,  $\mu$  depends mostly on Compton scattering and the photoelectric effect and thus can be defined as in Equation 2.1.7 [11].

$$\mu \approx \mu_{compton} + \mu_{photoelectric} \quad (2.1.7)$$

## 2.1. PET

Since the annihilation occurs,  $\gamma$ -photons must pass through the body (soft tissue and bones), where the most dominant interaction (see Table 2.1) is Compton scattering. Hence, the  $\gamma$ -photons may undergo a change in direction and their energy may be lower. The resulting angular distribution of the detected  $\gamma$ -photons may then be randomized by the scattering process [11]. Hence, scattered  $\gamma$ -photons arriving at the detector may infer an incorrect location for their emission point, which provokes inaccuracies in the reconstructed images. Nonetheless, if the energy of those  $\gamma$ -photons is precisely measured, it is possible to get rid of them. To achieve that, the energy resolution, which is explained in Section 2.1.3.1, must be good enough.

Material	$\mu_{compton}$ [cm $^{-1}$ ]	$\mu_{photoelectric}$ [cm $^{-1}$ ]	$\mu$ [cm $^{-1}$ ]	Half-value thickness [cm]
Soft Tissue	$\sim 0.096$	$\sim 0.00002$	$\sim 0.096$	7.2
Bone	$\sim 0.169$	$\sim 0.001$	$\sim 0.17$	4.1
Lead	0.76	0.89	1.78	0.42
LYSO	$\sim 0.58$	$\sim 0.08$	$\sim 0.68$	$\sim 1.02$

**Table 2.1:** Linear attenuation coefficients and half-value thickness, the thickness of material that is required to cause half of the 511-keV  $\gamma$ -photons to interact, for different materials. Values taken from [11] and [4, 44]. LYSO corresponds to  $Lu_{1.8}Y_{0.2}SiO_5$ , which is the scintillator material used in this thesis.

### 2.1.2 Detection of $\gamma$ -Photons

PET makes use of large transparent and passive components to convert the  $\gamma$ -photons' energy into measurable optical photons. These components are inorganic scintillators [68]. When  $\gamma$ -photons interact with an electron of the scintillator, the electron normally excites other electrons within the scintillator. In this process, optical photons may be emitted. These optical photons are detected using photosensitive sensors, such as, the digital silicon-photomultiplier (dSiPM).

The use of crystals as scintillators and the photo detectors in PET are explained in the following sections, respectively.

#### 2.1.2.1 Scintillators

The main principle of the scintillator crystals is the conversion of  $\gamma$ -photon's energy into optical photons. When a  $\gamma$ -photon interacts with an electron within a crystal, the electron gets excited. Then, they have enough energy  $E_g$  to overcome the gap between the valence band and the empty conduction band of the crystal atoms. As the valence band is the ground state, they try to return by emitting a  $\gamma$ -photon with the same energy as the gap between the two named bands, which is normally in the ultraviolet range.

By adding impurities to a crystal, a process named doping, extra energy states between the two bands in some of the atoms are created. The new energy states are still close to the bands. As shown in Figure 2.4, the energy of the emitted  $\gamma$ -photon  $E_\gamma$  is lower than the energy gap. Thus, the so-called optical photons, or visible light, do not have enough energy to excite again an electron into the conduction band of an atom without impurities. Therefore, to reduce the possible absorption of these optical photons in the scintillator, the amount of impurities is relatively low [3].

## 2.1. PET

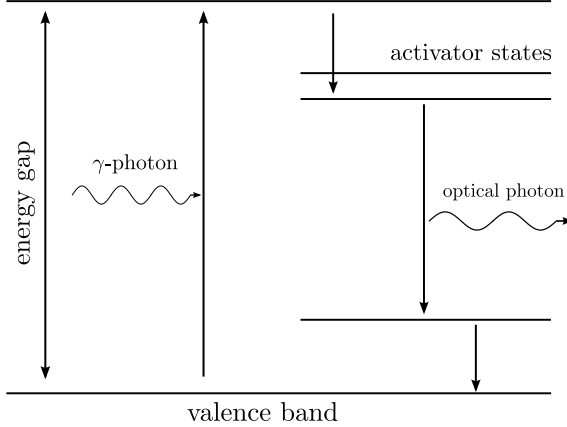


**Figure 2.4:** Schematic drawing of the scintillation mechanism in a doped inorganic scintillator. An energy gap  $E_g$  of some eV is separating the valence band of the conduction band. Figure follows illustrations in [3].

If the material's density or atomic number ( $Z$ ) is high, more  $\gamma$ -photons are stopped along the crystal and can be detected. Hence, a high stopping power in the selected material is desirable to obtain a better sensitivity. Another useful property for the material of the crystals is a short scintillation decay time, which reduces the random coincidence events (see Section 2.1.3.4) and thus increases the signal-to-noise ratio [3, 52]. Furthermore, to ensure a good spatial and energy resolutions, a high light-output is preferred, i.e. each  $\gamma$ -photon shall generate a large number of optical photons and thus more events may be detected in the photo detector (larger sensitivity) [3].

Additionally, the energy resolution depends on how regular the optical photons are spread over the photo detector. Thus, an homogeneous crystal is also a required property for the scintillator to obtain a good energy resolution [3].

Different kinds of materials are suitable to be scintillator crystals. However, as stated in [1], the most commonly employed scintillation materials nowadays are cerium doped lutetium-oxyorthosilicate (LSO) and lutetium-yttrium-oxyorthosilicate (LYSO). Their physical properties, such as a short decay time, a high light output and a high linear attenuation coefficient have proven to be ideal to detect 511 keV  $\gamma$ -photons.

### 2.1.2.2 Photo Detectors

The generated optical photons are detected using photosensitive sensors, also called photo detectors. They are divided mainly into two categories: the photo-multiplier tubes (PMTs) and the semiconductor-based photodiodes.

In PMTs, the incoming optical photons are absorbed in a thin photo-cathode layer situated at the entrance window of the detector. Due to the photoelectric effect, photo-electrons are produced. Then, they are guided through a vacuum enclosed tube to impact with dynodes. These dynodes generate more photo-electrons, which amplify the generated current. They are disposed in sequence to guide the photo-electrons towards the final dynode, which is the anode.  $10^6$  photo-electrons per each initial photo-electron reach the anode and then the signal is recorded.

Thanks to the mentioned gain, the signal-to-noise ratio is very good in PMTs. However, their low (around 15 % to 25 %) quantum efficiency (QE), which is the ratio of photo-electrons produced in the photo-cathode per detected optical photon, had always encouraged the research of other photo detectors [3, 11].

The semiconductor-based photodiodes employ p-n junctions. Following the description given in [60], this structure is based on positively (p-) and negatively (n-)doped semiconductors which are brought into direct contact. After the electrons of the conduction band

## 2.1. PET

from the n-doped semiconductor have filled the holes of the valence band from the p-doped semiconductor, there is a region near the interface where no free carriers are available. This is known as the depletion region (see Figure 2.5). When some voltage is applied to the p-n junction, the diode can be biased to allow current to flow through the junction easily in one direction (forward), but not easily (with very high resistance) in the other direction (reverse) [60].

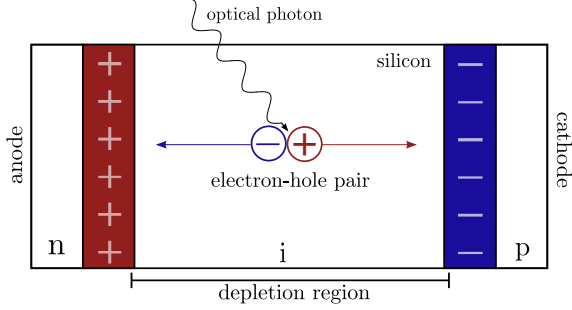


**Figure 2.5:** Schematic diagram of a silicon-PIN-diode. Figure follows discussions and illustrations in [11, 52, 60].

The process to detect an optical photon is as follows [60]. An optical photon reaches the depletion region and deposits its energy. This extra energy provokes that an electron can be released. Therefore, an electron-hole pair is considered. As they have opposite charges, they move towards the opposite charged areas of the diode. This action produces a drop of the electric field that can be measured to determine the number of detected optical photons.

The quantum efficiency of photodiodes is approximately 60 % to 80 % [11], providing a much more efficient conversion of optical photons to electrons than what is possible with PMTs. However, photodiodes have no internal gain, producing only one detected electron-hole pair per optical photon. Therefore, the signal-to-noise ratio is very low, leading to long integration times.

To overcome this problem, the photodiode is modified to apply a much higher voltage across it. In consequence, the electron of the electron-hole pair gains enough energy to release further electrons. This leads to an avalanche effect, which is why they are named avalanche photodiodes (APDs). Amplifications are typically around  $1 \times 10^2$  to  $1 \times 10^3$  [11].

The use and development of APDs for medical applications has increased during the last years [6]. Nowadays, one of the reference detectors in PET is the silicon-photomultiplier (SiPM).

SiPMs consist of a few thousand single-photon avalanche diodes (SPADs) operating above their breakdown voltage [52]. This operation mode is known as Geiger-mode and it causes a self-sustaining avalanche.

To detect further optical photons, each SPAD has to be reset actively or passively (active or passive quenching) [52]. In analog SiPMs (aSiPMs), passive quenching is achieved by a serial high-ohmic resistance. After the avalanche is stopped, the bias voltage recovers to its original value and the SPAD is sensitive again. A single optical photon produces a binary signal in a SPAD. To cover a large region of detection, several small-area SPADs are placed together in an array to count the optical photons in the respective region. This sensitive array is employed to record a signal that is proportional to the number of optical photons [52].

The recorded analogue signal of all SPADs is summed up and then digitized by an application specific integrated circuit (ASIC) [52]. In this process, the temperature can affect the final recorded signal. Moreover, the internal gain of a SPAD is approximately equal in every avalanche and much higher than that of APDs. In addition, its signal is

## 2.1. PET

very fast, which entails the consideration of SPADs as trigger devices that detect optical photons in a binary mode.

The digital SiPM (dSiPM) takes advantage of the last described property of SPADs. In each SPAD, the signal of the breakdown is binarily digitized and the quenching circuitry is adapted to be able to keep the SPAD in the quenched state [52]. The dark count rate (DCR) of the individual SPADs can be measured thanks to the latter feature. Therefore, a DCR map with all SPADs can be generated to deactivate the SPADs with the highest DCR. Although the sensitivity is slightly lower, the benefit of reducing the DCR is higher [52].

The most important benefits of SiPMs with respect to PMTs are their compact size, their high photon detection efficiency, low operating voltage, and their insensitivity to magnetic fields, which allows to simultaneously obtain PET and MR images [6, 34].

### 2.1.3 Performance Parameters

There are different parameters to evaluate the performance in PET. Nevertheless, they are limited by physical effects or by the intrinsic properties of the system. Moreover, each kind of PET system, e.g., experimental, pre-clinical or clinical, consists of different detectors and geometrical configurations. Therefore, the evaluated parameters shall be reported including the type of PET system, as the results and conclusions may differ considerably.

This section describes the most important parameters: energy resolution, coincidence resolution time (CRT), image spatial resolution, count rate performance and sensitivity. In this thesis, the energy resolution and the CRT of "experimental" setups are studied. Therefore, the rest of parameters are briefly introduced only for completeness.

#### 2.1.3.1 Energy Resolution

To evaluate the energy of the incoming  $\gamma$ -photon through the scintillation event thanks to the data provided by the SiPM, a calibration between the data and the respective energy is needed. The available data is the number of optical photons detected in the corresponding active area of the SiPM.

The ability of the detector to determine the energy value of the expected  $\gamma$ -photons is of paramount importance in PET [3]. Not only for most of its uses on different performance parameters, but also for its role in understanding which physical effects occur. This accuracy is referred to as the energy resolution of the detector and is characterized by the FWHM of the photopeak in the energy spectrum, which is the histogram filled with the calibrated energy values of the incoming  $\gamma$ -photons.

If several of the incoming  $\gamma$ -photons are attenuated before being detected, the width of the photopeak may vary [52].

In addition, small fluctuations in the energy spectrum can arise due to several processes. Therefore, it is required to state if a background modelling or a specific function is fitted to the spectrum in order to obtain the FWHM [52].

#### 2.1.3.2 Coincidence Resolution Time

The ability of the PET detector to accurately account for time difference between coincident  $\gamma$ -photons is very important in PET. A spectrum of the measured time difference is generated and thus this accuracy can be characterized if the expected time difference is known [52]. The FWHM of the peak in the time difference spectrum is typically reported and referred to as the coincidence resolution time (CRT) of the detector. The time difference spectrum may contain a background and non-Gaussian tails caused by the random and scattered events, and the different CRT resolutions of the detector's components.

## 2.1. PET

Therefore, a background removal model is normally applied. The report of results shall mention whether the background model or a fit to the time skew spectrum are computed [52].

As an important note, when the CRT of the scanner is lower than the actual time the  $\gamma$ -photons need to hit the detectors, the spatial resolution along the LOR is improved by the time of flight (TOF) method which reduces noise in the final image [75]. The TOF method characterizes the position offset  $\Delta d$  along the LOR using the time difference  $\Delta t$  and the fact that the  $\gamma$ -photons travel at the speed of light  $c_0$ . The relation is shown in Equation 2.1.8.

$$\Delta d = \frac{\Delta t \cdot c_0}{2} \quad (2.1.8)$$

### 2.1.3.3 Image Spatial Resolution

For PET images to be used for diagnostics, their spatial resolution is vital. The overall PET spatial resolution  $R_{sys}$ , i.e., the spatial resolution of the final image, can be approximated as shown in Equation 2.1.9 [52].

$$R_{sys} = \sqrt{R_{det}^2 + R_{range}^2 + R_{acol}^2} \quad (2.1.9)$$

In Equation 2.1.9,  $R_{det}$  is the detector resolution,  $R_{range}$  is the positron range effect and  $R_{acol}$  is the acollinearity effect. As discussed in Section 2.1.1.2, the two latter ones set fundamental limits to the spatial resolution in PET.

In addition, there are extra terms that may degrade the spatial resolution, such as the employed reconstruction algorithm [52], the Compton scattering, or the own system limitations. A detailed explanation of the limits of this performance parameter can be found in [39].

### 2.1.3.4 Count Rate Performance

The noise equivalent count rate (NECR) is proportional to the SNR in the final reconstructed images [10]. To report its value, a model to distinguish the true, scattered and random events of detected coincidence events is necessary [52], see Figure 2.6 for illustration. The NECR is defined in Equation 2.1.10[10].

$$NECR = \frac{T^2}{T + S + kR} \quad (2.1.10)$$

In Equation 2.1.10, T, S and R denote the rates of true, scattered and random coincidence events respectively, and k is a factor describing different methods of correcting random coincidences.

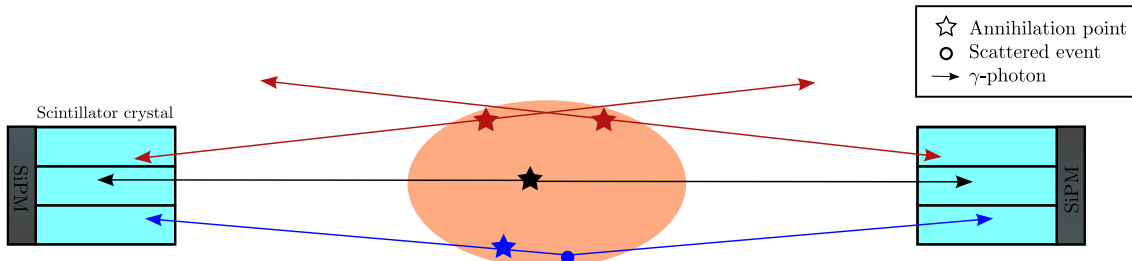


**Figure 2.6:** Accounted coincidence events provoked by different LORs: **real/true coincidence**, **random events** and **scattered events**. Sketch follows discussions and illustrations in [3].

## 2.2. MRI

### 2.1.3.5 Sensitivity

The sensitivity of a PET scanner can be defined as the ratio of the number of detected coincident  $\gamma$ -photons per unit of activity concentration in a source [cps/MBq] [49]. Sensitivity depends mainly on the geometric efficiency and the detection efficiency of the system. The detection efficiency of a detector depends on the scintillation decay time, density, atomic number, and thickness of the detector material.

Based on the named factors, the sensitivity  $S$  of a single ring PET scanner can be expressed as shown in Equation 2.1.11 [49].

$$S = \frac{A\varepsilon^2 e^{-\mu t} 3.7 \times 10^4}{4\pi r^2} \quad (2.1.11)$$

In Equation 2.1.11,  $A$  corresponds to the detector area seen by a point source to be imaged,  $\varepsilon$  to detector's efficiency,  $\mu$  is the linear attenuation coefficient of 511 keV  $\gamma$ -photons in the detector material,  $t$  is the thickness of the detector, and  $r$  is the radius of the detector ring.

## 2.2 MRI

Although this thesis focuses on PET detectors, in order to complete the background for the next chapter, MRI is briefly introduced. For a more detailed introduction to MRI, see [42, 82], which were used as reference for this section.

MRI is a non-invasive imaging technology that produces detailed three dimensional anatomical images. To achieve that, the spins of atomic nuclei, such as Hydrogen, are polarized by using a homogeneous static magnetic field  $B_0$  that ranges from 1.0 T to 14.1 T [82].

After the thermal equilibrium state for the spins is reached, the atoms are perturbed by radiofrequency (RF) pulses. The Larmor frequency of the spins ( $\omega_0$ ) is used for image acquisition. Its value mainly depends on the properties of the atom (included in its gyromagnetic ratio  $\gamma$ ) and the strength of the  $B_0$  field, as shown in Equation 2.2.1 [79].

$$\omega_0 = \gamma B_0 \quad (2.2.1)$$

After the RF pulse is applied, the system tends to return to the initial state inducing a magnetic flux. By placing receiver coils, the magnetic flux yields a change in the voltage of the coils, in accordance with Faraday's law of induction. This signal is used to reconstruct the spatial distribution of the atoms.

Finally, for the spatial encoding of MRI signal, gradient coils which produce timely variant magnetic fields in three spatial dimensions are used. Nonetheless, the details of this technique are out of the scope of this thesis.

## 2.3 PET/MRI

The combination of PET with MRI has several benefits. The main reason is that PET provides functional information about the metabolism of the living body, but to provide morphological information, another imaging technique is required. MRI not only provides that information, but also additional functional information with functional MRI [24]. Moreover, it provides a high soft-tissue contrast and no additional radiation dose is needed. Both benefits are important reasons to rather use MRI than computed tomography (CT), where the living body is exposed to a higher radiation dose, more acquisition time is needed and the soft-tissue contrast is worse [81].

### 2.3. PET/MRI

There are several ways to combine PET and MRI imaging of the living body [81]. The simplest one is a tandem design for sequential examinations. Another possibility is to have a simultaneous acquisition with a small axial size PET insert fitted inside a standard MRI scanner. Additionally, both techniques could be fully integrated in a system. The latter ones are the most interesting configurations, because they reduce the measurement time and facilitate image reconstruction [81].

The limited space inside the magnet of a MRI scanner and the interference in the magnetic field by elements of a PET system are the main drawbacks of a fully integrated PET/MR system [81]. Therefore, the use of an insert can be preferable. Furthermore, the interference can be avoided by designing shielding techniques and new detectors in PET. The most promising design is a SiPM, which was described in Section 2.1.2.2, because studies have reported its low sensitivity to magnetic fields in comparison with other PET detectors [17, 52].

# Chapter 3

## Hypmed

This chapter gives an overview of the HYPMED project and the explanation for two of its challenges, namely the depth of interaction and the parallax error. Subsequently, this chapter includes the description of two DOI-capable detectors as solution to face these challenges, whereas one of them is the proposed candidate for the HYPMED project. In addition, the importance of crystal identification is described as a key factor in the use of this particular detector.

### 3.1 Basic Idea

Breast cancer is one of the most common diseases among women [28]. It provokes a tortuous path with not only several physical consequences due to therapies and surgeries, but also a psychological counterpart [66]. Nevertheless, if the cancer is detected in an early stage and the therapy is convenient, its lethality is significantly reduced [28]. Therefore, together with an early detection, a non-invasive characterisation of cancer is desired.

In 2016, the European Project HYPMED took shape when several entities across Europe, including our working group, decided to assess this challenge [16, 56]. HYPMED seeks to develop a radio-frequency field-penetrable PET insert for simultaneous PET/MRI and thus improve breast cancer diagnosis [25, 57].

As introduced in Section 2.3, PET and MRI together can provide molecular and functional information that may be vital in therapy [47]. Both techniques side by side allow precision imaging of breast cancer by combining the high sensitivity, high resolution and low dose of PET inserts with the advantages of MRI.

Current detection of breast cancer with whole-body PET (WBPET) is generally successful, but not when detecting the disease in early stages. The main obstacle to this is the sensitivity of the system for subcentimeter breast tumors (lower than 60 %) [28].

To be able to diagnose cancer foci in the millimeter range, a scanner with good spatial resolution is not sufficient [69]. High sensitivity to enhance the final image quality and a good energy resolution to reject scattered or background events are also required. In addition, a good CRT resolution is needed to use the TOF method to improve the spatial resolution along the LOR. By doing so, the possible interference of organ motion, especially from the heart, in terms of provoking random coincidence events can be reduced.

In Section 2.1.3.5, the geometrical efficiency was introduced as a key factor for the sensitivity of a PET scanner. The distance between the detector and the source, the total number of detectors in the ring and the radius of the ring are some of the important parameters that affect the geometrical efficiency. One possibility to enhance the sensitivity of the system is to decrease the radius of the ring. With that, the solid angle of the source over the detector increases and the geometrical efficiency improves [49].

### 3.1. BASIC IDEA

Therefore, in the light of the above, HYPMED aims to integrate an innovative fully-digital MRI-transparent PET-detector into a novel multi-channel PET-transparent MRI surface coil for a breast-specific insert. To adapt to different anatomies and keep the breast tight, two PET rings are designed (see Figure 3.1 and 3.2 for illustration). Each ring is divided into two halves. One half is fixed and the other half is movable.

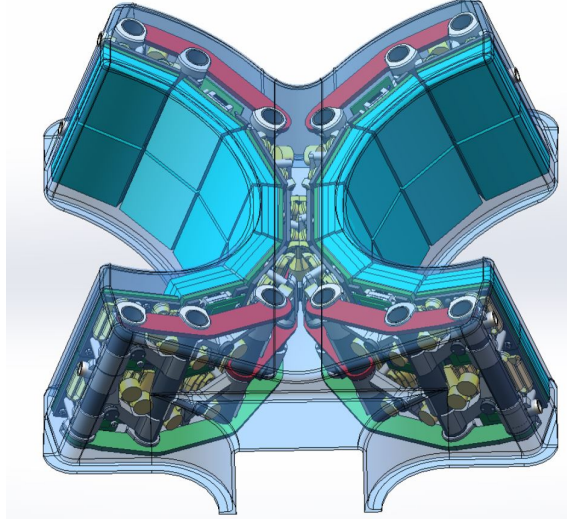


**Figure 3.1:** 3D representation for two halves of PET rings which belong to the PET/MRI insert. The two rows of detectors as well as the holding mechanism are visible. Courtesy of *TU Delft*.

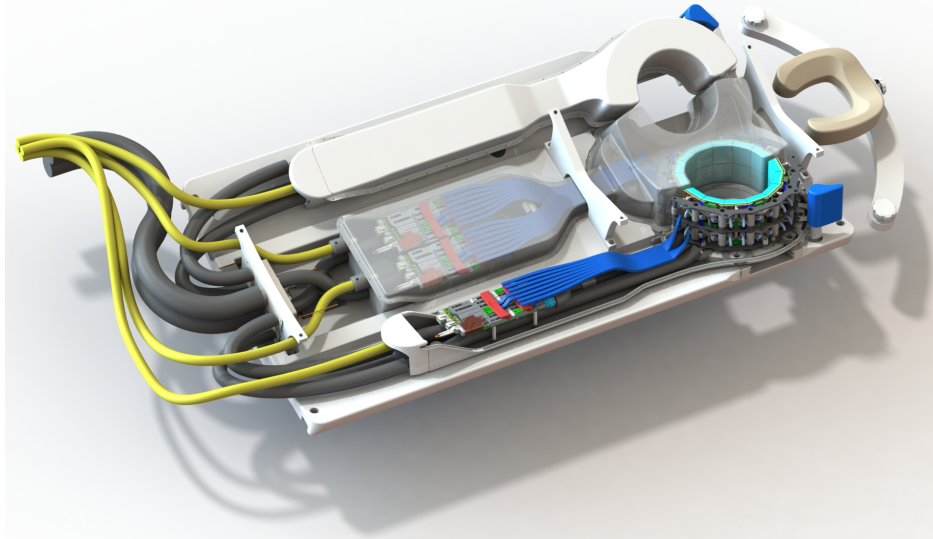


**Figure 3.2:** 3D representation of the complete HYPMED PET/MRI insert. The two PET rings as well as the electronics (motherboard in green and cables in blue) and cooling tubes (grey) are visible. Courtesy of *TU Delft*.

One of the drawbacks when reducing the radius of the PET scanner is the increase of the parallax error [61]. The parallax error leads to a worsening of spatial resolution. In this case, the spatial resolution can be improved if the depth of interaction (DOI) of the  $\gamma$ -photons is provided. Furthermore, to obtain a good enough energy and CRT resolutions in the system, the detector candidates shall aim to equal or enhance the results from similar systems. Some reported results are shown in Table 3.1.

In Section 3.2, parallax error and DOI are described. A more detailed explanation of both concepts can be found in [38].

### 3.2. DOI AND PARALLAX ERROR

PET system	Crystal material	Photo sensor	DOI-method	$E_r$	$CRT_r$
Small animal [23]	LYSO	PSPMT	Phoswich	13.4%	-
Brain insert [62]	LYSO	aSiPM	Two-layered scintillator	FL: 18%, SL: 16%	420 ps
Dedicated organ [33]	LYSO	SiPM	Dual-ended readout	15.7%	603 ps
Small animal [30]	LYSO	SiPM	Dual-ended readout	12.9%	680 ps
Breast/Brain insert [37]	LYSO	SiPM	Dual-ended readout	16%	-
Small animal [29]	LYSO	aSiPM	Three-layered scintillator	19.7%	591 ps
Small animal [5]	LYSO	aSiPM	Three-layered scintillator	FL: 32.7%, SL: 20.9%, TL: 16.5%, M: 19.1%	613 ps

**Table 3.1:** Characteristic and best results of energy and CRT resolutions for systems similar to the one sought in HYPMED. All PET systems are reported as experimental, see Section 2.1.3. FL, SL and TL are first, second and third layer, respectively. M is reported mean value and PSPMT corresponds to position sensitive PMT. Values taken from named references in first column.

In Section 3.3, two DOI encoding detectors and methods to deal with these challenges are given. Moreover, the selected solution is presented and the importance of crystal identification is introduced. In Section 3.3.1, different approaches to crystal identification problems are mentioned. Lastly, in Section 3.3.2, one further challenge on our solution, the inter-crystal scattering (ICS), is described.

## 3.2 DOI and Parallax Error

When an incoming  $\gamma$ -photon enters a scintillator crystal, it may transfer its energy to an electron of the scintillator material at a specific location along the crystal. This location is known as depth of interaction (DOI) information

To position the scintillation events generated by the incoming  $\gamma$ -photon, PET scanner normally employ the so-called Anger logic. In this method, each of the events is assigned a coordinate ( $x, y$ ) which is a pseudo-position of the gamma interaction [2, 73]. These 2D positions depend on the distribution of detected optical photon counts in the detector, see Section 4.5.3. Therefore, the DOI information is simply assigned a constant value for all events based on the attenuation coefficient of the scintillator material [38]. The main issue of assuming the DOI to be constant is the uncertainty in the LOR, see Figure 3.3 for illustration. This uncertainty is commonly known as parallax error (also known as radial astigmatism or radial elongation).

### 3.2. DOI AND PARALLAX ERROR

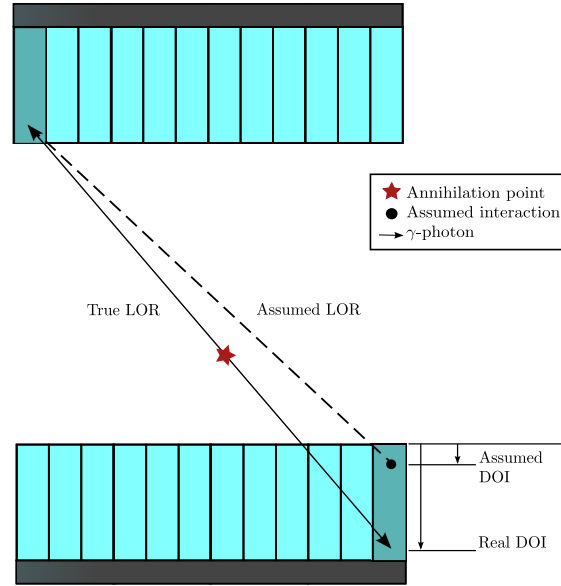


**Figure 3.3:** Schematic drawing of the parallax error resulting from an oblique LOR without DOI information. The dashed line represents the assumed LOR (which is the same for all coincidence events between those two crystals) while the solid line represents the true LOR (which can be drawn with DOI information from that specific event). Figure follows discussions and illustration in [38].

The parallax error is increased if the incoming  $\gamma$ -photons do not enter perpendicularly the detector, or specifically the crystal (see Figure 3.4a for illustration). In ring geometry PET scanners, for a source at the center of the field of view (FOV), most of the emitted  $\gamma$ -photons enter the detectors perpendicularly to the detector face. However, when the source location has a radial offset from the centre, most of the detectors become angled with respect to the LOR. The annihilation  $\gamma$ -photons have more possibilities to penetrate through the first detector they encounter and be detected in an adjacent detector. As a consequence, the spatial resolution in the radial direction degrades towards the peripheral FOV.

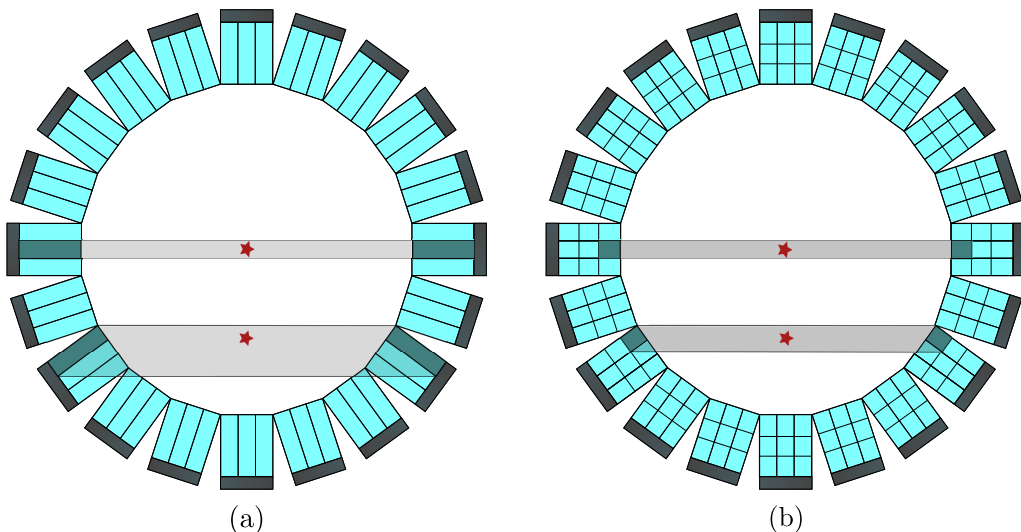


**Figure 3.4:** Shadowed area represent all accessible LORs for the marked annihilation event (red star), that means, the parallax error in two PET ring detectors: **(a)** Sketch showing the increase of parallax error for events in which the incoming  $\gamma$ -photons do not enter perpendicularly the detector without DOI information. **(b)** Sketch showing how DOI-capable detectors reduce parallax error. Figure follows discussions and illustration in [38].

### 3.3. DOI-CAPABLE DETECTORS

Moreover, parallax error causes a radial elongation artefact that is as a challenge to high resolution PET [38]. In addition, this uncertainty becomes increasingly problematic as the ring diameter is decreased [61], due to the increase of events occurring in the peripheral FOV.

As expected, this effect is reduced even if partial DOI information in the detector is available, see Figure 3.4b. Consequently, a uniform high spatial resolution can be achieved [38].

One solution to obtain DOI information is to use depth-encoding detectors. With them, PET scanner with smaller ring diameters and good spatial resolution are possible [38]. A smaller ring diameter implies a smaller  $\gamma$ -photon acollinearity effect, higher sensitivity and lower cost [38].

Furthermore, with the help of DOI, the CRT resolution may be improved [38]. In small ring PET detectors or in long narrow scintillator crystals, the time between the interaction of the  $\gamma$ -photon within the scintillator and the detection of the optical photons may be important. If the DOI information is available, a time skew correction for the location of the interaction is possible and thus the CRT is enhanced. This is especially significant in TOF PET systems [38].

With the help of DOI information, the energy resolution can be improved as well. The number of interactions of the  $\gamma$ -photons depends on the distance they travel before depositing their whole energy. That is why the number of optical photons (proportional to the energy of the incoming  $\gamma$ -photon) varies depending on the DOI. Therefore, the number of optical photons corresponding to the 511-keV  $\gamma$ -photons can be corrected depending on the point of interaction in the scintillator, which results in an improved energy resolution.

## 3.3 DOI-Capable Detectors

Various DOI encoding apparatus and methods have been studied among researchers including multi-layered scintillators (phoswich, offset structure, mixed shapes), multiple crystal-photodetector layers, monolithic scintillators blocks, laser engraving, dual ended readout and AX-PET [26, 38].

Our working group has focused its research on two of these: monolithic scintillator blocks and multi-layered scintillators with offset structure (see Figure 3.5). Therefore, both approaches are introduced in the following paragraphs. Moreover, the second type is used in the HYPMED project and the chosen characteristics are described in Section 4.1.

Monolithic scintillator blocks consist of one crystal coupled to all readout channels (sensitive areas where the SPADs are) of the detector, see Figure 3.5a. The  $\gamma$ -photons in this geometry create optical photons isotropically. For that reason, the light distribution of the events is spread over all readout channels and presents a different pattern depending on the point of interaction [40]. Besides of the x- and y-coordinates, the DOI is also available. To determine the light distribution pattern a priori is not possible. Therefore, an external calibration is needed to correlate a pattern with the corresponding point of interaction [40]. Hence, it is complicated to obtain a quick evaluation of the detectors and to possibly recalibrate the systems once the detectors are mounted in the scanner.

The multi-layered scintillator with an offset structure consist of arrays of many small crystal needles arranged in multiple layers, see Figure 3.5b. Each of the crystal needles is surrounded by a reflector, the so-called inter-crystal layer, which helps to avoid cross-talk of optical photons between crystals on the same layer. In this case, the crystal pitch is much smaller than the readout channels. To allow an identification of the scintillating crystal, light sharing is employed, e.g., a light guide (see Figure 3.5b for illustration). This light guide spreads the scintillation light exiting a single crystal over a larger area of a photosensor array, including different readout channels [52].

### 3.3. DOI-CAPABLE DETECTORS

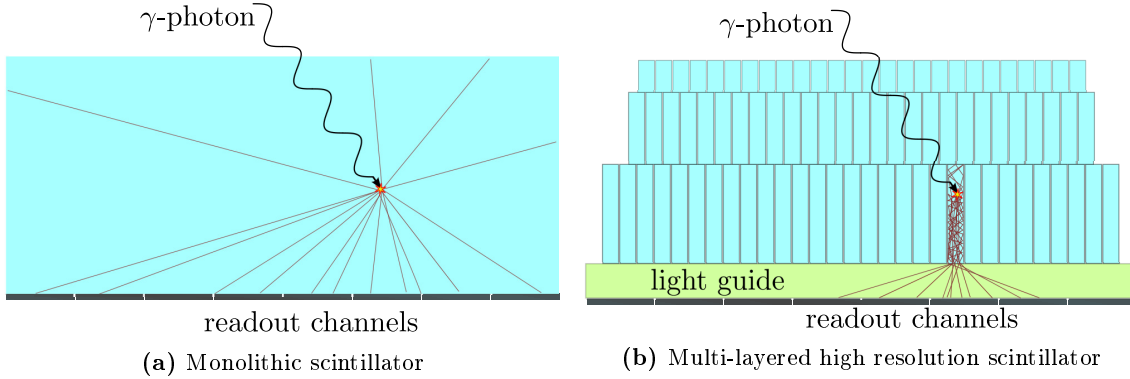


**Figure 3.5:** DOI-capable crystal configurations and readout schemes showing a gamma interaction. (a) **Monolithic scintillator**. A correlation of the scintillation position and the measured signals in the readout channels is required to reconstruct the interaction position. (b) **Multi-layered high resolution scintillator** coupled via a light guide to readout channels. The channel pitch is larger than the crystal pitch. Hence, the optical photons exit the crystal at the bottom and are spread by the light guide over a combination of multiple readout channels. An identification algorithm to reconstruct the interaction position is required. Figure follows illustrations in [52].

The positions of the interaction in the x- and y-coordinates are calculated and binned into a 2D histogram known as a flood histogram or flood map (see Figure 3.6). The scintillating crystal can be identified by studying the light accumulation points in the flood map [54] without requiring a previous external calibration. Hence, a quick evaluation and calibration of the detectors is possible without complicated setups. Furthermore, it allows a possible recalibration of systems once the detectors are mounted in the scanner.

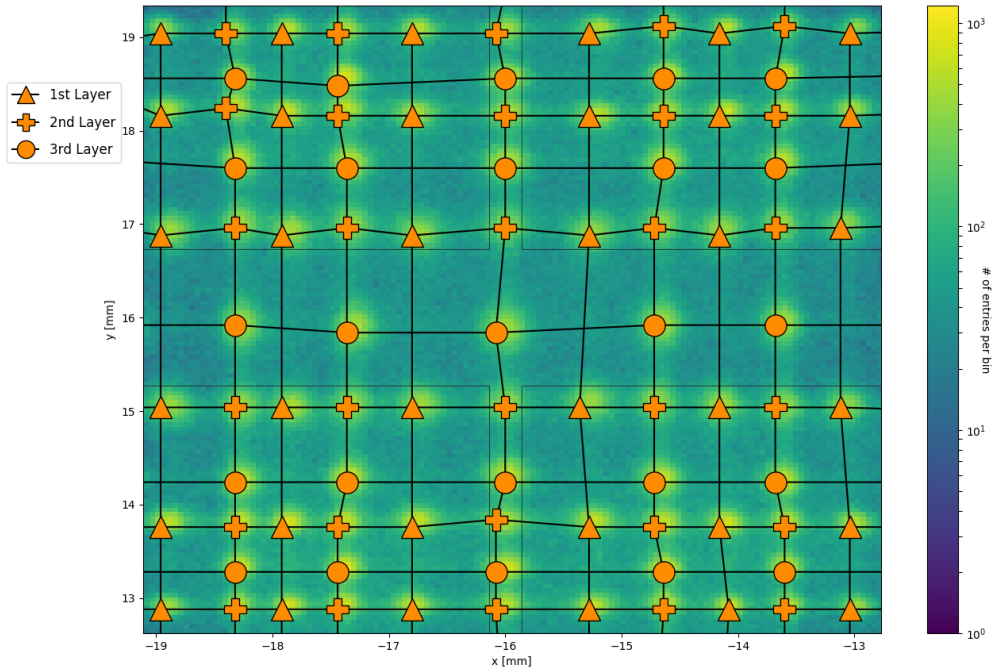


**Figure 3.6:** Example of a flood map for a multi-layered high resolution scintillator. The different light accumulation points are assigned to the corresponding crystal which belongs to a specific layer depending on the offset structure. The CPM is connected with black lines that delimit the rows and columns. The gray lines correspond to the readout channel area.

### 3.3. DOI-CAPABLE DETECTORS

As mentioned before, to identify each scintillation event with its respective crystal, the flood map is analyzed. Since no external calibration is performed, it is necessary to assign the crystals with their corresponding light accumulation point in the flood map. This assignment generates a crystal position map (CPM), see Figure 3.6. The CPM is employed to identify each scintillation event to a specific crystal index. When the 2D-coordinates of an interaction are compared with the CPM, the closest crystal position to the coordinates identifies the most probable scintillating crystal. Thus, the accuracy of the CPM is crucial to the detector's intrinsic spatial resolution [72, 73].

Since each layer presents a different offset in x- or y-direction, the light accumulation points of each layer (corresponding to the respective crystals) can be distinguished, as shown in Figure 3.6. Thereupon, the accuracy of the CPM is also vital to differentiate the crystals from different layers and return the DOI information.

Taking into account the above, an appropriate crystal identification with an accurate CPM is required. In Section 3.3.1, the possible different approaches to generate a CPM are described.

A possible counterpart of the described configuration occurs if the incoming annihilation  $\gamma$ -photons interact with more than one detection element within the same block detector. This effect is called inter-crystal scatter (ICS) (see Section 3.3.2) and can cause an event mispositioning in addition to the parallax error.

#### 3.3.1 Crystal Identification

An optimal crystal identification method is required to spatially identify the most probable scintillating crystal of an interaction event. Firstly, a CPM should be generated from the detector's flood map. Then, considering the CPM, each scintillation event should be identified with a specific crystal index. After that, the scintillation events identified by the same crystals are analyzed. Finally, an evaluation and calibration of the detector can be realized on crystal level.

Hence, it is vital to generate accurate CPMs. The three main kind of methods to achieve this are [72]:

1. *Manual segmentation* of flood maps. It is time consuming, especially for configurations with thousands of crystals.
2. *Semi-automatic segmentation* of flood maps. Traditional image segmentation algorithms with the help of manual corrections.
3. *Prior knowledge based automatic segmentation* of flood maps. The most robust solution based on information from the detector configuration.

Although the reconstruction effort is larger for the third kind, they are commonly utilized due to their good results. Several representative approaches are available in [72, 73]. Unfortunately, most of them are developed to produce CPMs of detectors without DOI information. Therefore, in the case of multi-layered scintillators with an offset structure, the layer distinction and crystal labels generation provoke a problem for these methods [73].

There are other methods, e.g., in [73], where the attenuation effect is exploited to distinguish the different layers. However, in our case, the height for the different layers has been optimized to diminish the attenuation effect in the flood map. Another method based on Gaussian mixture models (GMM) has been implemented [80]. Unfortunately, it is time-consuming and impractical for large dimension position histograms, as ours, because a large number of parameters for the GMMs must be estimated [73].

### 3.3. DOI-CAPABLE DETECTORS

Therefore, in order to have an optimal crystal identification for the HYPMED project, this thesis focuses on a novel method employing distance-based tracking, which is proposed in Section 5.3.

#### 3.3.2 Inter-Crystal Scattering

ICS is the effect in which the incoming  $\gamma$ -photon is scattered and interacts in more than one crystal. The spatial coordinates corresponding to the energy weighted mean (Anger logic) of the multiple interaction locations are different from the location of the first interaction [31]. This inaccuracy could cause a wrong identification of the crystal (see Figure 3.7), which can lead to a worse energy resolution of the detector [5]. Moreover, it reduces imaging contrast and degrades the spatial resolution [23, 31].

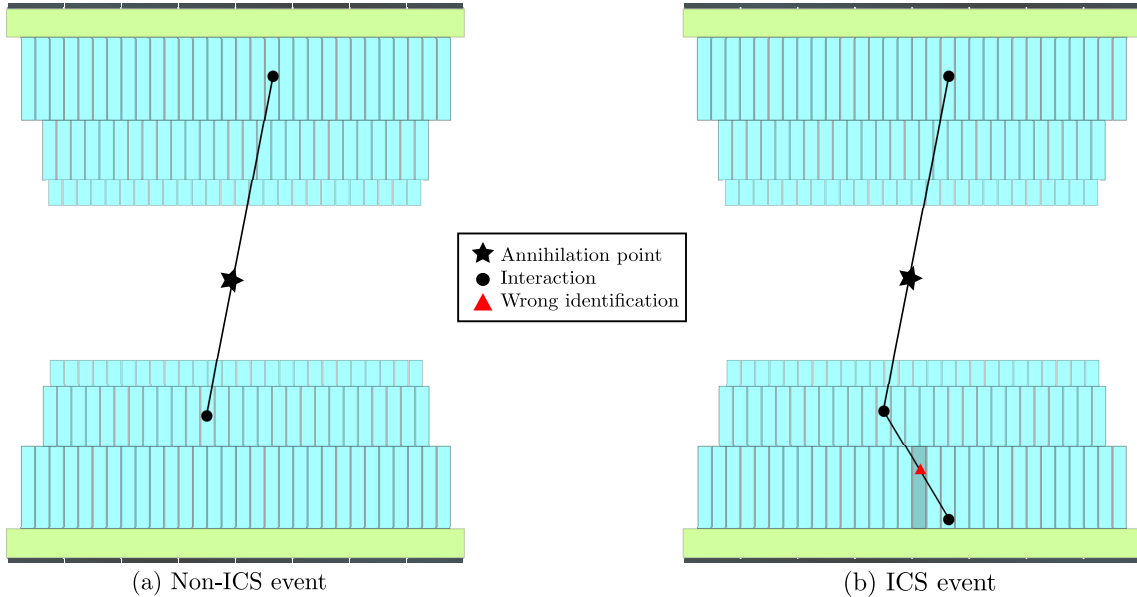


**Figure 3.7:** (a) Sketch representing the identification of an annihilation without ICS. (b) Sketch showing the wrong identification of the same annihilation with ICS. The shadowed crystal is wrongly assigned due to ICS and Anger-type logic calculation. Figure follows discussions and illustrations in [31].

The longer and narrower the crystals are and the more layers the scintillator has, the greater the chance of ICS events. In general, the longer the distance the  $\gamma$ -photon must travel, the more ICS events occur. Therefore, the layer that is close to the photo sensor may have a worse energy resolution due to the longer path of the  $\gamma$ -photon through the scintillator to reach it [5].

As mentioned in [23], several studies show the improvement in image quality if in the analysis of the scintillation events, the ICS events are discarded or their first interaction position is derived. However, complex algorithms are necessary to determine the location of the first interaction of the  $\gamma$ -photon. Therefore, the most feasible option is to reject ICS events. In flood maps, most of the predicted position of ICS events do not clearly belong to one of the light accumulation points [5] and can be rejected without complex analysis. Nevertheless, although rejecting ICS events enhances the energy resolution and increases the image quality, it leads to a significant sensitivity loss.

## Chapter 4

# Materials and Data Compilation

This chapter presents the materials used in all measurement setups. Additionally, the data collection and its compilation for later analysis is described.

Figure 4.1 shows an overview of the materials. The corresponding setup belongs to the side irradiation measurement, which is explained in Section 6. The different setups are described along the analyses in Sections 5 and 6.

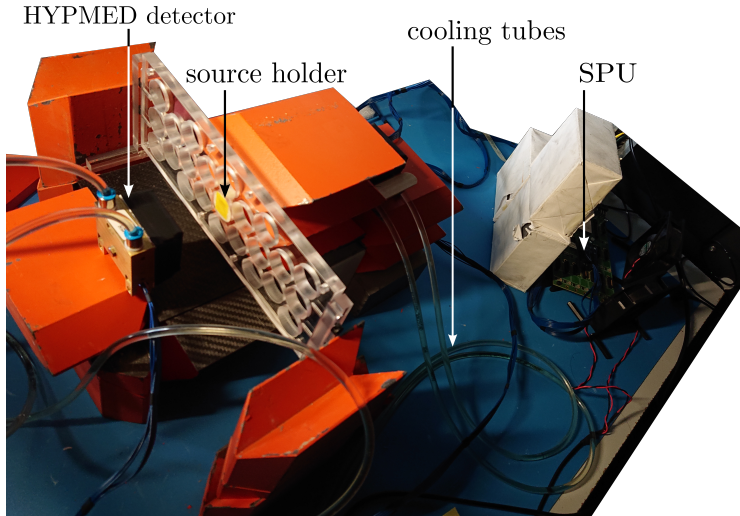


**Figure 4.1:** Overview of setup including the components to be described in this section. Furthermore, on the right, there are fans to cool down the SPU and, on the left, the cooling plate attached to the HYPMED detector is shown. The orange and white blocks are made of lead and are used as shielding elements or as collimators for the irradiation.

### 4.1 HYPMED Detector

The HYPMED detector consists of three main parts: a scintillator, a photosensor and a light guide.

A multi-layered high resolution scintillator with an offset structure is the choice for the HYPMED project. This kind of scintillator was introduced in Section 3. The selected characteristics, such as number of layers, offset or type of inter-crystal layer are defined in Section 4.1.1.

Due to its intercompatibility with PET and MRI, the selected photosensor for the HYPMED project is a dSiPM, which was already introduced in Section 2.1.2.2. The chosen properties, such as channel pitch, number of SPADs, its trigger and validation logic, etc., are specified in Section 4.1.2.

## 4.1. HYPMED DETECTOR

Section 4.1.3 defines the used light guide and which glue couples the different components.

The mounted detector stack is shown in Figure 4.2.

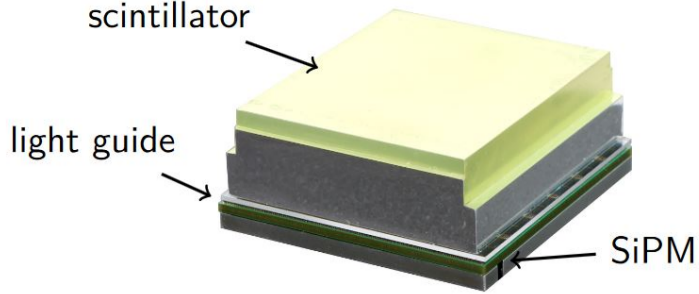
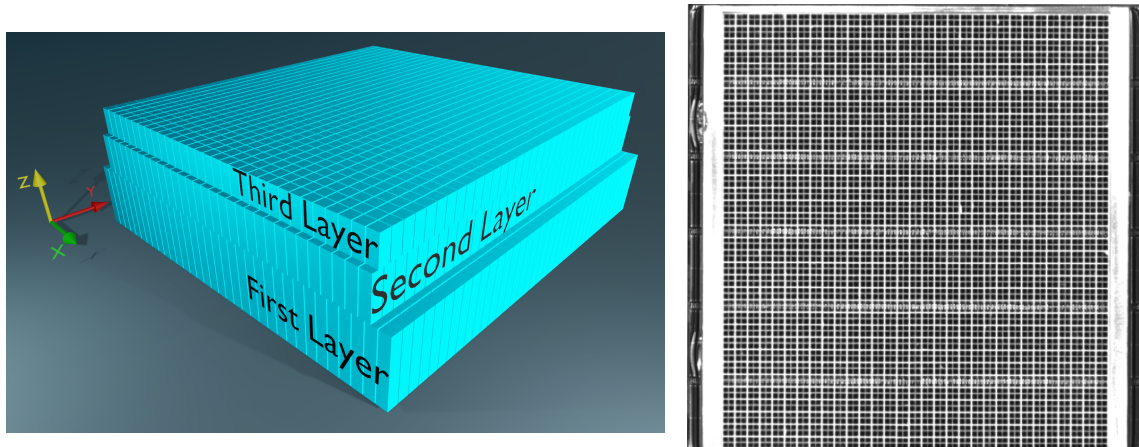


**Figure 4.2:** Manufactured three-layered high resolution scintillator with offset structure coupled with a glass light guide and the corresponding SiPM. Reprinted from our working group.

### 4.1.1 Scintillator

Scintillators are normally mounted in arrays of single crystals. In the HYPMED project, each of the crystals is a cerium-doped lutetium yttrium orthosilicate (LYSO) manufactured by Sichuan Tianle Photonics Co. Ltd. [46]. Between the crystals, an inter-crystal layer contains the optical photons and spatially distributes the events. Several tests carried out by our working group led to the selection of a barium-sulfate ( $\text{BaSO}_4$ ) powder mixed with an epoxy as inter-crystal layer [15]. It ensures a better flood map quality in contrast to other commonly used reflectors, e.g., enhanced specular reflector (ESR). Due to its low optical crosstalk between the LYSO crystals, the  $\text{BaSO}_4$  inter-crystal layer can reduce the number of optical photons that are detected [29].

As shown in Figure 4.3, the HYPMED scintillator consists of three layers of crystal arrays. Every layer is shifted differently. Therefore, the generated flood maps show light accumulation points that can be assigned to each single crystal of the scintillator, as observed in Figure 3.6.



(a) Sketch in 3D of the HYPMED scintillator. The shifts in the x- and y- are visible. The first layer is the closest to the SiPM and largest one. The second layer is in the middle and the third layer is the smallest one on top of the others. Figure adapted from [15].

(b) Plan view of the HYPMED detector stack. Reflector from third layer has been removed. The white lines correspond to the inter-crystal layer. Five rows of bond wires from the sensor tile are visible.

**Figure 4.3:** Sketch and plan view of the three-layered high resolution scintillator with an offset structure.

#### 4.1. HYPMED DETECTOR

The total number of crystals in the scintillator is 3425. The first layer, i.e., the layer which is coupled to the dSiPM, consists of 1224 crystals covering an area of approximately  $45 \times 48 \text{ mm}^2$ . The second layer, i.e., the layer in the middle, is shifted in the defined x-direction with respect to the first layer by half a crystal pitch. However, the actual difference to the first layer is one and a half crystal pitches from both edges in x-direction. This is due to its centered position and size. 1116 crystals belong to the second layer covering an area of approximately  $41 \times 48 \text{ mm}^2$ . The third layer presents the same shift in the x-direction, but also a shift in the y-direction by half a crystal pitch. It is also centered and its number of crystals is 1085 covering an area of approximately  $41 \times 46.7 \text{ mm}^2$ .

The total height of the scintillator is 15 mm and the crystal pitch is 1.33 mm. Moreover, the heights of the first, second and third layers are 7.5 mm, 4.5 mm and 3 mm, respectively. They were chosen such that the probability of interaction between the crystals and the  $\gamma$ -photons is approximately the same in all layers. Hence, in the flood map, the number of entries per bin, which is called intensity, of the light accumulation points is approximately the same, regardless of which layer the assigned crystal belongs to, as observed in Figure 3.6. Moreover, to ensure a better light collection, the scintillator is surrounded by a reflector and wrapped in teflon tape.

In this kind of scintillators, the reconstruction of the scintillation events is a challenge: not only because of the number of crystals to handle, but also because it presents an irregular grid of scintillating crystals. Figure 4.4 shows the expected physical position of the crystal's centers from each layer over the pixels of the expected dSiPM, which is introduced in the next paragraphs.

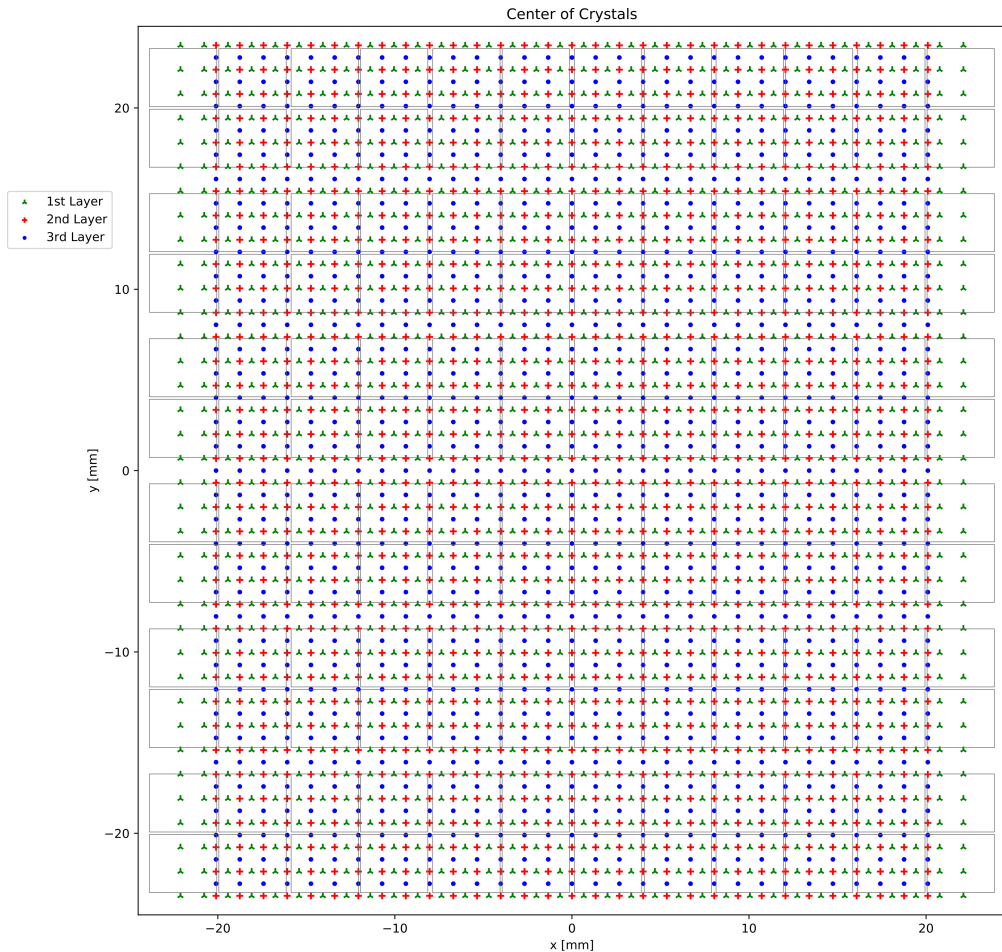


**Figure 4.4:** Geometrical representation of the crystal positions over the SiPM. The gray lines correspond to the actual sensitive area of the SiPM.

## 4.1. HYPMED DETECTOR

### 4.1.2 Photosensor

The description of the photosensor is based on the PDPC Tile-TEK user manual [43] and the paper [54]. The selected photosensor (DPC3200-22) is a sensor tile formed by dSiPMs and manufactured by Philips Digital Photon Counting (PDPC). It covers an area of  $48 \times 48 \text{ mm}^2$  and it is divided into 36 Digital Photon Counters (DPCs), called dies. As shown in Figure 4.5, they are arranged in a  $6 \times 6$  matrix and are connected to a field-programmable gate array (FPGA) via bond wires. Each die comprises  $2 \times 2$  readout channels with a pitch of 4 mm, called pixels. Each pixel consists of 3200 SPADs. When an avalanche is produced in a SPAD, the applied bias voltage drops and this breakdown is stored as binary information. An active quenching circuit stops the avalanche. When a readout is requested, all SPAD breakdowns are counted. Moreover, as explained in Section 2.1.2.2, SPADs can be inhibited individually. This feature is used to deactivate a fraction of SPADs per pixel that show a significantly high dark count rate (DCR) [54]. This last step is explained in Section 4.5.2.

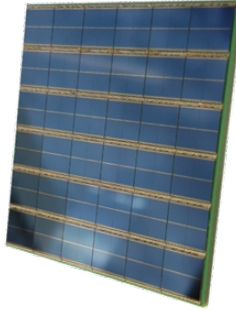


**Figure 4.5:** Array of the dSiPM. The  $6 \times 6$  dies array is visible with 4 pixels per die. The bond wires between the dies are also observed. Reprinted from our working group.

The bias voltage  $V_{bias}$  sets the operating voltage of the SPADs. As shown in Equation 4.1.1 and defined in [43], it is determined as the breakdown voltage  $V_{break}$ , which is calibrated, and the excess voltage  $V_{ov}$  (overvoltage), which is set in every measurement. If the overvoltage is set too low (less than 1.0 V), less optical photons are detected [43]. On the other hand, a too high overvoltage (more than 3.3 V) can cause a saturation on the detector due to higher dark count rates. Therefore, a range of about 2 V to 3.3 V should be selected to operate the SPADs [52].

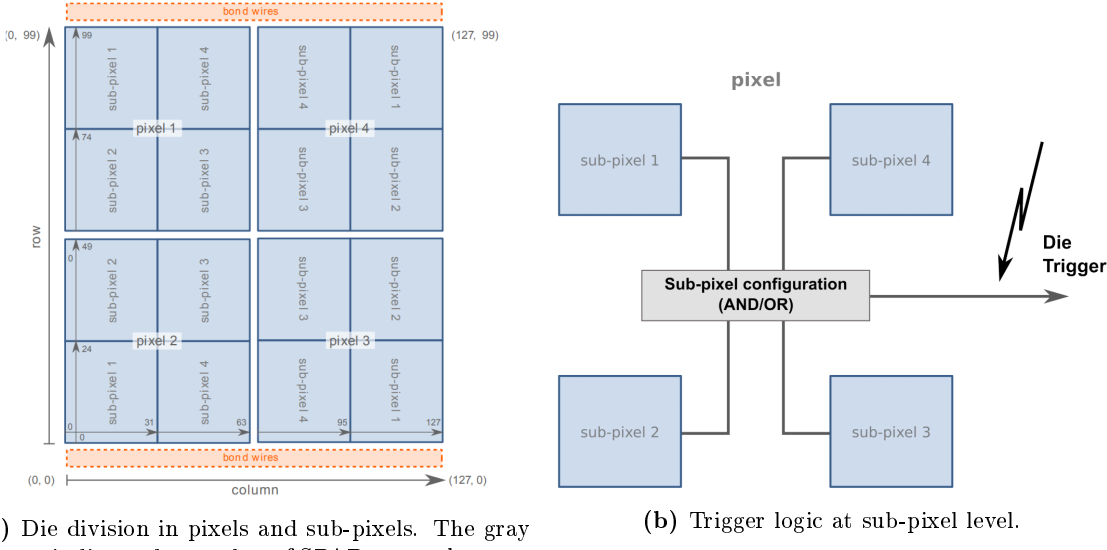
$$V_{bias} = V_{break} + V_{ov} \quad (4.1.1)$$

One of the most important features of the dies is their configurable trigger and validation logic before reading out data, which is explained in the following.

## 4.1. HYPMED DETECTOR

### Trigger and Validation

A pixel is further divided into four sub-pixels (see Figure 4.6a). The 800 SPADs per sub-pixel are grouped together to generate a trigger signal. When a SPAD breaks down, the corresponding sub-pixel releases a logical TRUE. Depending on the trigger scheme, an acquisition cycle is initiated or not. The selected trigger scheme connects the four sub-pixels with an AND/OR-logic, as shown in Figure 4.6b.



(a) Die division in pixels and sub-pixels. The gray arrows indicate the number of SPADs per column or row.

(b) Trigger logic at sub-pixel level.

**Figure 4.6:** Reprinted from [43].

The trigger scheme defines the necessary number of logical TRUE signals to begin the acquisition cycle [43]. In the presented case, it ranges from trigger scheme 1 where only one logical TRUE signal is required until trigger scheme 4 where four logical TRUE signals are required. Table 4.1 resumes the different possible trigger schemes with the respective threshold of the mean number of SPAD breakdowns required to reach the trigger condition.

Trigger scheme	Sub-pixel configuration	Average threshold
1	$sp1 \vee sp2 \vee sp3 \vee sp4$	1.0
2	$[(sp1 \vee sp2) \wedge (sp3 \vee sp4)] \vee [(sp1 \vee sp4) \wedge (sp2 \vee sp3)]$	$2.33(\pm 0.67)$
3	$(sp1 \vee sp2) \wedge (sp3 \vee sp4)$	$3.0(\pm 1.4)$
4	$sp1 \wedge sp2 \wedge sp3 \wedge sp4$	$8.3 (\pm 3.8)$

**Table 4.1:** DPC3200 trigger schemes with expected average thresholds of number of breakdowns ( $spX$ : sub-pixel X,  $\vee$ :OR,  $\wedge$ :AND). Table follows table in [43].

As explained in [43], when a trigger is released, a timestamp is designated and the respective die enters a validation phase during a pre-defined time. The validation scheme follows the same idea as the trigger scheme, but it acts in each sub-pixel separately. The sub-pixel is divided into groups of 32 SPADs to form a row trigger line (RTL) which leads

#### 4.1. HYPMED DETECTOR

to 25 RTLS per sub-pixel. When further SPADs break down during the validation phase, the corresponding RTLS release a logical TRUE. The logical gates between the RTLS follow an AND/OR-logic and are defined by the validation scheme. In Figure 4.7, a schematic representation of the described architecture is shown.

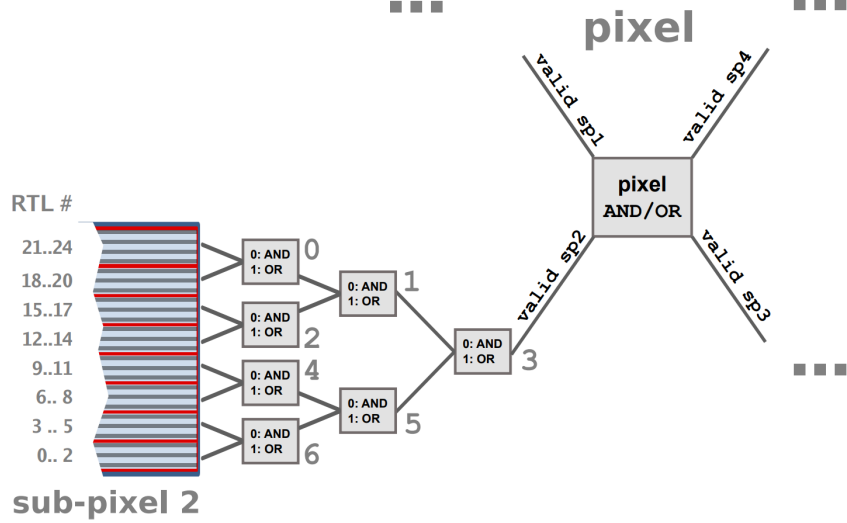


**Figure 4.7:** Validation logic at pixel and sub-pixel level. Reprinted from [43].

Table 4.2 summarises the different possible validation schemes with the respective threshold of the mean number of SPAD breakdowns required to reach the validation condition.

Validation scheme	Average threshold
1	1.0
2	4.7( $\pm 2.1$ )
4	17.0( $\pm 6.2$ )
8	53 ( $\pm 15.0$ )
16	54 ( $\pm 19.0$ )
32	132 ( $\pm 40.0$ )

**Table 4.2:** DPC3200 pre-defined validation schemes with expected average threshold of number of breakdowns. Table adapted from [43].

#### Integration and Readout

When the validation condition is fulfilled, an integration phase in the die is started. This phase is used to accumulate SPAD breakdowns caused by the incoming optical photon pulse during a pre-defined time [43].

As described in [43], after the integration phase, the readout is initiated line by line of SPADs and the binary information of each SPAD is collected. In each pixel, the number of optical photons is summed up. The final output data from each die contains the four optical photon count values and the trigger timestamp.

Subsequently, [43] indicates that a recharge of the active dies is produced and thus their SPADs are sensitive again to wait for the next trigger. The recharge phase is also

## 4.2. TEMPERATURE CONTROL

activated if the validation condition is not fulfilled. Figure 4.8 presents a general flow chart of the event acquisition sequence for one event.

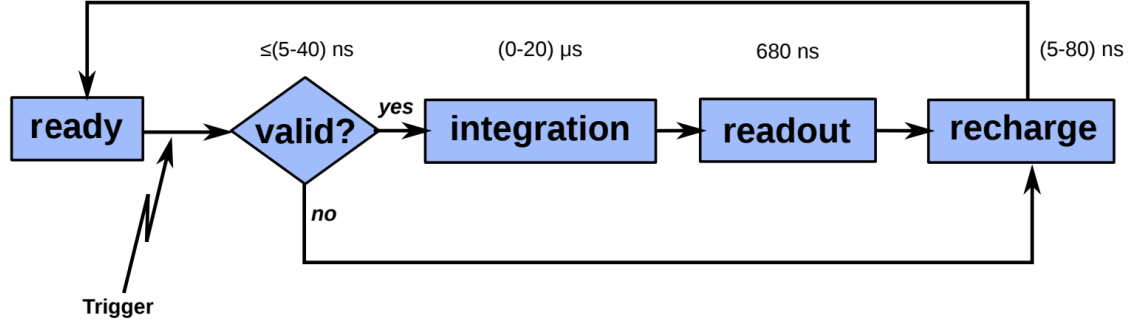


**Figure 4.8:** Flow chart of event acquisition sequence of one event in the dSiPM. Reprinted from [43].

In addition, when a die meets the validation condition, the sensor tile is capable of forcing the neighbouring dies to start an integration phase, even if they do not fulfil the trigger and validation conditions [53]. This feature, called neighbor logic, is fundamental for the work of this thesis and [53] provides a detailed explanation.

### 4.1.3 Light Guide and Glue

The pitch of the pixel (readout channel) from the described sensor tile is 4 mm. As the crystal pitch is 1.33 mm, coupling one pixel to every crystal is not possible. Hence, an additional light guide is needed to spread the scintillation light from a single scintillator element over a multitude of readout channels.

Proportionally to the thickness of the light guide, the scintillation light is spread more or less. To reach more readout channels, a broader spread is required. With information about the optical photons from different channels and using the Anger logic, the reconstruction of the scintillating event is more stable. Nevertheless, each channel receives less optical photons per event and thus increases the relative background contribution.

An optimal light guide thickness was decided according to the study conducted in [15]. In this study, the best generated flood maps were from the 1.1 mm light guide. The tests were carried out with different light guides made of transparent borosilicate glass.

The light guide is coupled to the scintillator and the sensor tile with glue. The properties of this glue, e.g., its refractive index, may alter the number of optical photons that reach the sensor tile [21]. Thus, the glue was selected according to recent experiments carried out in our working group and its name is SCIONIX RTV 481. It is a RTV based ultraclean silicon two component glue designed for scintillators, PMTs and light guides by SCIONIX Holland BV. Its curing time is 48 hours (at room temperature) and its refractive index  $n$  is 1.4 [58].

## 4.2 Temperature Control

The acquisition of data by the dSiPMs through FPGAs produces lots of heat. To dissipate this heat, a liquid cooling system was designed in our group. As shown in Figure 4.1, the cooling plate is coupled to a detector to transfer the heat. Flexible tubes are used to connect the cooling plate individually to a LAUDA RE 307 cooling system. Thanks to the cooling system, the liquid remains constant at the desired temperature and the temperatures of the dSiPMs and the FPGAs are maintained under control.

### 4.3. SOURCES

For all the measurements carried out in this thesis, presented in Sections 5 and 6, the temperature of the cooling system was set to 15 °C.

The SPU also produces heat, but not as much as the dSiPMs. Therefore, a simple dissipation of heat with the use of fans is employed.

### 4.3 Sources

One of the most important radio-tracers that are used today in PET is fluorodeoxyglucose ( $^{18}\text{F}$ -FDG) [10, 19]. However, the relative short half-life of the  $^{18}\text{F}$  (109.8 minutes) limits its use for experiments [14]. Furthermore, due to safety reasons, open radioactive sources cannot be used in the laboratory. Therefore, a similar radioactivity element is desired with a longer lifetime and in the closed form of discs and cubes. One of the most used substitutes is  $^{22}\text{Na}$  in the form of cubes manufactured by the National Electrical Manufacturers Association (NEMA). Its energy spectrum presents characteristic peaks at 511.0 keV and 1274.5 keV [12]. The 511 keV peak due to a  $\beta^+$ -decay in  $^{22}\text{Na}$  represents with fidelity the expected coincidence events in a PET scanner procedure. The used sources in this thesis are listed in Table 4.3 with the corresponding characteristics.

Point-source shape	Element	Characteristic $\gamma$ -photon peaks	Activity (2021-05-17)	Active diameter
NEMA cube	$^{22}\text{Na}$	511.0 keV, 1274.5 keV [12]	1.918 MBq	0.5 mm
NEMA cube	$^{22}\text{Na}$	511.0 keV, 1274.5 keV [12]	0.245 MBq	0.5 mm
NEMA cube	$^{22}\text{Na}$	511.0 keV, 1274.5 keV [12]	0.228 MBq	0.5 mm
NEMA cube	$^{22}\text{Na}$	511.0 keV, 1274.5 keV [12]	0.211 MBq	0.5 mm
NEMA cube	$^{22}\text{Na}$	511.0 keV, 1274.5 keV [12]	0.211 MBq	0.5 mm
disc	$^{22}\text{Na}$	511.0 keV, 1274.5 keV [12]	0.146 MBq	0.5 mm
disc	$^{22}\text{Na}$	511.0 keV, 1274.5 keV [12]	0.146 MBq	0.5 mm

**Table 4.3:** Selected radioactive sources for the different experiments.

### 4.4 Hardware Control: SPU and DAPS

The singles processing unit (SPU) is an electronics board, which was developed by our working group. The SPU is responsible for collecting the data from the sensor tiles via flexible cables, synchronizing it via optical fibers and transmitting it to a data acquisition and processing server (DAPS) via a  $10\text{ Gbits}^{-1}$  optical link [77], see Figure 4.9 for illustration. Moreover, thanks to the SPU, the voltages applied to the sensor tiles can be controlled [20].

The DAPS stores the measured data, the information about the used settings and the message logs transmitted by the SPU. Moreover, the calibration data of the sensor tiles, which is described in Section 4.5.1, is saved in the DAPS and sent to the SPU before each measurement.

## 4.5. PRINCIPLES OF DATA COLLECTION AND PRE-PROCESSING

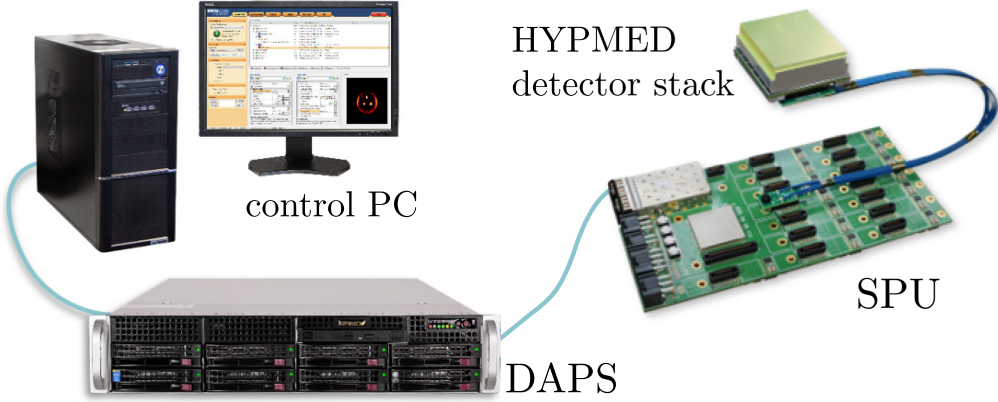


**Figure 4.9:** SPU connected to the HYPMED detector stack via flexible cables and to the DAPS via optical link. The PC runs the control software and is connected to the DAPS. Figure adapted from our working group.

## 4.5 Principles of Data Collection and Pre-Processing

For the data to be collected, a control software is executed. The employed software is the Hyperion Scanner Control Version 6.7, Revision 0, Compilation 21028. It was developed by our working group and it is constantly updated [75, 77].

The software is used to control the parameters of a measurement setup, such as the voltage of the sensor tiles, the saving directory of the data in the DAPS or the duration of the measurement. In addition, the temperature of the different components is monitored.

Before using the software for actual measurements, a calibration of the sensor tile is needed to reduce its intrinsic noise and thus provide more concise data. The calibration of the sensor tile is explained in Section 4.5.1.

Once the calibration is done, the measurements of the experiments can be carried out and the data can be collected. In Section 4.5.2, the most important steps of data collection are described.

After the measurements, the raw data needs to be processed in order to extract meaningful analysis. Section 4.5.3 provides a description of the pre-processing steps applied to the raw data.

### 4.5.1 Sensor Tile Calibration

The calibration of a sensor tile consists of two steps. First, its characteristic breakdown voltage is measured. Afterwards, the dark count map (DCM) of the sensor tile and its "inhibit map" are determined. During the calibration procedure, a constant operating temperature is required to avoid possible unexpected behaviour in the DCM [43]. Furthermore, the sensor tile should be immersed in darkness for the whole procedure.

Once the sensor tile is connected to the SPU and the bias voltage can be changed via the control software, the first step can be carried out. As indicated in [43], the bias voltage is increased until a SPAD breakdown is detected. The corresponding voltage at that moment is defined as the breakdown voltage for the sensor tile.

In the second step, for each SPAD, the number of breakdowns per unit of time is measured, and thus its resulting dark count rate (DCR) is obtained. With the DCRs of all SPADs, the DCM is generated. Figure 4.10 shows that the DCR at the edges of the pixels is lower than in the rest of the sensitive area.

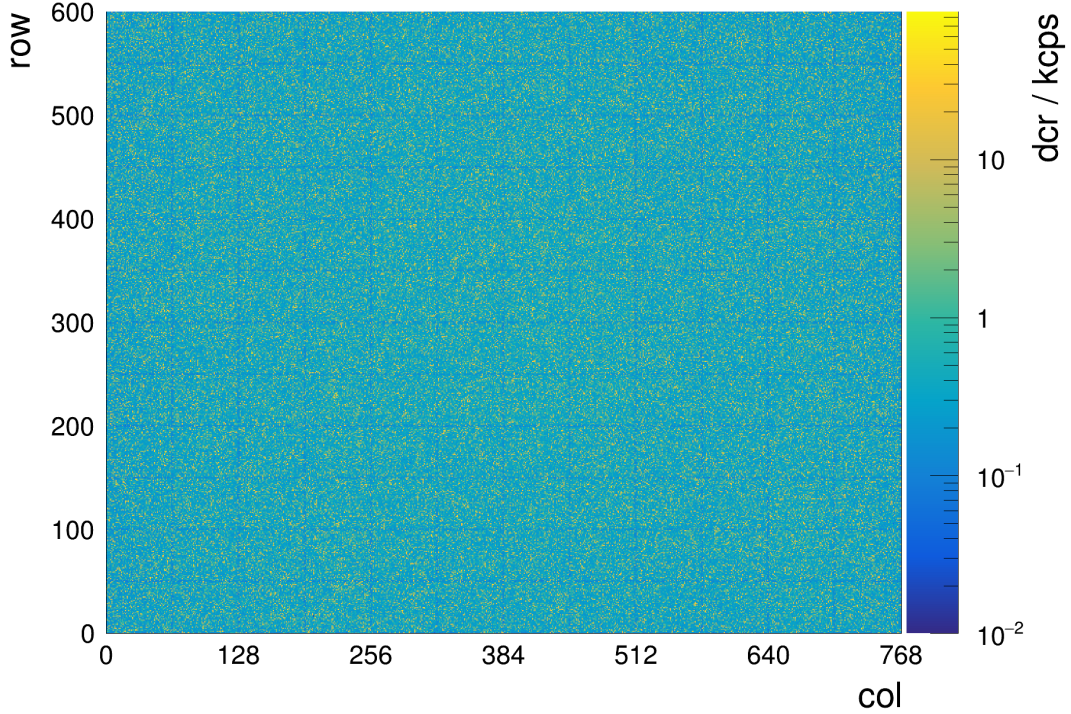


**Figure 4.10:** Dark count map of a sensor tile used in the measurements. The columns (col) and rows correspond to the SPADs of the sensor tile. A logarithmic scale is chosen to observe how the DCR is lower at the edges of the pixels.

The sensor tile can physically disable any SPAD by writing the so-called inhibit memory [43]. With this feature, the SPADs with the highest DCRs can be disabled. In the control software, the percentage of SPADs to be disabled is set. Based on this percentage, an "inhibit map" is generated and, subsequently, stored in the DAPS. Each sensor tile has its own "inhibit map", which shows whether a SPAD must be activated or not.

For all the measurements in this thesis, the percentage of disabled SPADs per die is set to 10%.

#### 4.5.2 Data Collection

After carrying out the calibration of the sensor tiles, the actual measurements can take place. Firstly, the setup is mounted, the sensor tiles are connected to the SPU via flexible cables and, in turn, the SPU with the DAPS via optical link. As mentioned before, the next step is to load the corresponding "inhibit maps" from the DAPS using the control software.

Hyperion Scanner Control provides a user-friendly interface to manage the creation of new directories to store the data. After selecting the directory, the respective settings of the measurements are loaded. This includes the number of sensor tiles, whose firmware the SPU runs, the chosen overvoltage, the trigger and validation schemes, and several further options, which allow a precise control of the measurement. The selected settings are validated by running a test. For example, if the voltage cannot ramp up to the desired one, an error is returned.

Once the control software confirms that the settings are correct, the user can start the pre-measurement mode. In this mode, the sensor tile is transmitting the detected events, but the data is not yet saved in the DAPS. Before storing the data, the user should check that all the significant parameters have reached their expected value. Mainly, the

## 4.5. PRINCIPLES OF DATA COLLECTION AND PRE-PROCESSING

temperature of the detector stack shall achieve a thermal equilibrium.

Finally, if the parameters are within a reasonable range, the measurement starts and the raw data is stored in the DAPS. Thanks to the control software, the measurement time can be defined.

### 4.5.3 Data Pre-Processing: Center of Gravity

Before a scintillation event can be identified with its corresponding crystal index using the flood map, its respective 2D pseudo-position must be calculated out of the measured raw data [2, 73].

Center of gravity (COG) is one of the most used algorithm to decode these 2D positions [52]. To achieve this, COG analyzes the photo counts of the activated or selected pixels and the timestamps of the activated or selected dies [54]. This is possible thanks to the implemented neighbor logic in the analysis of data, which is explained in [53]. If the scintillation is distributed over a large fraction of dies, selecting only the dies close to the main pixel deteriorates the computed COG. Hence, advanced COG algorithms weight the contribution of the pixels to the position depending on the number of optical photons or timestamp that they have. Another possibility is to define one region-of-interest (ROI) around the pixel with the highest number of optical photons or the earliest timestamp, called main pixel. Moreover, two or more ROIs can be accepted to improve the sensitivity of the analysis [54].

*HitAnalysis* is a program to handle the processing of the raw data. It is based on C++ and was developed by our working group. The COG algorithm is implemented in this program and different ROIs can be pre-defined. Depending on the ROI, the algorithm checks if all the required dies for the given ROI have incoming optical photons within a certain time window, called cluster window. However, the scintillating crystals are on different regions, e.g., between the dies, at the edges or within the die. As the ROI is fixed for all the events, there may be regions where the selected ROI does not return a stable COG for some of the scintillating crystals. To have a good resolution on these regions and to improve the sensitivity of this algorithm, a novel strategy to combine the data obtained with four different ROIs is presented in Section 5.2.

In addition, *hitAnalysis* can also apply filters to the raw data. The following three kind of filters are used in this thesis. Firstly, two thresholds for the minimum and maximum number of optical photons of 500 and 5000, respectively. Secondly, a cluster window of 40 ns. Finally, a coincidence window of 20 ns for coincidence measurements.

After running the program, a ".DebugSingles" file is created. In this file, the processed information about every event is shown. The most important information for this thesis are the calculated positions of the selected ROIs, their flag showing whether all the required dies were available or not, the photo sum of the selected dies in the ROIs, the timestamp of the pixels and the optical photon count of the die. In addition, for coincidence measurements, a ".DebugCoincidenceSingles" file is created. This file shows the same information as the first, but in pairs for both sensor tiles.

These files can be quite large (around 100 Gb) depending on the measurement time and number of events. To facilitate data handling, a routine has been developed to extract the mentioned information from these files.

To optimize the consumption of computer resources, each file is chunked and processed in parallel. Subsequently, a high performance data software library named HDF5 is used to manage, process, and store the data [64]. The chunks are then merged into ".hdf5" files and are ready to be analyzed by the proposed algorithm in this thesis (see Section 5).

## Chapter 5

# Optimization of Crystal Identification

As mentioned in previous chapters, the crystal identification algorithm is based on the flood map analysis. Hence, in order to develop and optimize an algorithm for the HYPMED configuration, a first set of measurements is carried out to obtain the necessary flood maps.

This chapter starts by describing the setup used to carry out the first measurements. Thereupon, for a better understanding, the algorithm is explained step by step together with the corresponding results obtained by the first set of measurements. The chapter ends with the results, discussions, and conclusions of the algorithm's performance.

### 5.1 First Measurements: Front Irradiation

The first measurements to obtain the characteristic flood maps of the detector stacks are carried out placing the  $^{22}\text{Na}$  source in front of the detector face. This kind of measurement is called front irradiation, as the source irradiates the detector face frontally.

Once the source is placed, there are two basic arrangements of the detectors to acquire the flood maps:

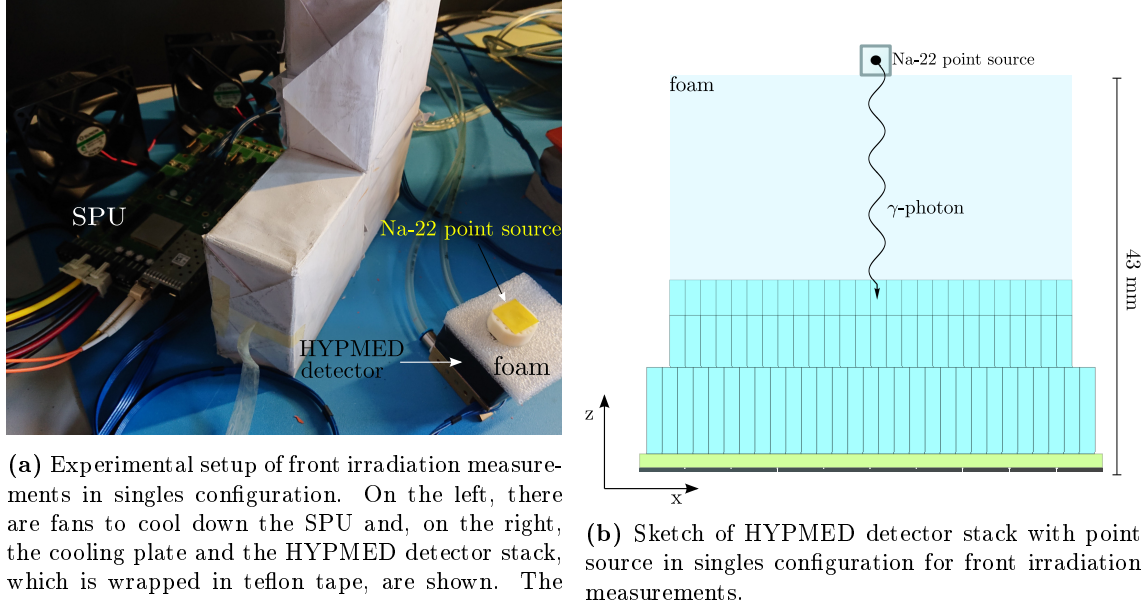
- **Singles configuration.** Only one detector is connected to the setup and measuring. Therefore, only one of the two  $\gamma$ -photons produced by the source is detected per event. The detected individual  $\gamma$ -photons are then called "singles".
- **Coincidences configuration.** Two or more detectors are connected to the setup and measuring. Therefore, the two  $\gamma$ -photons produced by the source can be detected per event, if they arrive within a time window at the two detectors that are placed symmetrically to the source. The detected pairs of  $\gamma$ -photons are then called "coincidences".

The singles configuration is used to acquire the first flood map, due to its simplicity and the availability of only one detector stack at the beginning of the experiments. However, with this configuration only the energy resolution of the detector stack can be determined. In order to obtain the time resolution and thus, a more significant evaluation of the detector stack (see Chapter 6), the coincidences configuration is needed. The measurements with the coincidences configuration are conducted once two detector stacks are mounted and the corresponding setup is built. In both configurations, the measuring time and the distance to the source are kept constant to enable discussions about other factors in the results. In addition, to ensure a better light collection, the scintillators are wrapped in teflon tape.

## 5.1. FIRST MEASUREMENTS: FRONT IRRADIATION

### 5.1.1 Singles Configuration

The singles measurement provides a first quick contact with the detector stack. Figure 5.1 shows the used experimental setup together with a sketch of the detector stack arrangement and the source for a front irradiation measurement. For the sake of simplicity, the source is centered placed over a  $\gamma$ -transparent material, e.g., foam, at a distance of 43 mm to the sensor tile.



(a) Experimental setup of front irradiation measurements in singles configuration. On the left, there are fans to cool down the SPU and, on the right, the cooling plate and the HYPMED detector stack, which is wrapped in teflon tape, are shown. The white blocks are made of lead and are used as shielding elements.

(b) Sketch of HYPMED detector stack with point source in singles configuration for front irradiation measurements.

**Figure 5.1:** Singles configuration of front irradiation mode.

Some of the parameters discussed in the last chapter are important for the discussion of the results. Table 5.1 reports the selected values for the most significant parameters.

Parameter	Value
trigger scheme	2
validation scheme	4
overvoltage	2.0 V
source activity	1.918 MBq
distance to source	43 mm
measurement time	10 min

**Table 5.1:** Selected settings for the front irradiation measurements with singles configuration.

An extra measurement was carried out with the same settings, but with multiple sources. The activity of all the multiple sources sums up to 1.187 MBq.

### 5.1.2 Coincidences Configuration

Coincidences measurements are carried out to reduce the number of events that are not originated by the source. Furthermore, thanks to the coincidences configuration, the time resolution of the HYPMED detector stacks can be tested.

## 5.1. FIRST MEASUREMENTS: FRONT IRRADIATION

Figure 5.2 shows the used experimental setup together with a sketch of the detector stack arrangement and the source for a front irradiation measurement. For the sake of simplicity, the source is centered placed over a  $\gamma$ -transparent material, e.g., foam, at a distance of 43 mm to the sensor tile.

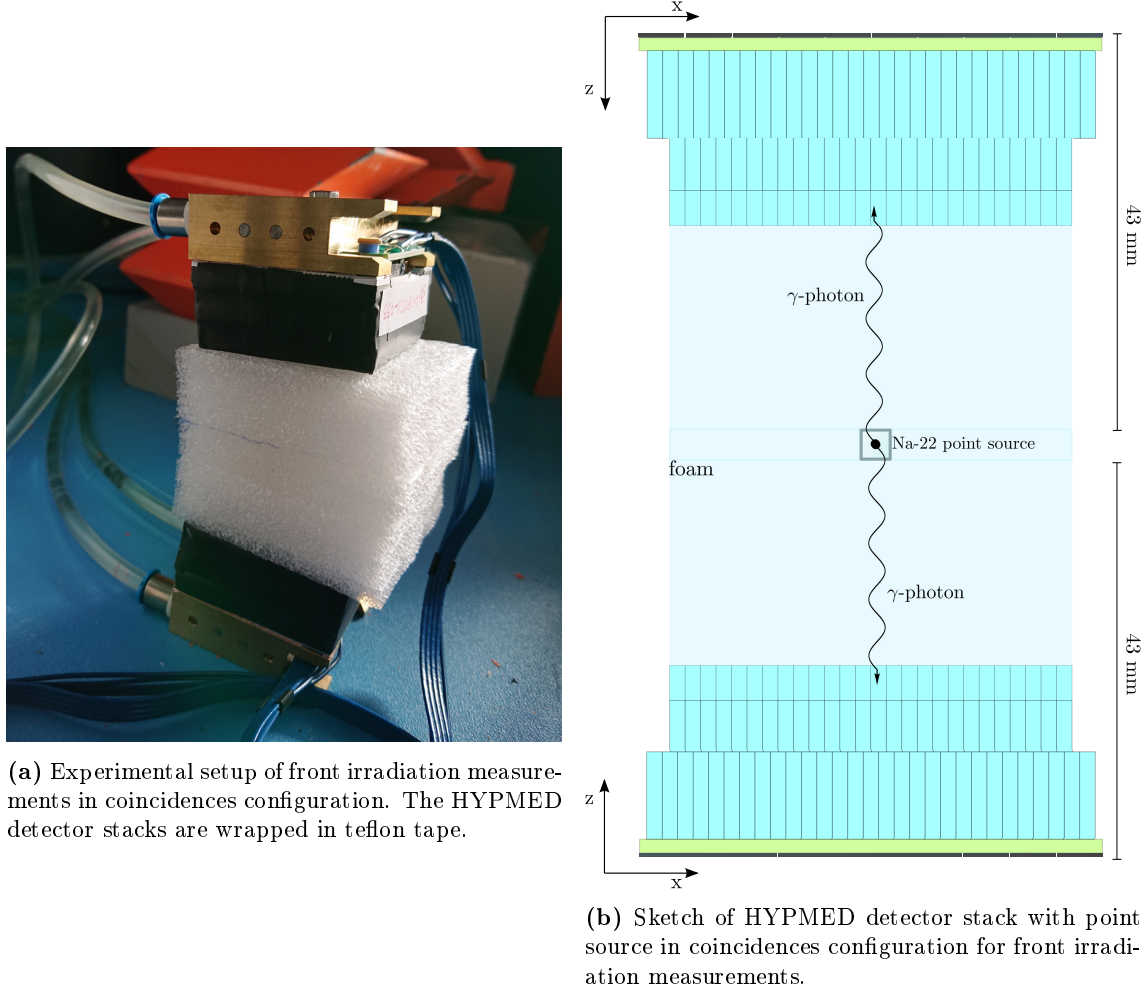


**Figure 5.2:** Coincidences configuration of front irradiation mode.

Moreover, table 5.2 reports the selected values for the most significant parameters in the coincidences configuration.

Parameter	Value
trigger scheme	2
validation scheme	4
coincidence window	20 ns
overvoltage	2.0 V
source activity	1.918 MBq
distance to source	43 mm
measurement time	10 min

**Table 5.2:** Selected settings for the front irradiation measurements with coincidences configuration.

## 5.2. REGION OF INTERESTS

### 5.2 Region of Interests

As mentioned in Section 4.5.3, *hitAnalysis* processes the raw data of the measurements that is generated by the dies of the detector. The dies of interest to be analyzed can be selected by setting conditions to the individual pixels. One condition is the definition of the main pixel depending on the number of optical photon counts ("hottest" pixel) or on the time stamp (first triggered pixel). An extra condition is the number of its surrounding dies to be analyzed. The area covered by the dies to be analyzed is called region-of-interest (ROI).

After the selection of the ROI, the program uses a positioning algorithm, e.g., COG, to return the expected coordinates of the center of the  $\gamma$ -interaction on the xy-plane, which are defined as "cluster". Depending on the chosen ROI, the cluster may differ. This possibility opens a wide range of strategies to select the ROI in order to obtain the correct cluster of the  $\gamma$ -interaction and identify the corresponding scintillating crystal.

Normally, only one ROI per scintillation event is selected [52]. The larger the ROI is, the more optical photons are detected. Thus, choosing a ROI that covers a main pixel with its three neighbouring pixels of different dies can be a good strategy. The respective ROI spans four dies and is labelled as "111" after the acronym HVD, which corresponds to the Horizontal, Vertical and Diagonal neighbouring dies, respectively. A "1" or "0" indicates whether a neighbour is or is not part of the ROI, accordingly.

However, although the three neighbours are analyzed, any of them might have not triggered and thus the cluster is considered invalid. For that reason, the sensitivity of this ROI is lower than that of other ROIs, which consider less neighbours.

Moreover, due to the high number of crystals, some of them may be on the center of the die, between four pixels. Depending on which pixel is the main pixel and assuming that the "111"-ROI is selected, the three neighbouring pixels activate different dies to generate the cluster, as shown in 5.3a. Hence, each of the four sets of active dies induces a different light accumulation point in the flood map for the same scintillating crystal. This effect is called "ghosting" and is shown in Figure 5.3b. It also occurs whenever a crystal is located over two pixels of the same die, but in this case, "only" two light accumulation points per crystal are induced.

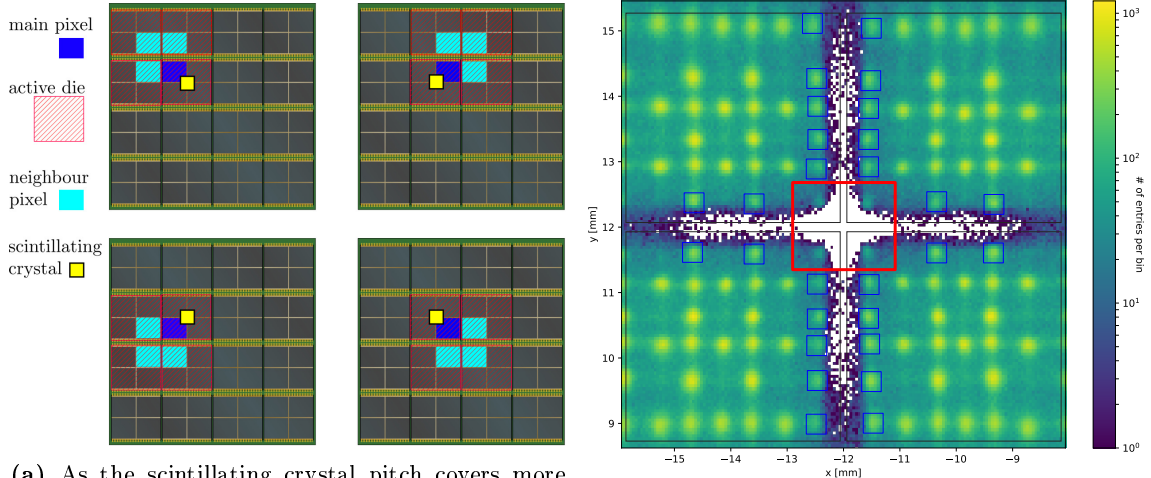
The "ghosting" effect complicates the identification of crystals. As the intensity of one expected light accumulation point is shared by two or four different ones, some of them might not be visible. In that case, the clusters near the invisible light accumulation point are not identified with the crystal. Hence, a lower sensitivity in these crystals is expected. Moreover, the "ghosting" effect may provoke a worse energy calibration, as the count of optical photons may vary from one set of dies to another.

To increase the sensitivity, another ROI should be selected for those scintillation events that could not be identified with the "111"-ROI. However, it is not possible to know a priori to which crystal the  $\gamma$ -photon deposited its energy.

The applied strategy in this master thesis is to analyze complementary ROIs and, a posteriori, decide which ROI is the best one to identify the corresponding crystal per scintillation event. Based on the mentioned "HVD" criterion, namely the neighbours pixels to be considered in the analysis,  $2^3$  possible ROIs can be selected. However, four of them present the best complementary distribution of light accumulation points in the flood maps to compute an identification algorithm. In the following, the four ROIs considered to be the most meaningful are explained. As previously mentioned, one of them shall be the "111"-ROI, which is listed again for completeness:

- **"111"**. The main pixel and its three neighbours are considered to be analyzed. Due to the Anger logic to position the scintillation events (COG), the stable areas of the active dies from this ROI are between four dies. Furthermore, the clusters are well

## 5.2. REGION OF INTERESTS



(a) As the scintillating crystal pitch covers more than one pixel within a die, four areas with different active dies are generated. Every area produces a light accumulation point in the flood map, as shown in Figure 5.3b with a red square. With an illustrative aim, the sensor tile is an array of 4 x 4 dies. Figure adapted from [54].

(b) The "ghosting" effect is represented by the red square and the blue squares. The first one illustrate four light accumulation points for one scintillating crystal in the center of the die. The latter ones show pairs of light accumulation points for scintillating crystals over two pixels within the die.

**Figure 5.3:** (a) Sketch of "111"-ROI with four different areas. (b) Flood map with "111"-ROI showing the light accumulation points in the area over a die.

distributed over the areas and thus, most of the light accumulation points are well defined, as shown in Figure 5.5d. Thereupon, most of the crystals can be assigned to generate the CPM. However, the ROI is not stable on the edges of these areas due to the "ghosting" effect. Moreover, its sensitivity is lower than that of other ROIs as four different dies must be active.

- **"010".** The main pixel and its vertical (HVD) neighbours are considered to be analyzed. Due to the Anger logic to position the scintillation events (COG), the clusters that need the analysis of the two missing neighbours concentrate on the horizontal edges, as shown in Figure 5.5b. Therefore, some of the light accumulation points overlap and cannot be assigned to their corresponding crystals to be part of the CPM. However, the light accumulation points on the center of these areas are complementary to the "111"-ROI, as they do not suffer from the "ghosting" effect. On the contrary, the ROI is not stable on the vertical edges due to the "ghosting" effect. At last, its sensitivity is higher than that of the "111"-ROI as two different dies must be active.
- **"100"** The main pixel and its horizontal (HVD) neighbours are considered to be analyzed. Due to the Anger logic to position the scintillation events (COG), the clusters that need the analysis of the two missing neighbours concentrate on the vertical edges, as shown in Figure 5.5c. Therefore, some of the light accumulation points overlap and cannot be assigned to their corresponding crystals to be part of the CPM. However, the light accumulation points on the center of these areas are complementary to the "111"-ROI, as they do not suffer from the "ghosting" effect. On the contrary, the ROI is not stable on the horizontal edges due to the "ghosting" effect. At last, its sensitivity is higher than that of the "111"-ROI as two different dies must be active.
- **"000"** Only the main pixel is considered to be analyzed. Due to the Anger logic to position the scintillation events (COG), the clusters that need the analysis of

## 5.2. REGION OF INTERESTS

the three missing neighbours concentrate on the edges, as shown in Figure 5.5a. Therefore, most of the light accumulation points overlap and cannot be assigned to their corresponding crystals to be part of the CPM. However, the light accumulation points on the center of these areas are complementary to the "111"-ROI, as they do not suffer from the "ghosting" effect. At last, its sensitivity is the higher than that of other ROIs as only two different dies must be active.

The mentioned areas where the light accumulation points neither suffer from the "ghosting" effect nor overlap with others are called good resolution areas. As explained above, each ROI has its own good resolution area, which are selected to be complementary to each other. The location of scintillating crystals that belong to the good resolution area in every ROI is shown in Figure 5.4.

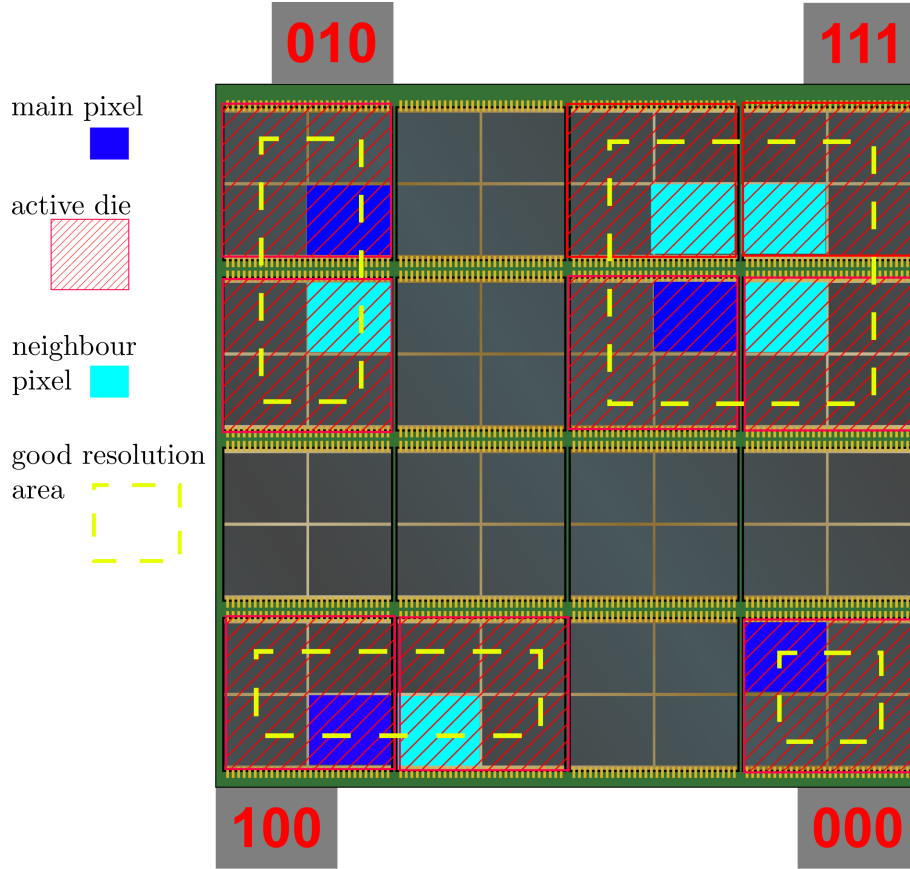


**Figure 5.4:** Sketch of the active areas selected by each ROI depending on the main pixel. The location of scintillating crystals, whose light accumulation points neither suffer from the "ghosting" effect nor overlap with others, is remarked as good resolution area. Each ROI provides a different area that is complementary with the rest. With an illustrative aim, the sensor tile is an array of 4 x 4 dies. Figure adapted from [54].

Each ROI generates its own clusters and thus its own flood maps. Figure 5.5 shows the four generated flood maps in the front irradiation measurement with singles configuration. The flood maps show the different active areas in every ROI. To optimize the workflow, these areas are analyzed individually. Each area contains the corresponding clusters.

An enlarged version of the individual figures in 5.5 are shown in Appendix A.1.1.

### 5.3. CRYSTAL IDENTIFICATION ALGORITHM

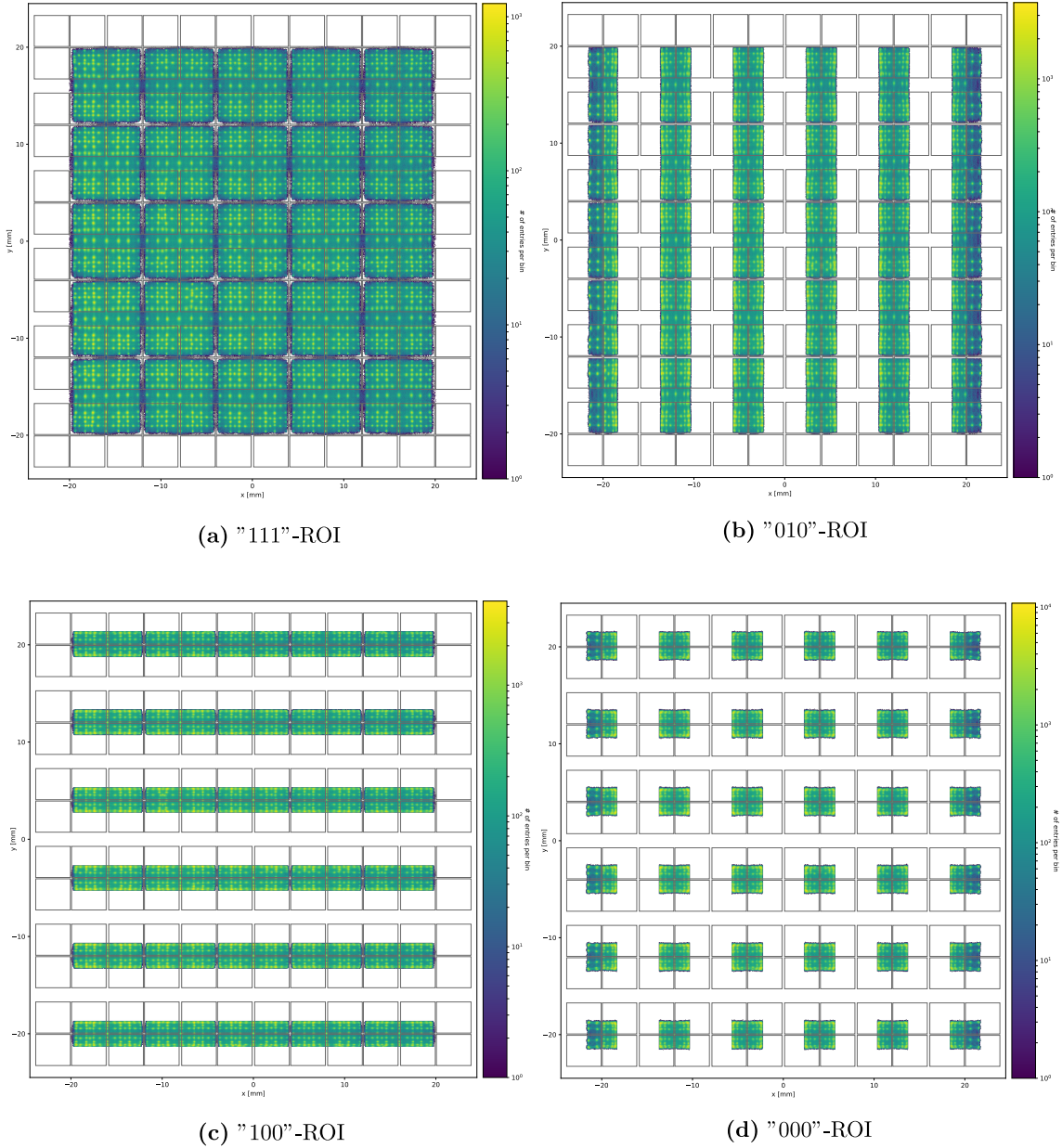


**Figure 5.5:** Generated flood maps of the four most meaningful ROIs.

The analysis of the individual areas in every ROI is explained in the following sections.

## 5.3 Crystal Identification Algorithm

Since four ROIs are employed, four clusters are returned per scintillation event. Hence, four different flood maps are expected. In order to identify the corresponding scintillating crystal to every cluster in each of the flood maps, an individual crystal position map (CPM) per flood map is necessary.

Once the four CPMs are produced, four respective lookup tables (LUTs), which optimize the identification of crystals, are created. Subsequently, several parameters are employed to deduce which of the four identifications per scintillation event is the best one.

### 5.3. CRYSTAL IDENTIFICATION ALGORITHM

#### 5.3.1 Light Accumulation Point Finder

Since the flood maps of the four ROIs are divided, an optimized routine is used to find the light accumulation points in each area separately. The routine is called *SearchHighRes* and is defined in ROOT, a C++ software developed by CERN [7]. To include it in our program, the python interface of ROOT was used: PyROOT.

In the following paragraphs, a brief description of the routine with its input parameters is given. The given information is extracted from [48] and [45], which provide an extended description of the used routine.

*SearchHighRes* is a 2D peak search function that is based on the deconvolution method. In this thesis, the peaks correspond to the light accumulation points. The first step of the routine is to remove the background of the histogram to be analyzed, if the corresponding flag is activated. The removal depends on the peak with the highest intensity of the area selected from the flood map. The user selects the percentage of intensity (threshold) that is removed based on that peak. The second step is to calculate the response function of the remaining data according to a given sigma. The sigma corresponds to the accepted width of the peaks. With a higher sigma, the routine accepts wider peaks. On the contrary, with a smaller sigma, the routine searches for narrower peaks. At last, the gold deconvolution algorithm runs through as many iterations as the user has previously selected.

In the *SearchHighRes* routine, the input parameters can be varied and the output deconvolved data can be accessed. Therefore, in every ROI, the input parameters were tuned according to the output data, which are shown in Table 5.3. Two exceptions are the selection of the background removal, which is always activated, and the number of iterations of the deconvolution algorithm, which is set to 200 on all the ROIs. Additionally, a smoothing filter is deactivated.

ROI	Sigma [a. u.]	Threshold [%]
000	3.3	2
010	2.5	6
100	1.5	7
111	1.5	4

**Table 5.3:** Input parameters used in the *SearchHighRes* routine in the different ROIs. The unit of sigma are defined with respect to the center of the peak and its magnitude. The percentage of the threshold is with respect to the peak with the highest intensity.

These values are optimized for the flood maps generated by the front irradiation measurement with singles configuration. However, they are also successfully employed in the other front irradiation measurements, i.e., with another detector stack and in coincidences configuration.

The output data is an array of the "x" and "y" coordinates from the found peaks, which are plotted in the individual flood maps to visually check that they correspond to the light accumulation point. With the selected parameters, the peaks within the good resolution area are detected, unless the crystal presents some defect. Some examples of the obtained results in every ROI are shown in Figure 5.6.

### 5.3. CRYSTAL IDENTIFICATION ALGORITHM

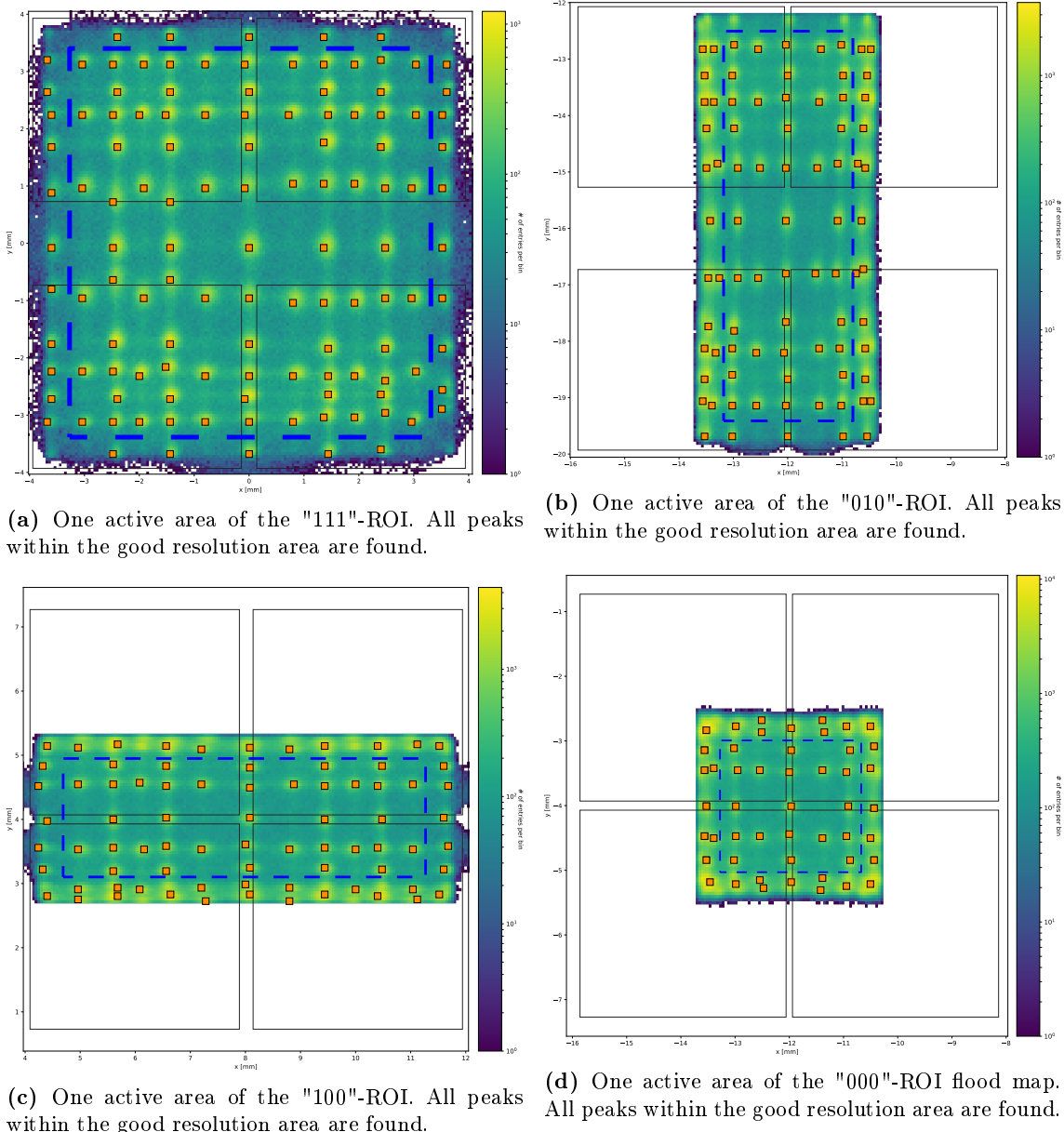


**Figure 5.6:** Found peaks (light accumulation points) in the four flood maps from the selected ROIs. One active area is shown for better visualization. The blue dashed lines remark the good resolution area.

#### 5.3.2 Crystal Position Map Construction

The map with all the crystal positions in the different flood maps is created by analyzing every active area individually. The peaks within it are sorted and assigned to the corresponding crystals. Then, the assignment is compared with the whole flood map and corrected, if necessary.

For the sake of a clear explanation, the "111"-ROI is taken as reference to describe the following steps in the algorithm. In the final step (see Section 5.3.3), the results for all the ROIs are shown.

The output peaks of a single active area in the "111"-ROI are ordered according to their coordinates in "y"-direction. With this order, groups of peaks, which belong to the same row, can be sorted.

In Figure 5.6a, the number of peaks of one row can be deduced. No row contains more

### 5.3. CRYSTAL IDENTIFICATION ALGORITHM

than 20 peaks. Therefore, to create the group of rows, sets of 20 peaks are sorted with respect to their coordinates in "x"-direction.

An iteration check is run over the set of 20 peaks. The closest one to the left top corner (maximum "y" coordinate and minimum "x" coordinate) is chosen as reference for the row. The next peak of the row must be within a preset range of the "y"-axis to be added to the row. This range is defined as the "y" position of the previous peak  $\pm 0.2$  mm. With this method, the range adapts itself to the possible variations within the row that may occur. If the following peak is not within that range, it is saved for the next iteration. A scheme of this iteration is shown in Figure 5.7.

Note: the maximum and minimum values of the range vary from 0.1 mm to 0.2 mm.

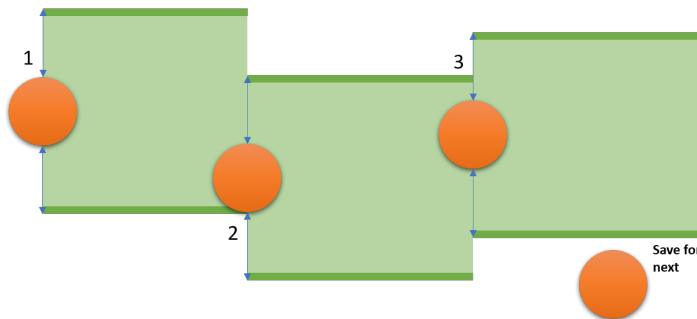


**Figure 5.7:** Scheme of iteration to separate the peaks into sets of rows. The green area shows the accepted range for the row.

This iteration is repeated 20 times because no more than 20 rows per active area are expected.

The result of this method for sorting rows is shown in Figure 5.8b. The next step is to assign crystal labels to the sorted peaks. In case any peak is not included in a row, it is saved for the second part of the algorithm, see Section 5.3.3.

#### Labels of Crystals

In order to assign the corresponding crystals to the peaks of the different active areas, at least one reference per active area is needed. That means, it is necessary to assign a priori the label of one crystal to one of the peaks in every active area. Subsequently, the rest of the peaks within the active area can be assigned as the distribution of the crystals is known.

Firstly, the crystals must be labelled to assign them to the peaks. As the orientation of the scintillator is consistent throughout the measurements, the labels are defined based on the geometrical disposition of the crystals. The expected orientation can be observed in Figure 4.4.

The labels are numerical and range from "0" up to "3424". The label "0" is given to the crystal at the top left corner corresponding to layer "1". The next labels are assigned in ascending order along the "x" axis. Once the first row of crystals from the first and second layers is labelled, the labels continue with the next row of crystals from the third layer. The last crystal at the bottom right corner is labelled as "3424".

Furthermore, the row and column indexes are saved together with the label. All the layers share the same row index, from "0" at the top until "70" at the bottom, which gives 71 rows in total. However, the column index is different for the third layer with respect to the other two layers. For the third layer, the column index reaches up to "30", as there are 31 columns in total for this layer. For layers 1 and 2, the column index reaches up to "64", as there are 65 columns in total counting both layers.

### 5.3. CRYSTAL IDENTIFICATION ALGORITHM

A relation between the column indexes is given in Equation 5.3.1, where  $i_{12}$  corresponds to the column index of the labels from the layers 1 and 2, and  $i_3$  to the column index of the labels from the third layer.

$$i_{12} = i_3 \cdot 2 + 2 \quad (5.3.1)$$

#### First Assignment

Once all the crystals possess their respective label, the reference crystal in every active area is assigned.

Due to the used positioning algorithm (COG), the position of the peak in the center of the active area coincides with the actual geometrical position of the crystal. Figure 5.8 shows the geometrical disposition of crystals over the expected active area of the "111"-ROI and the corresponding peaks found. Hence, the closest peak to the center of the active area is selected to be labelled with the respective reference crystal. Subsequently, the reference crystals for all the active areas are previously defined.

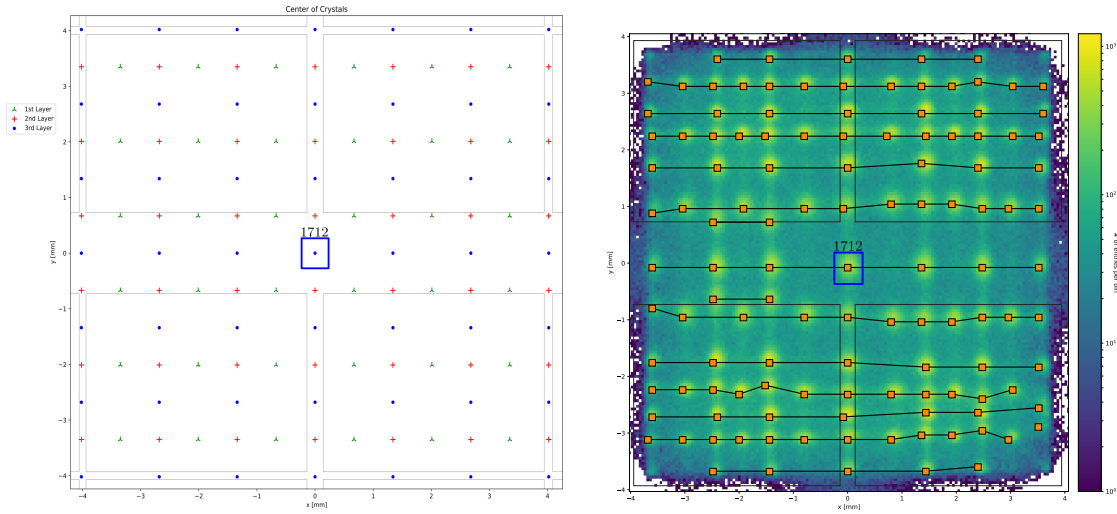


**Figure 5.8:** The crystal label ("1712") of one of the first assignments is shown. The position of the geometrical position of this crystal corresponds with its light accumulation point if the "111"-ROI is used to position its scintillation events.

Note: all the reference crystals from the four ROIs belong to the third layer.

#### Further Assignments

Using the peak in the center as reference, the rest of the peaks from the active area is assigned running an iteration along the rows and towards the edges.

Assuming that the reference peak is correctly assigned, the peaks on the same row are assigned and marked as valid. Thereafter, the centered peak of the next row with respect to the reference, which belongs to the second layer, is assigned. Then, the assignment process is run iteratively for the rest of the rows analogously. If any row presents a problem, such as a higher or smaller number of expected peaks, the peaks are not assigned and are marked as invalid.

### 5.3. CRYSTAL IDENTIFICATION ALGORITHM

The crystal labels are iteratively assigned in every active area and the assignments are saved in a common python dictionary for every ROI. To deal with the "ghosting" effect, one crystal can be assigned more than once to peaks from different active areas. Moreover, as the "ghost" peaks can be previously defined, these assignment are checked afterwards, as explained in Section 5.3.3.

To distinguish the crystals from the different layers, the main crystal reference can be used as a guide. As observed in Figure 5.8a, it belongs to the third layer and thus the crystals from the same row belong to the third layer. Moreover, the closest peaks to it from the other rows belong to the second layer, and so forth. A simplified flow chart of the CPM construction is shown in Figure 5.9.

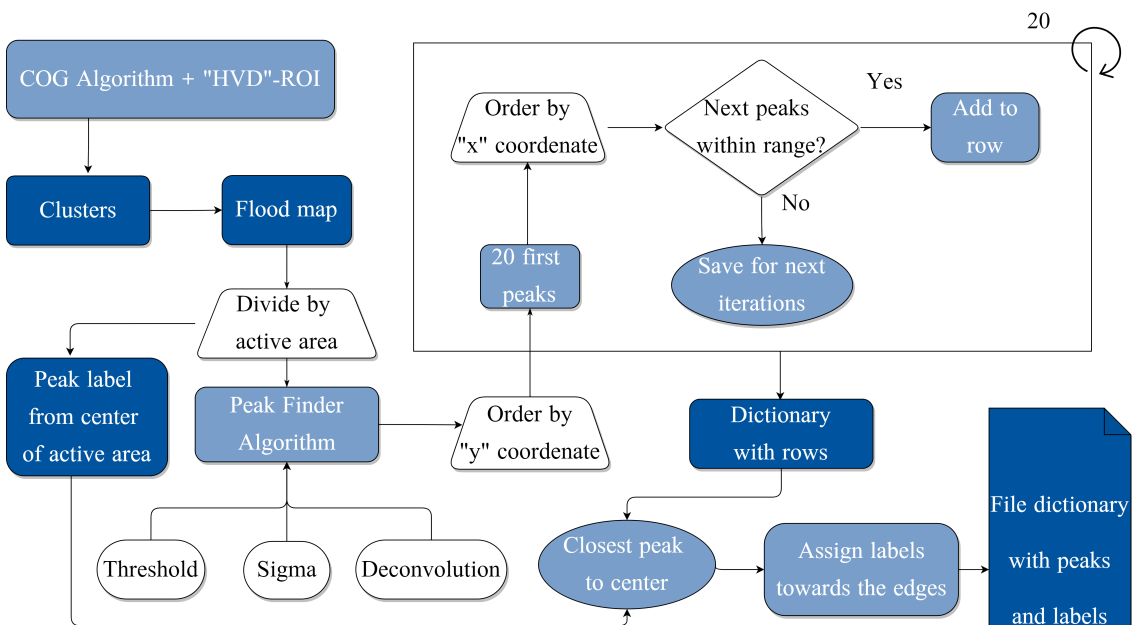


**Figure 5.9:** Flow chart of the first part of the CPM construction.

The last step for this part is to plot the CPM to check visually whether it assigns all the peaks correctly. Figure 5.10 shows a part of the first constructed CPM. Nonetheless, in the next step, all the assignments are checked to ensure that they match the assignments of the other active areas and the whole CPM is analyzed to confirm the correct distribution of the labels.

#### 5.3.3 Crystal Position Map Tweaking

Once the CPM is constructed, some of the peaks may not be assigned correctly or may not have an assignment. In order to improve the assignments, the CPM is tweaked. Firstly, all the assigned peaks from all the active areas are analyzed together. The medians of the different columns from the valid assignments are calculated. In case they are within the specific range defined as median of column  $\pm 0.3$  mm, they are confirmed as valid. If that is not the case, the peak is marked as invalid. Thereafter, an analogous procedure using the medians of the rows is executed.

Note that the maximum and minimum values of the column range vary from 0.15 mm to 0.3 mm. The maximum and minimum values of the row range vary from 0.2 mm to 0.4 mm.

Subsequently, the closest column and row of the peaks that are not valid or do not have any label are calculated. If the corresponding row and column lead to a label that

### 5.3. CRYSTAL IDENTIFICATION ALGORITHM

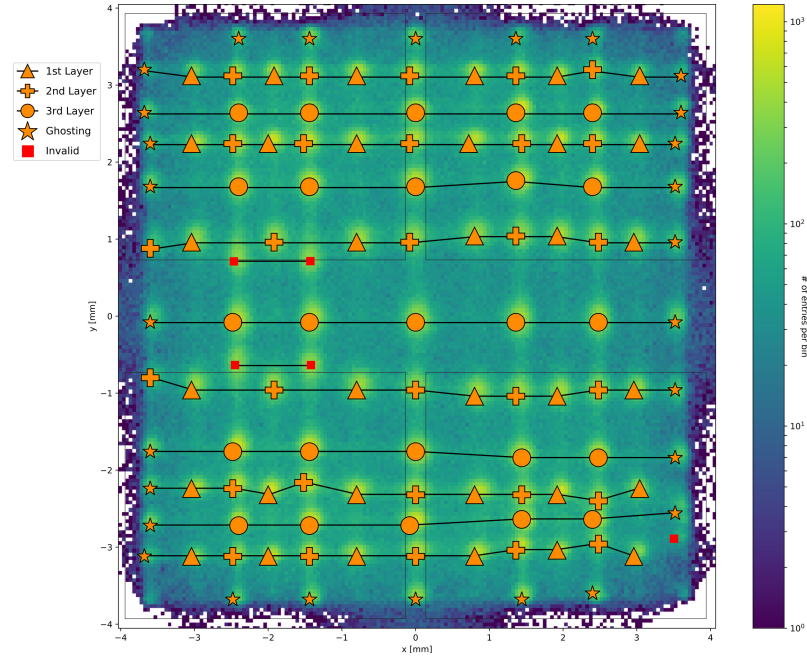


**Figure 5.10:** Part of the CPM from the centered active area of "111"-ROI. The invalid labels correspond to unassigned peaks.

is empty, the peak is assigned to it. If the label contains a peak, both peaks are checked individually to determine whether they are within the specified range. The closest one is marked as valid and the other one as invalid. A new common python dictionary per ROI is created including the corrected labels.

A simplified flow chart of the CPM tweaking is shown in Figure 5.11.

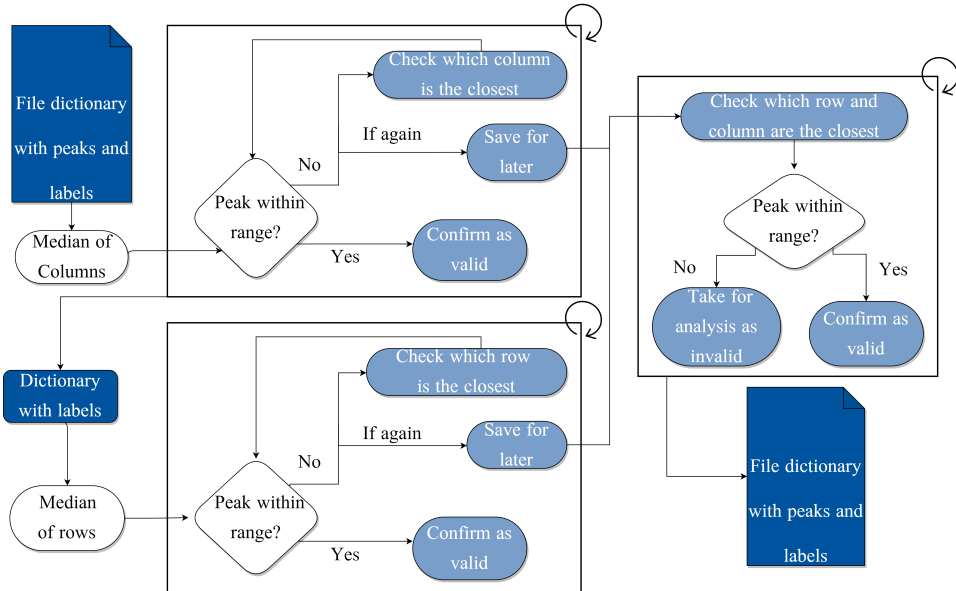


**Figure 5.11:** Flow chart of the CPM tweaking.

While Figure 5.12 shows the final CPM in the same active area as in Figure 5.10, in Figure 5.13 the final CPM of the four different ROIs can be found. An enlarged version of the individual figures in 5.13 are shown in Appendix A.1.2.

### 5.3. CRYSTAL IDENTIFICATION ALGORITHM

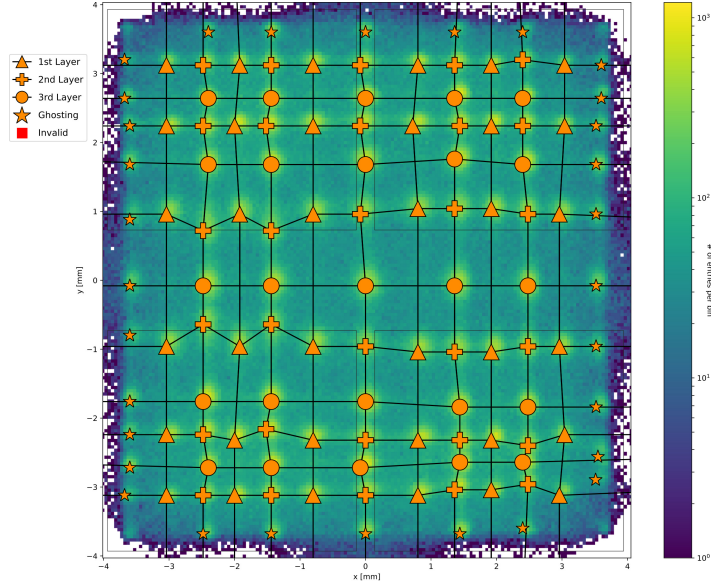


**Figure 5.12:** Part of the final CPM from the centered active area of "111"-ROI connecting the crystal positions by columns and rows. The invalid labels correspond to unassigned peaks.

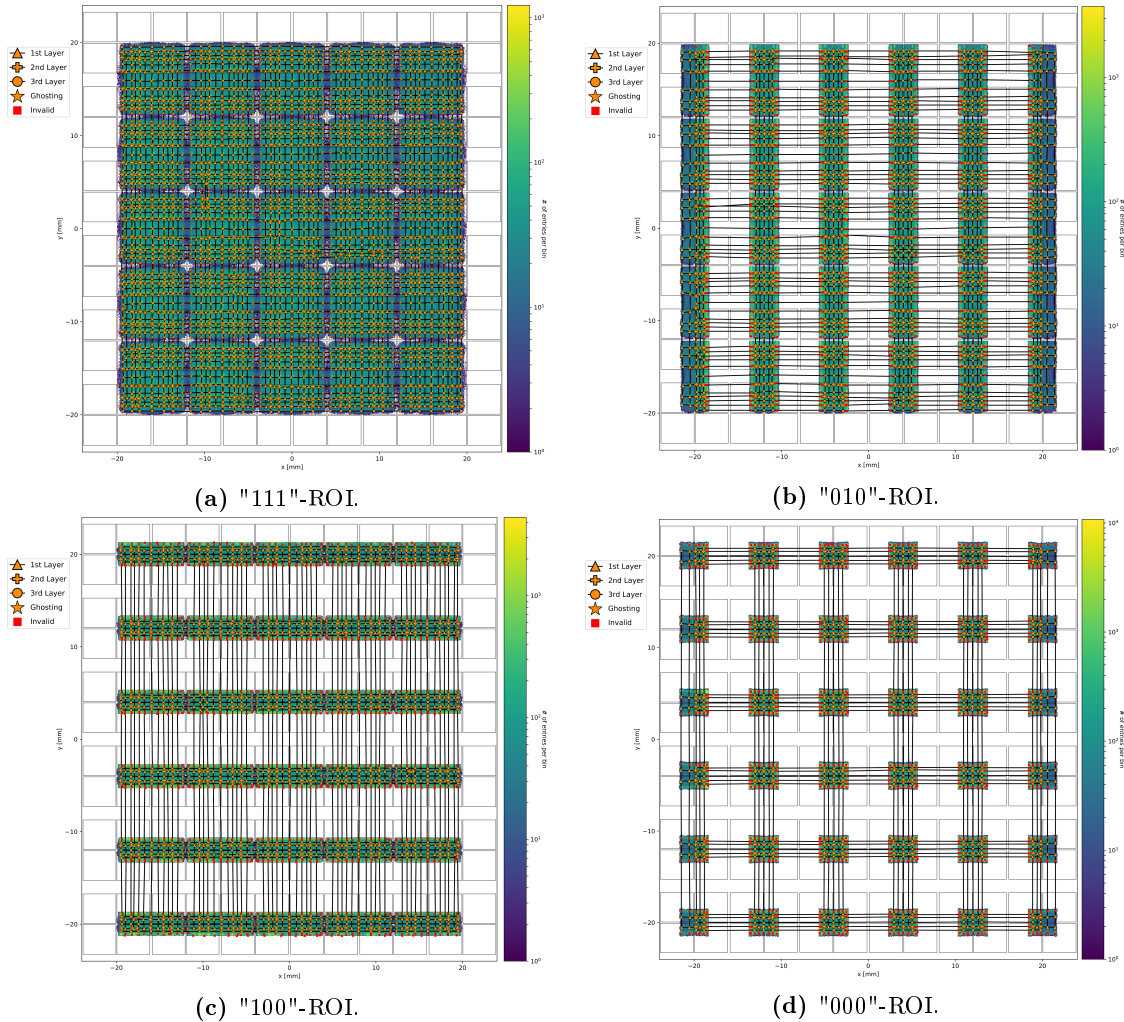


**Figure 5.13:** Final CPM connecting the crystal positions by columns and rows. The invalid labels correspond to unassigned peaks.

### 5.3. CRYSTAL IDENTIFICATION ALGORITHM

#### 5.3.4 Segmentation of Flood Maps: Look Up Table

A crystal identification of the clusters can be carried out with the four different dictionaries of labels. The algorithm iterates over all the cluster from the different ROIs and identifies them with the corresponding crystal. To achieve this, the cluster of each ROI can be plotted in the flood map and with the help of the CPM, the closest peak to the cluster is determined. Since there are 100 million of clusters for the front irradiation measurement with singles configuration and thousands of assigned crystal labels per flood map, this process can last days. To speed it up, a look up table (LUT) is created for each of the four CPMs.

The LUT consists of a grid with a resolution of 0.01 mm covering the area of the CPM. Each coordinate of the grid is analyzed to find the closest peak in the corresponding CPM. In fact, the two closest peaks are saved in the LUT together with their respective distances for posterior analysis.

In order to analyze the good resolution area of each ROI, the LUT can be reduced to only the area that contains the valid peaks of the CPM. To achieve this, the convex hull of the valid peaks is calculated. The "ghost" peaks are outside the convex hull and thus a small grid of radius 0.3 mm is defined around them. Figure 5.14 shows the LUT in one of the active areas from the CPM of the "111"-ROI.

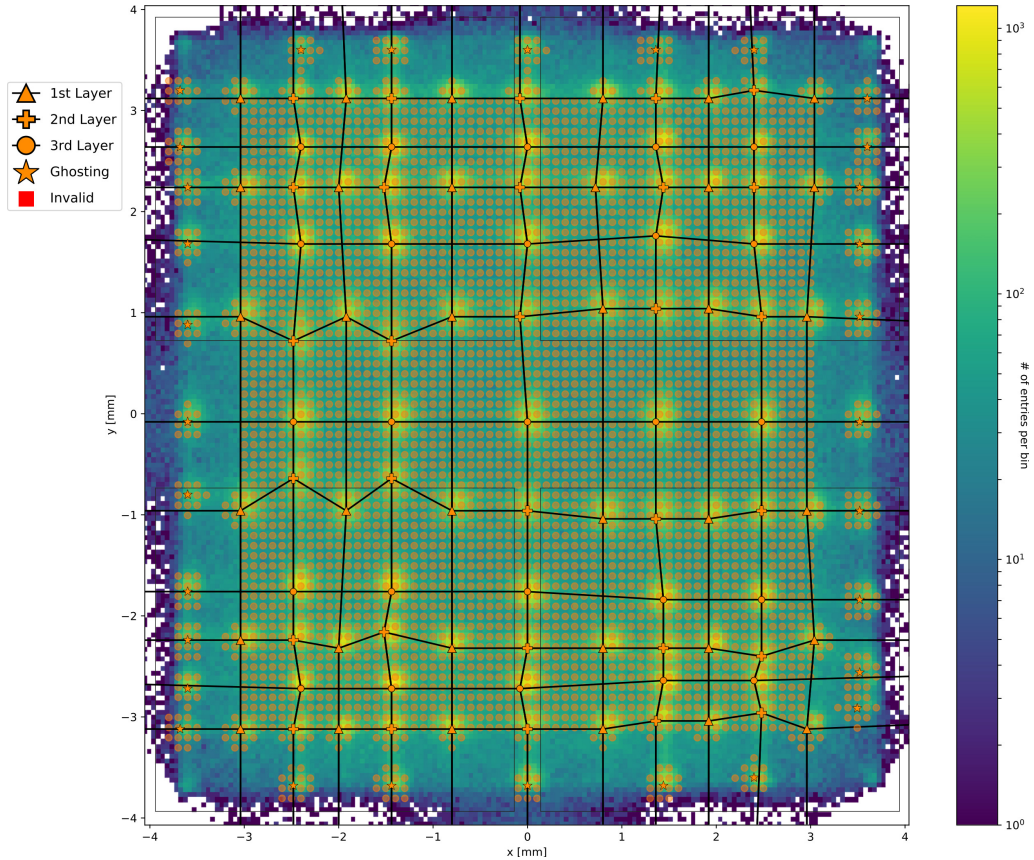


**Figure 5.14:** Flood map of an active area of the "111"-ROI with dwarfed markers for the CPM and enlarged markers for the LUT. The LUT is represented by the shadowed orange circles which cover the convex hull of the valid peaks and a small radius around the peaks outside of the convex hull.

In case only the clusters close to the valid peaks shall be analyzed, the LUT can be further reduced to a small radius around the valid peaks. Hence, the clusters that are not clearly identified with one scintillating crystal are rejected. Thus, it is especially important to calculate the energy resolution of the detector stacks, as explained in Section 6.1.

### 5.3. CRYSTAL IDENTIFICATION ALGORITHM

#### 5.3.5 Crystal Identification

Once the CPMs for each ROI are constructed, an iteration is run over the scintillation events. In every scintillation event, up to four clusters might be calculated if the expected active dies of the respective ROI are available. Then, a crystal identification algorithm is applied to the obtained clusters. With the crystal identification, up to four possible scintillating crystals that may have caused the measured light pattern are returned. Subsequently, the scintillating crystal is decided among these four crystal candidates.

When iterating over the scintillation events, the four corresponding clusters are rounded to the selected resolution of the LUTs. Every cluster is analyzed separately. For example, if the respective coordinates of one cluster from the "111"-ROI are within the accepted area (either convex hull or close to a valid peak) of the "111"-LUT, the information contained in the LUT for these coordinates is returned. This information consists of the label for the closest peak, i.e., crystal, a flag indicating whether it is a valid or "ghost" peak, and the distances from the two closest peaks to the coordinates. If the coordinates of the respective cluster are not within the accepted area, the scintillating crystal cannot be identified for this cluster. Therefore, the information regarding its position and the closest peak is stored, but marked as invalid.

In case the different LUTs that provide a valid crystal label return the same crystal label, the labelled crystal is considered as the scintillating crystal. As long as more than one crystal label is available and they do not match, the crystal labels are saved for further analysis.

The next step is to compare the saved crystal labels. When more than the half of them agree on one crystal, this crystal label is considered as the scintillating crystal. If there is no agreement, an extra parameter is needed.

To define this parameter, two assumptions are considered. The clusters close to a peak (crystal) are assumed to be "good quality" clusters, as their corresponding crystal is easy to identify and the clusters further away from any peak (crystal) are assumed to be "bad quality" clusters, as their corresponding crystal is not easy to identify.

With these assumptions, the parameter can be defined measuring the distance between the clusters and their corresponding crystal, given by the LUT. However, the absolute distances cannot be compared among LUTs, as the gaps between the peaks in the "000"-LUT are smaller than the gaps in the "111"-LUT. Therefore, a relative quantity to compare the distances among the LUTs is needed.

To achieve that, each of the four LUTs provides the distances from the two closest peaks to the respective coordinates. With the lowest distance ( $d_1$ ) and the second lowest distance ( $d_2$ ) to valid peaks, a "quality" factor (QF) is defined in Equation 5.3.2. The QF indicates how close a cluster is to one peak in comparison with the other peak.

$$QF = \frac{d_1}{d_1 + d_2}, \quad QF \in [0, 0.5] \quad (5.3.2)$$

With the help of the QF, the "quality" of the crystal identification can be compared among the LUTs. The lower the QF, the better the crystal identification for the cluster, because the distance to the first peak is smaller than the distance to the second peak, relatively. When the distances are similar, the crystal is not clearly identified for the cluster and thus a larger value of QF is returned. In case the identified crystal label corresponds to a "ghost" peak, the QF is "punished" with an increase of 20 %.

Therefore, when the conditions explained before are not enough to identify the scintillating crystal, the QF shows which crystal label should be considered to be selected as scintillating crystal.

## 5.4. RESULTS AND DISCUSSION

### 5.4 Results and Discussion

In this section, the obtained CPMs and the crystal identification of scintillation events are discussed and verified.

Figure 5.13 shows the CPMs that correspond to the flood maps generated with the COG algorithm with the four employed ROIs for the front irradiation measurement with singles configuration. Due to its large area of good resolution, the CPM of the "111"-ROI is able to assign a high number of crystals to the found peaks. In total for that CPM, 2853 out of 3425 crystals are assigned including 556 crystals that suffer from the "ghosting" effect. The remaining 572 crystals are located at the edges of the scintillator and are not assigned because their corresponding light accumulation points do not appear on the respective flood map. This happens because of the conditions imposed by this ROI. On the other hand, the CPMs from the "010"-ROI, "100"-ROI, and "000"-ROI are able to assign 1353, 1283, and 648 out of the 3425 crystals including 96, 180, and 0 that suffer from the "ghosting" effect. The total number of crystals assigned at least once in any of the CPMs is 3105, which is approximately 91% of the crystals from the tested HYPMED detector. This percentage of assignments remained constant when the other available detector stack was tested.

The remaining 9% of crystals (320) belong to the three first and last rows of the scintillator. They are not assigned due to the overlap of their corresponding light accumulation points on the analyzed flood maps where they appear ("000"-ROI and "100"-ROI), as shown in Figure 5.15.

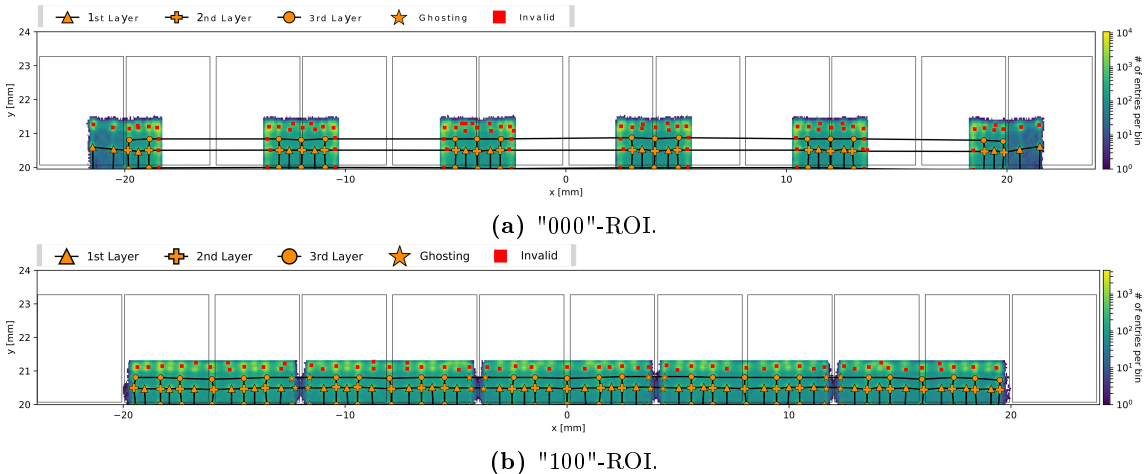


**Figure 5.15:** Overlap of light accumulation points of the three first rows in the flood maps from two of the ROIs.

A first verification of the CPMs from the four ROIs is done by visually observing whether the assigned crystal labels are correctly distributed over the flood maps. As the reference crystal labels are always correctly labeled, the layer markers assigned to the crystals can confirm that the distribution of labels is as expected. As shown in Figure 5.13, the labels from the four CPMs are correctly distributed.

Due to the isotropic emission of pairs of  $\gamma$ -photons by the employed source, a relatively homogeneous distribution of the scintillation events is expected. From this fact, two possible verifications of the crystal identification algorithm are derived. Firstly, the number of scintillation events that share the same identified crystal shall be approximately equal. Secondly, the scintillating crystal shall be identified in around 91% of the scintillation events produced by the  $\gamma$ -photons emitted by the source.

In total, 100 million scintillation events were stored in the front irradiation measurement with singles configuration. Figure 5.16 shows the crystal map with the number of

## 5.4. RESULTS AND DISCUSSION

scintillation events per crystal in this measurement.

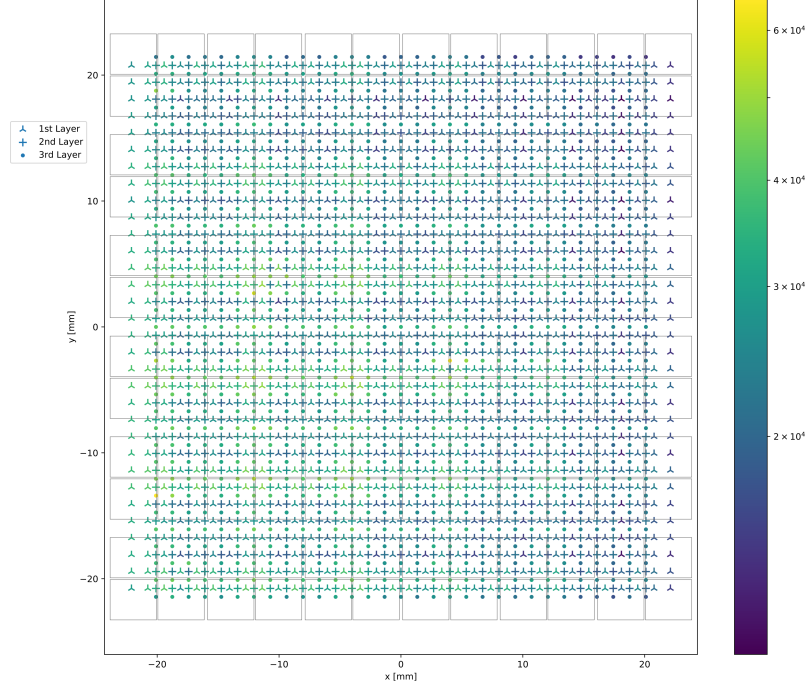


**Figure 5.16:** Number of scintillation events in each crystal label in logarithmic scale. Front irradiation measurement with singles configuration and one point source. The three first and last rows are excluded, as their crystals are not analyzed.

In total, 80 million scintillation events were stored in the front irradiation measurement with coincidences configuration. Figure 5.17 shows the crystal map with the number of scintillation events per crystal in this measurement.

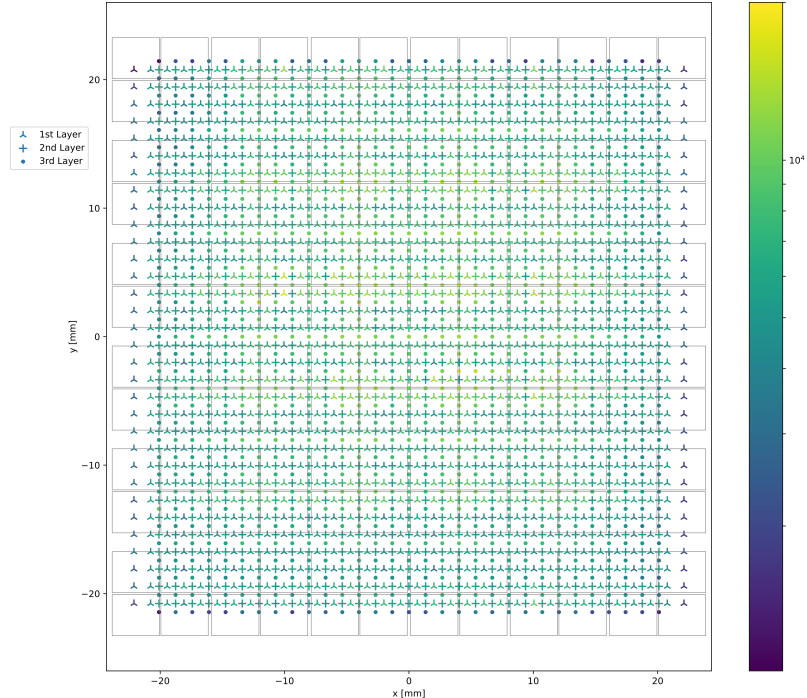


**Figure 5.17:** Number of scintillation events in each crystal label in logarithmic scale. Front irradiation measurement with coincidences configuration and one point source. The three first and last rows are excluded, as their crystals are not analyzed.

## 5.4. RESULTS AND DISCUSSION

A crystal label, which may correspond to the scintillating crystal, is returned in around 85% and 90% of the stored scintillation events for the singles and coincidences configurations, respectively.

In both crystal maps the position of the source is observed. Figure 5.16 shows that the source was slightly shifted from the center towards the lower left corner and Figure 5.17 shows that the source was correctly placed.

To check whether this shift is indeed produced by the location of the source, an extra measurement with multiple sources in the front irradiation measurement with singles configuration was carried out. In total, 150 million scintillation events were stored in this measurement and Figure 5.18 shows its crystal map with the number of scintillation events per crystal.

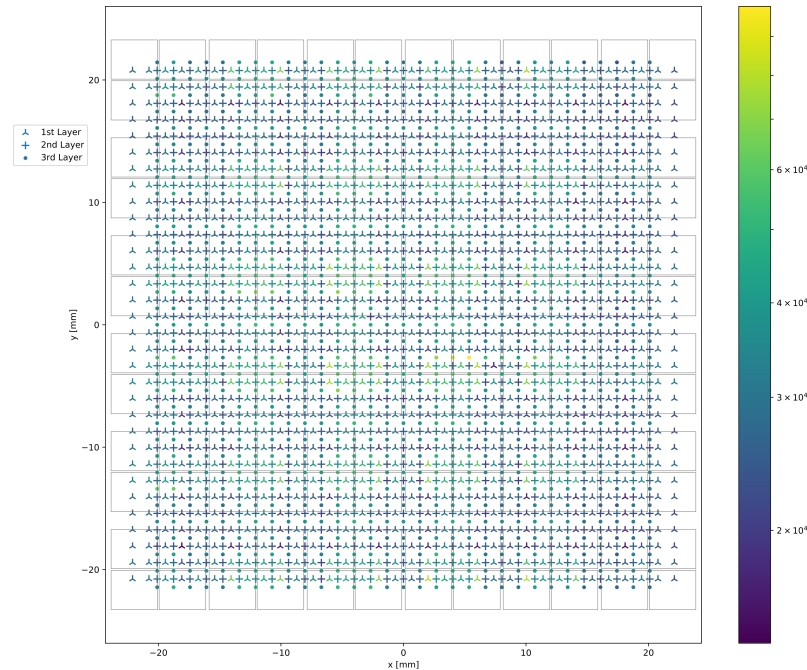


**Figure 5.18:** Number of scintillation events in each crystal label in logarithmic scale. Front irradiation measurement with singles configuration and multiple point sources. The three first and last rows are excluded, as their crystals are not analyzed.

A crystal label, which may correspond to the scintillating crystal, is now returned in around 85% of the stored scintillation events and the shift caused by the single source is no longer visible now.

In addition, a trend is discernible in all the crystal maps shown. Although most of the crystals have a similar number of scintillation events depending on the total number of stored scintillation events, a relatively higher number of scintillation events is observed in the crystals above the center of the dies.

Another possible verification of the crystal identification algorithm is to plot the clusters that correspond to each crystal label separately in each of the available four selected flood maps. It may occur that the clusters of one crystal label, e.g., "1712", are only available in one of the selected flood maps (corresponding to the "111"-ROI), as shown in Figure 5.19b. In this case, all the clusters should be confined around the light accumulation point, as the identified crystal in the "111"-LUT is the selected crystal label.

If the clusters are available in more than one of the selected flood maps, e.g., in the crystal label "1714", they are still plotted even if their crystal labels do not match with the selected crystal label as long as they are valid (see Section 5.3.5). The clusters whose crystal labels do not match with the selected crystal label are likely further apart from

## 5.4. RESULTS AND DISCUSSION

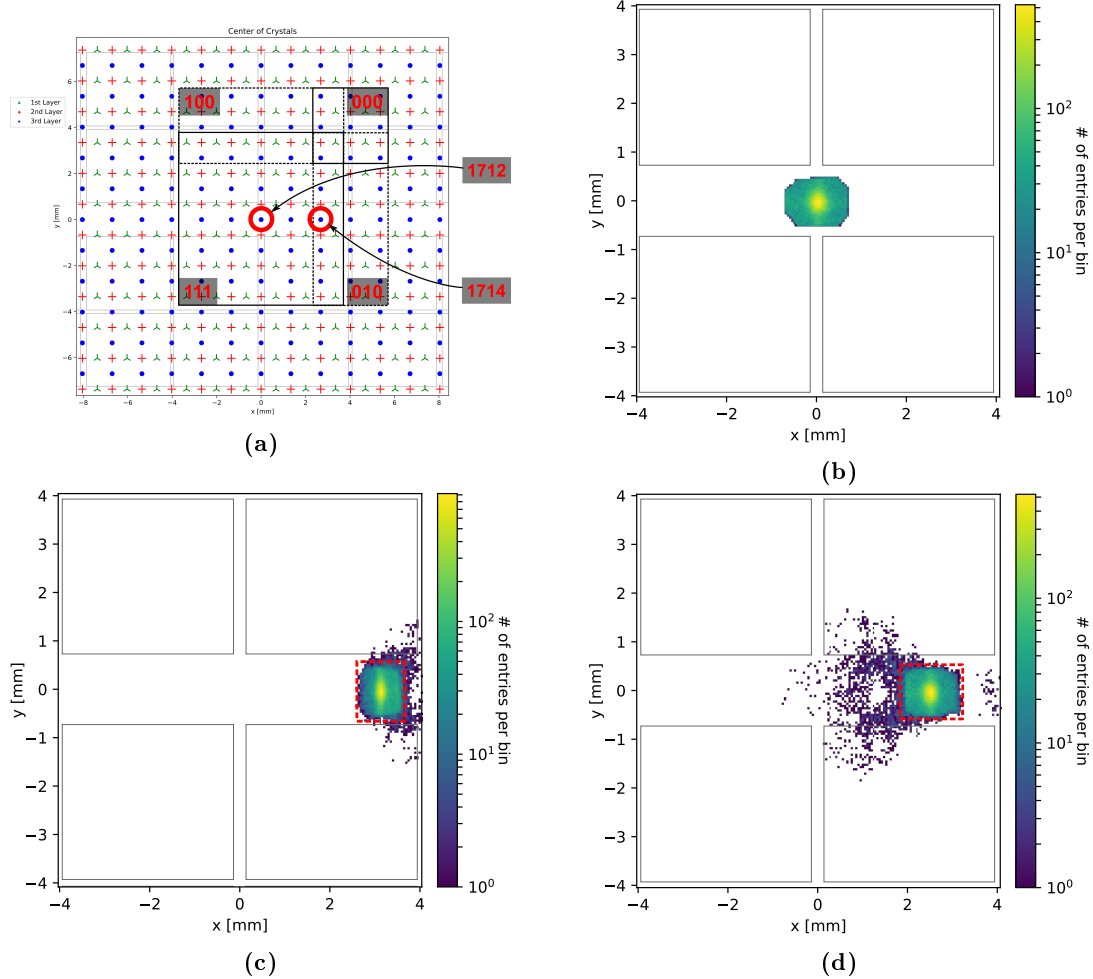


**Figure 5.19:** (a) Geometrical position of the selected crystals: "1712" and "1714". The black dashed and solid lines represent the good resolution areas of the corresponding ROIs. (b) Flood map with calculated clusters of scintillation events whose identified crystal label is: "1712" ("111"-ROI flood map). (c) and (d) "010"-ROI and "111"-ROI respective flood maps with calculated clusters of scintillation events whose identified crystal label is: "1714". The red dashed square limits the area where the identified crystal in the LUT of the corresponding ROI most likely matches the selected crystal for the corresponding scintillation event. Probably, the crystal labels of the clusters outside this area do not agree with the selected crystal label.

the light accumulation point, as shown in Figures 5.19c and 5.19d. Nevertheless, the clusters should still be mostly concentrated in the respective light accumulation point of the selected crystal label if the crystal identification algorithm works for most of the corresponding scintillation events.

In addition, a more practical method to confirm that the crystal identification algorithm is reliable and identifies the correct crystal in most of the scintillation events is the following. The clusters that correspond to crystal labels from the same layer separately in each of the four selected flood map are plotted. The clusters should be concentrated in the respective light accumulation points, i.e. crystals, of the selected layer. Figure 5.20 shows the four selected flood maps only with the clusters whose identified crystal label belong to the third layer, regardless of the LUT that was used to provide the crystal label. This means that up to four calculated clusters are plotted even if their crystal labels do not match with the selected crystal label as long as they are valid, as explained in Section 5.3.5.

An enlarged version of the individual figures in Figure 5.20 is shown in Appendix A.1.3.

## 5.4. RESULTS AND DISCUSSION

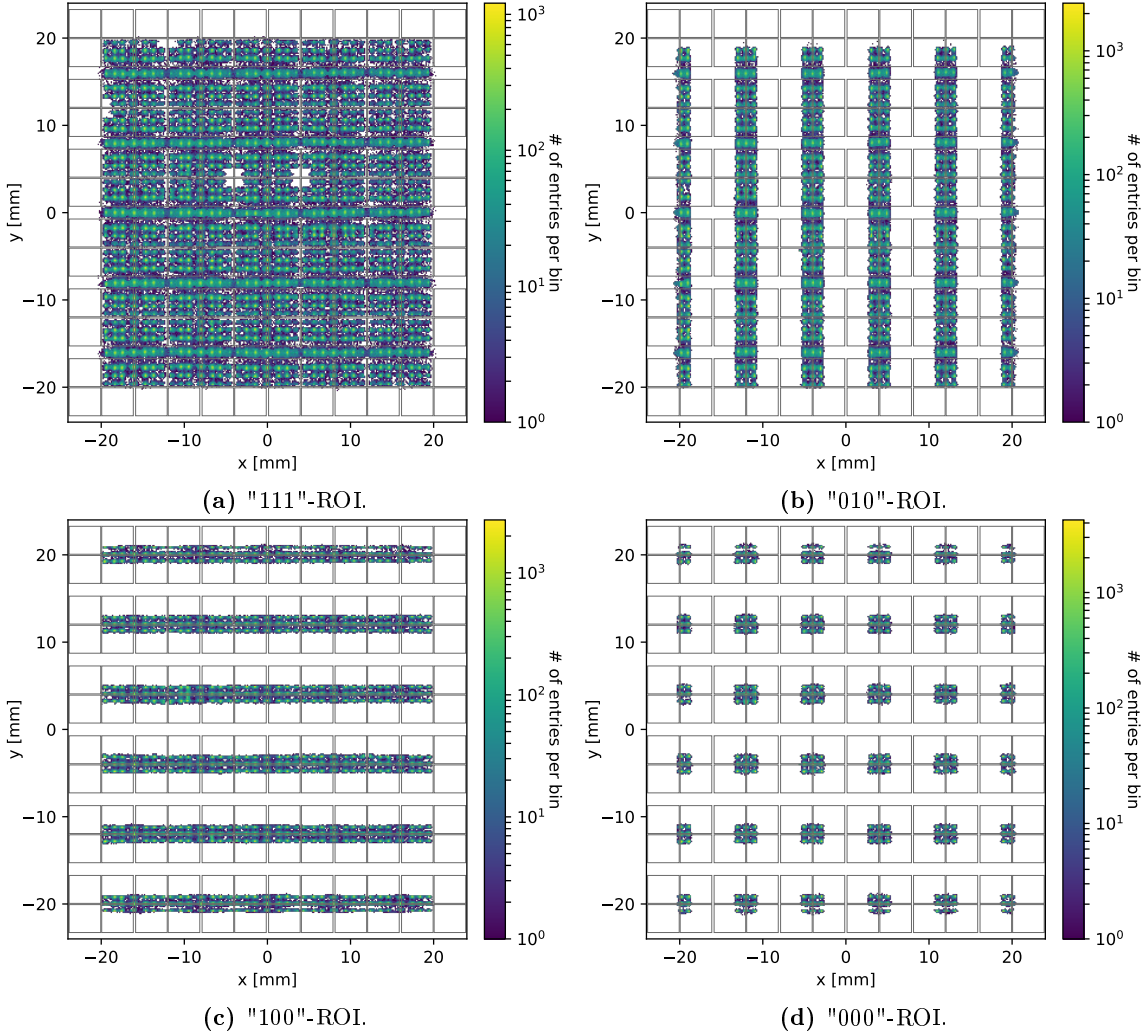


**Figure 5.20:** Flood maps of the four different ROIs with calculated clusters of scintillation events whose identified crystal labels belong to the third layer.

As observed in Figures 5.20, the light accumulation points that correspond to the crystal labels of the third layer can be distinguishable. However, due to the clusters that do not agree with the selected crystal label, clusters in the area between the light accumulation points are also visible.

## 5.5. CONCLUSION AND OUTLOOK

### 5.5 Conclusion and Outlook

The four selected ROIs have proven to be complementary in assigning most of the crystals with the four respective CPMs. The presented method for constructing the CPMs is able to reliably assign the crystals automatically and to easily check the assignments visually. It is also able to adapt to different ROIs with a simple parameter adjustment and its results show that no manual correction is necessary. In addition, it is capable of coping with the explained "ghosting" effect.

The algorithm can be further enhanced to handle the unassigned crystals in the three upper and lower rows, which are currently not distinguishable in neither of the four selected flood maps. One possibility may be to tune the parameters of the peak finder algorithm individually to distinguish the light accumulation point outside the good resolution areas in the flood maps. Another potential solution might be to adjust the measurement parameters, e.g., by employing a more conservative trigger scheme or a lower overvoltage, to likely reduce the intensity of the light accumulation points and thus avoid their overlapping at the edges of the flood maps.

The four generated CPMs allows the optimization of the crystal identification, which is based on the relative distances of the calculated 2D positions of the  $\gamma$ -photon interaction point with respect to the closest crystal labels in the corresponding CPM.

As can be observed in the figures of the last section, the distribution of scintillation events among the identified crystals is not completely homogeneous. The higher number of scintillation events in some of the identified crystals over the center of the dies is not yet completely understood. One possible explanation is that the light guide thickness was not optimized based on the number of scintillation events in all the detector areas. Therefore, there might be scintillation events occurring in the crystals above the bond wires or between the dies that are not detected. In addition, the used trigger scheme (2) might restrict the number of this kind of scintillation events. Another contributing factor might be the use of different ROIs. The "000"-ROI is the most sensitive ROI to scintillation events, as only one die must be active to accept the scintillation event as valid, and its good resolution areas include the crystals over the center of the dies. On the other hand, the "111"-ROI is more restrictive to scintillation events, as four dies must be active to accept the scintillation event as valid and its good resolution areas include the crystals above the bond wires or between the dies.

Furthermore, it is also possible to plot only the clusters that share one single identified crystal in the four selected flood maps and check whether the respective light accumulation point is distinguishable. If the expected light accumulation point is shown, the crystal identification algorithm works for most of the scintillation events generated in the selected crystal. However, this verification step is impractical due to the high number of identified crystals.

Therefore, another verification step is considered. The clusters from the scintillation events that occur in the crystals from a selected layer are plotted in the four selected flood maps. The crystal identification algorithm is able to identify most of the crystals correctly in the measured scintillation events, because the expected light accumulation points of the respective crystals from the selected layer can be distinguished visually.

Nevertheless, there might be a fraction of identified crystals that do not correspond to the scintillating crystal. Therefore, to ensure that this crystal identification algorithm works for all possible scintillation events, an additional measurement using an external reference should be performed in posterior analyses. This measurement might be necessary only once to confirm the percentage of correct identified crystals.

# Chapter 6

## Evaluation of HYPMED detector

Once the scintillating crystals can be identified in the scintillation events, the performance of the detector characterizing the scintillation events can be evaluated.

This chapter shows the analysis developed for two important parameters of the evaluation of a detector, namely the energy resolution and the coincidence time resolution, which are explained in Section 2.1.3. The first part describes this analysis and presents some of the results that are obtained in the front irradiation measurements alongside for better understanding. The second part provides an additional method and an extra measurement together with their results to expand the evaluation of the HYPMED detector.

### 6.1 Energy Resolution Evaluation

The energy of the incoming  $\gamma$ -photon can be obtained with the data provided by the dSiPM from the optical photon generated in the scintillator. A calibration between the number of optical photons and energy is possible if the energy of the incoming  $\gamma$ -photons is known. Due to the strategy followed in this thesis with four different active areas per scintillation event (the four "HVD"-ROIs), four different calibrations are carried out in parallel. The energy calibration methodology is described in Section 6.1.1.

After the energy calibration, the ability of the detector to determine the energy value of the expected  $\gamma$ -photons is evaluated. This ability is called energy resolution and is described in Section 6.1.2.

#### 6.1.1 Energy Calibration

The number of optical photons detected in the dSiPM can be correlated to the energy of the incoming  $\gamma$ -photons throughout a calibration factor. In the following, the calibration process to obtain this calibration factor is described.

The energy calibration is carried out by taking a measurement where the energy of the incoming  $\gamma$ -photons is known. The  $^{22}\text{Na}$  source used in the measurements of this thesis emits mostly 511 keV  $\gamma$ -photons and thus most of the scintillation events shall possess this energy. For each crystal, a histogram, which is called optical photon spectrum [52], is filled with the number of optical photons detected in every scintillation event. The most pronounced peak of the optical photon spectrum is assumed to be generated by the 511 keV  $\gamma$ -photons. Therefore, the calibration factor is defined as the relation between the energy of 511 keV of the  $\gamma$ -photons and the corresponding number of optical photons ( $\Sigma_{\text{photopeak position}}$ ) that produces this peak in the optical photon spectrum. As four "HVD"-ROIs are analyzed for each scintillation event, four different sums of optical photons are calculated and thus four optical photon spectra can be filled per crystal. That means, four calibration factors ( $c_{\text{HVD}}$ ) can be generated, as shown in Equation 6.1.1.

## 6.1. ENERGY RESOLUTION EVALUATION

$$c_{\text{HVD}} = \frac{511 \text{ keV}}{\sum_{\text{photopeak position}_{\text{HVD}}}}, \text{ with HVD} = \{000, 100, 010, 111\} \quad (6.1.1)$$

The sum of optical photons is only added to the respective "HVD"-ROI's optical photon spectrum if the scintillating crystal of the corresponding cluster is correctly identified. For this to happen, the identified crystal shall belong to the good resolution area of the "HVD"-ROI. Figure 6.1 shows the four optical photon spectra for one crystal that is in the good resolution area of the four ROIs in the front irradiation measurement with singles configuration.

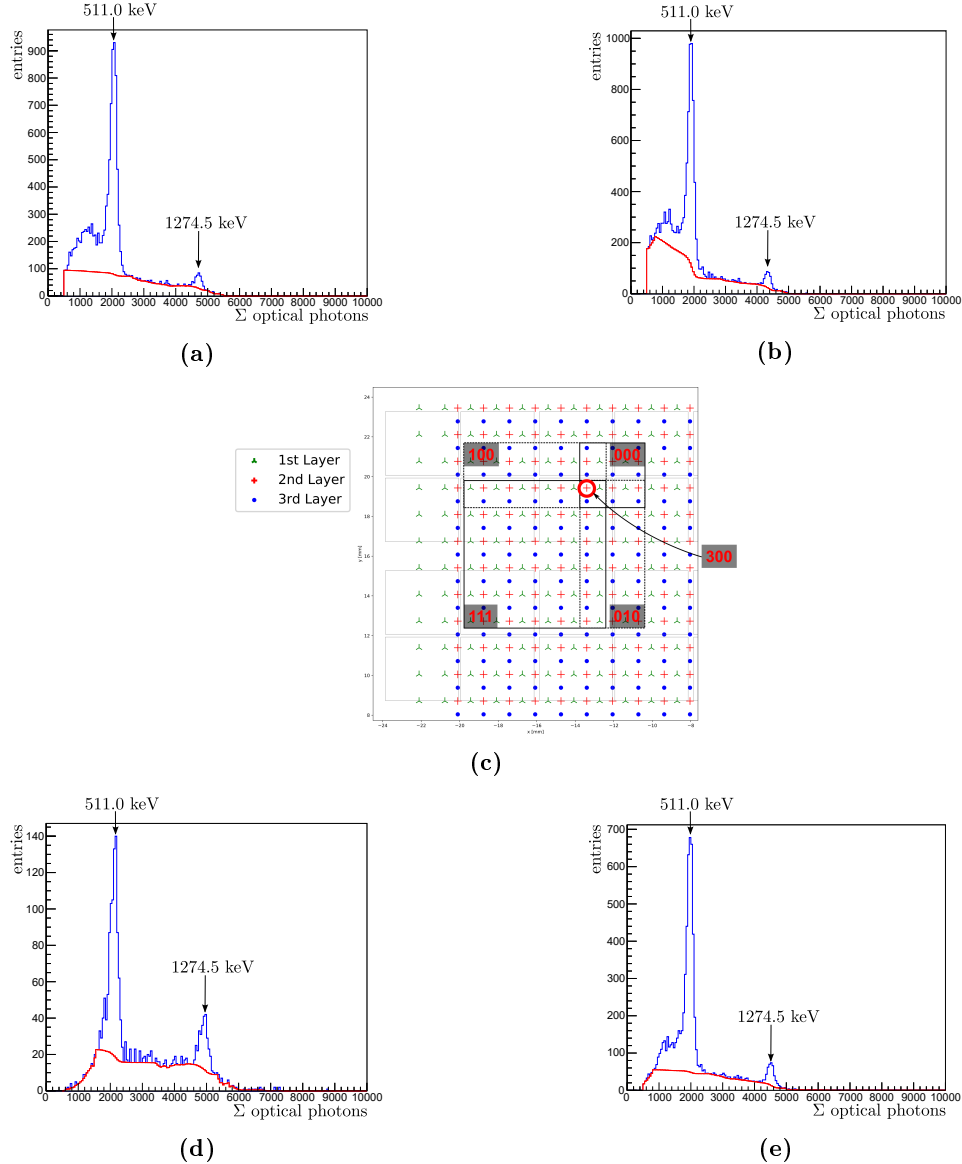


**Figure 6.1:** Optical photon spectra of crystal label "300" in the front irradiation measurement with singles configuration obtained with the four different ROIs: (a) "100"-ROI, (b) "000"-ROI, (d) "111"-ROI and (e) "010"-ROI. The background modelling is plotted in red. (c) shows the geometrical position of this crystal together with the good resolution areas of the four ROIs illustrated with black dashed and solid lines.

As explained in Section 2.1.3.1, the background of the optical photon spectrum is removed and the peak is searched following the same procedure as in Section 5.3.1. More than

## 6.1. ENERGY RESOLUTION EVALUATION

one peak can be found due to noisy events, such as inter-crystal or Compton scattering. The  $^{22}\text{Na}$  source also emits  $\gamma$ -photons with an energy of 1274.5 keV that can be detected as an extra photo peak. However, these background events can be drastically reduced if the scintillation events are filtered with the coincidence condition. Figure 6.2 shows the two available optical photon spectra for one crystal in the front irradiation measurement with coincidences configuration. The other two optical photon spectra are not available, because the crystal is not within their good resolution area and thus no sum of optical photons is added to their optical photon spectrum. Due to the coincidences configuration, the 1274.5 keV peak in the respective optical photon spectra is not visible anymore.

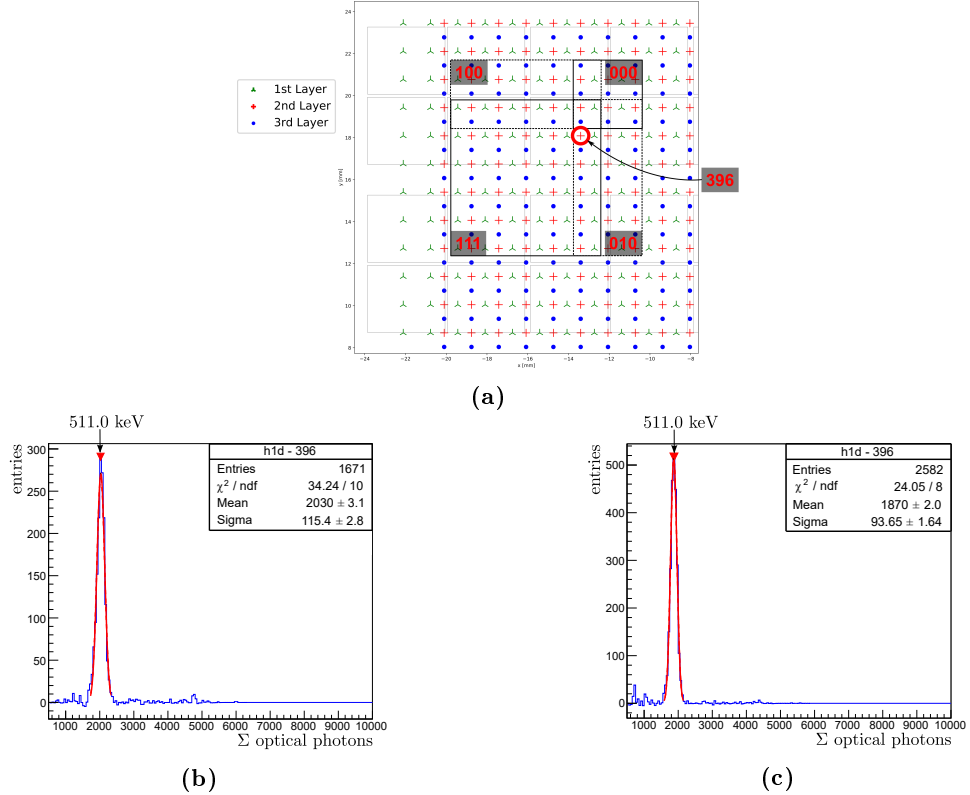


**Figure 6.2:** Optical photon spectra of crystal label "396" in the front irradiation measurement with coincidences configuration obtained with the two available ROIs: (a) "111"-ROI and (b) "010"-ROI. The Gaussian function, which is fitted to the photopeak to obtain the calibration factor, is plotted in red within the used fit range. The background is not shown. In (c), the geometrical position of this crystal is shown together with the good resolution areas of the four ROIs illustrated with black dashed and solid lines.

A Gaussian function is fitted to the found peaks to find the actual center of the peak and thus the corresponding value to calculate the calibration factor. In case multiple peaks are found, the highest peak is chosen.

Once the calculated calibration factors for all scintillation events are stored, a new iteration over the scintillation events is run to determine their energy ( $E_{\text{event}}$ ), as shown in Equation 6.1.2. In every event, more than one calibration factor may be available from different ROIs. In that case, the calibration factor of the ROI ( $c_{\text{HVD}}$ ) used to identify the crystal is selected together with the optical photon sum obtained with that ROI ( $\Sigma_{\text{event}_{\text{HVD}}}$ ).

$$E_{\text{event}} = c_{\text{HVD}} \cdot \Sigma_{\text{event}_{\text{HVD}}}, \text{ with HVD} = \{000, 100, 010, 111\} \quad (6.1.2)$$

## 6.1. ENERGY RESOLUTION EVALUATION

### 6.1.2 Energy Resolution

After the energy calibration, the energy value of every scintillation event, i.e., the energy of the incoming  $\gamma$ -photon, is reported and filled into a histogram, called energy spectrum. The expected energy of the incoming  $\gamma$ -photons is 511 keV and thus this energy value is anticipated for a large number of scintillation events. That means, the energy spectrum of a measurement with a source emitting this kind of  $\gamma$ -photons shall show a peak (photopeak) around 511 keV. The full width at half maximum (FWHM) of the photopeak provides the energy resolution of the detector, which is the ability of the detector to determine the energy value of the expected  $\gamma$ -photons. In addition, the FWHM can be affected by some of the incoming 511 keV  $\gamma$ -photons that attenuate or scatter before reaching the detector and thus their energy is slightly different.

To subtract the energy resolution, the background of the energy spectrum is not removed. The photopeak is searched following the same procedure as in Section 5.3.1. More than one peak can be found due to noisy events, such as inter-crystal or Compton scattering. The  $^{22}\text{Na}$  source also emits  $\gamma$ -photons with an energy of 1274.5 keV that can be detected as an extra peak and can be used to check the linearity of the detector' energy calibration [52]. However, the 511 keV peak is selected by choosing the highest peak. Figures 6.3a and 6.3b show the energy spectra of the two front irradiation measurements with singles and coincidences configurations, respectively. A Gaussian function is fitted to the photopeak to find its center and thus the corresponding FWHM to calculate the energy resolution.

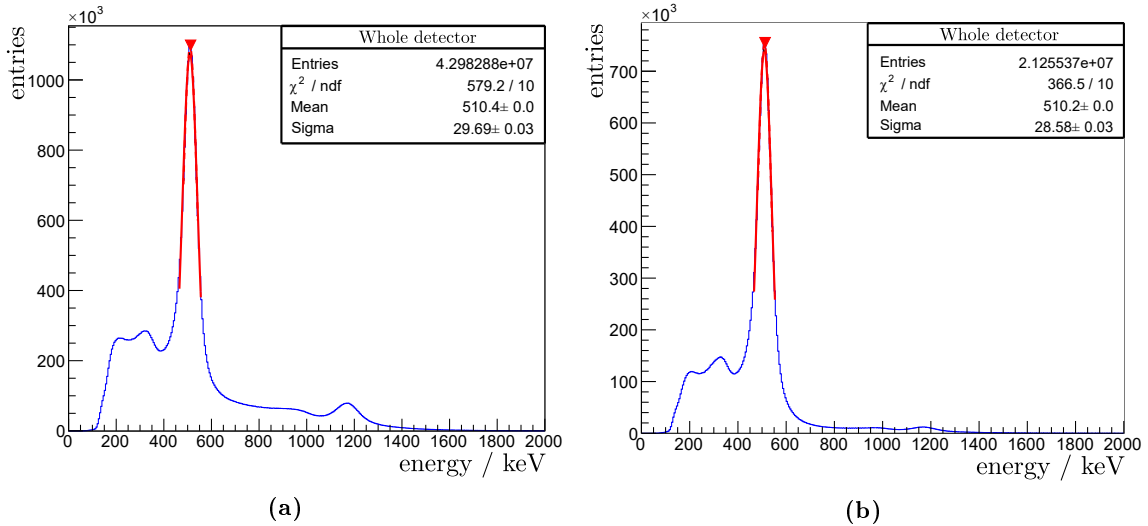


**Figure 6.3:** Energy spectra of the whole detector in the front irradiation measurement with: (a) singles configuration and (b) coincidences configuration. In both spectra, the photopeak at 511 keV is clearly visible. The Gaussian function, which is fitted to the photopeak to evaluate the energy resolution, is plotted in red within the used fit range. In (a), the peak corresponding to the  $\gamma$ -photons with an energy of 1274.5 keV from the  $^{22}\text{Na}$  source can be seen, but at a lower energy value.

The energy value of every scintillation event is not only filled into the detector's energy spectrum, but also in the energy spectra of the different layers and crystals. Hence, each of the spectra is analyzed by fitting a Gaussian function and calculating the corresponding energy resolution. While Figure 6.4 show the energy spectra for the three layers of the two front irradiation measurements with singles and coincidences configurations, in Figure 6.5

## 6.1. ENERGY RESOLUTION EVALUATION

the energy spectra for the two selected crystals in Section 6.1.1 ("300" and "396") can be found.

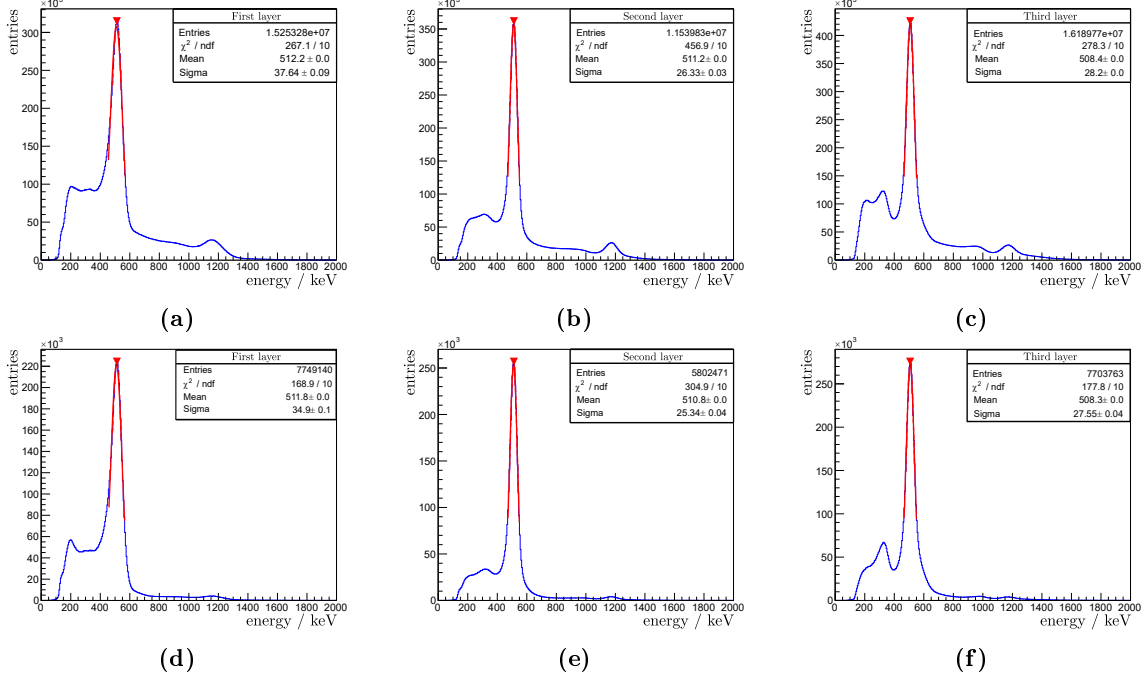


**Figure 6.4:** Energy spectra of the first, second and third layers of the detector in the front irradiation measurement with: (a), (b) and (c) obtained in singles configuration, and (d), (e) and (f) obtained in coincidences configuration. In all the spectra, the photopeak at 511 keV is clearly visible. The Gaussian function, which is fitted to the photopeak to evaluate the energy resolution, is plotted in red within the used fit range.

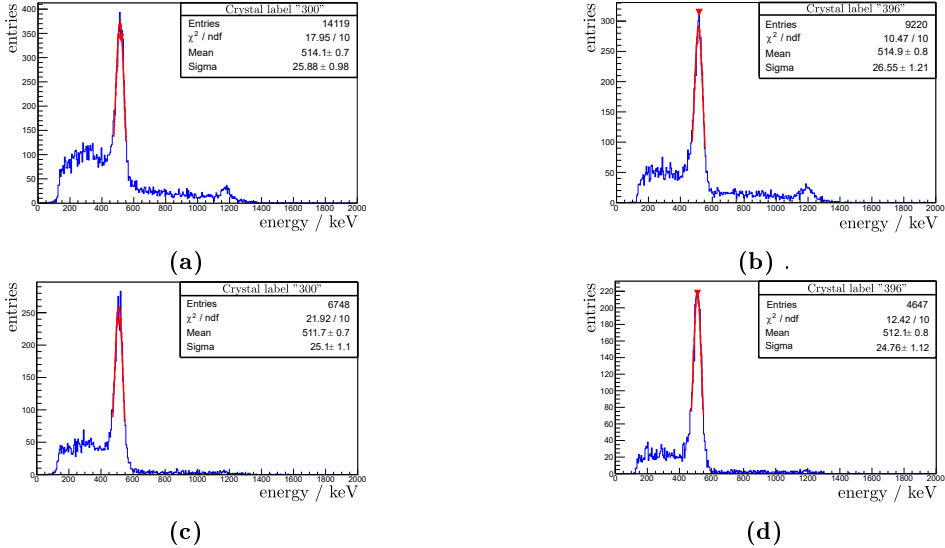


**Figure 6.5:** (a) and (c) show energy spectra of the crystal label "300" obtained in singles and coincidences configuration, respectively. (b) and (d) show energy spectra of the crystal label "396" obtained in singles and coincidences configuration, respectively. In all the spectra, the photopeak at 511 keV is clearly visible. The Gaussian function, which is fitted to the photopeak to evaluate the energy resolution, is plotted in red within the used fit range.

## 6.1. ENERGY RESOLUTION EVALUATION

### 6.1.3 Results and Discussion

Note that the first layer of the scintillator corresponds to the closest layer to the sensor tile, as shown in Figure 4.3a.

All the sums of optical photons from the scintillation events are filled into their respective photon spectra and the background is removed. Then, all the photo peaks from the different ROIs and crystals are extracted by fitting a Gaussian function. As shown in Figure 6.1, the background removal is applied correctly and both peaks from the emission of the  $^{22}\text{Na}$  source are visible. Moreover, Figure 6.1 shows that the Gaussian function is fitted successfully to the photopeak.

The position of the selected photopeak, i.e. the number of optical photons that correspond to 511 keV, might be approximately constant for crystals of the same layer in each ROI if the optical photons are equally distributed over the dies in the sensor tile. Figure 6.6 shows the position of the photopeak in every crystal of the different layers for the front irradiation measurement with coincidences configuration (see Section 5.1.2).

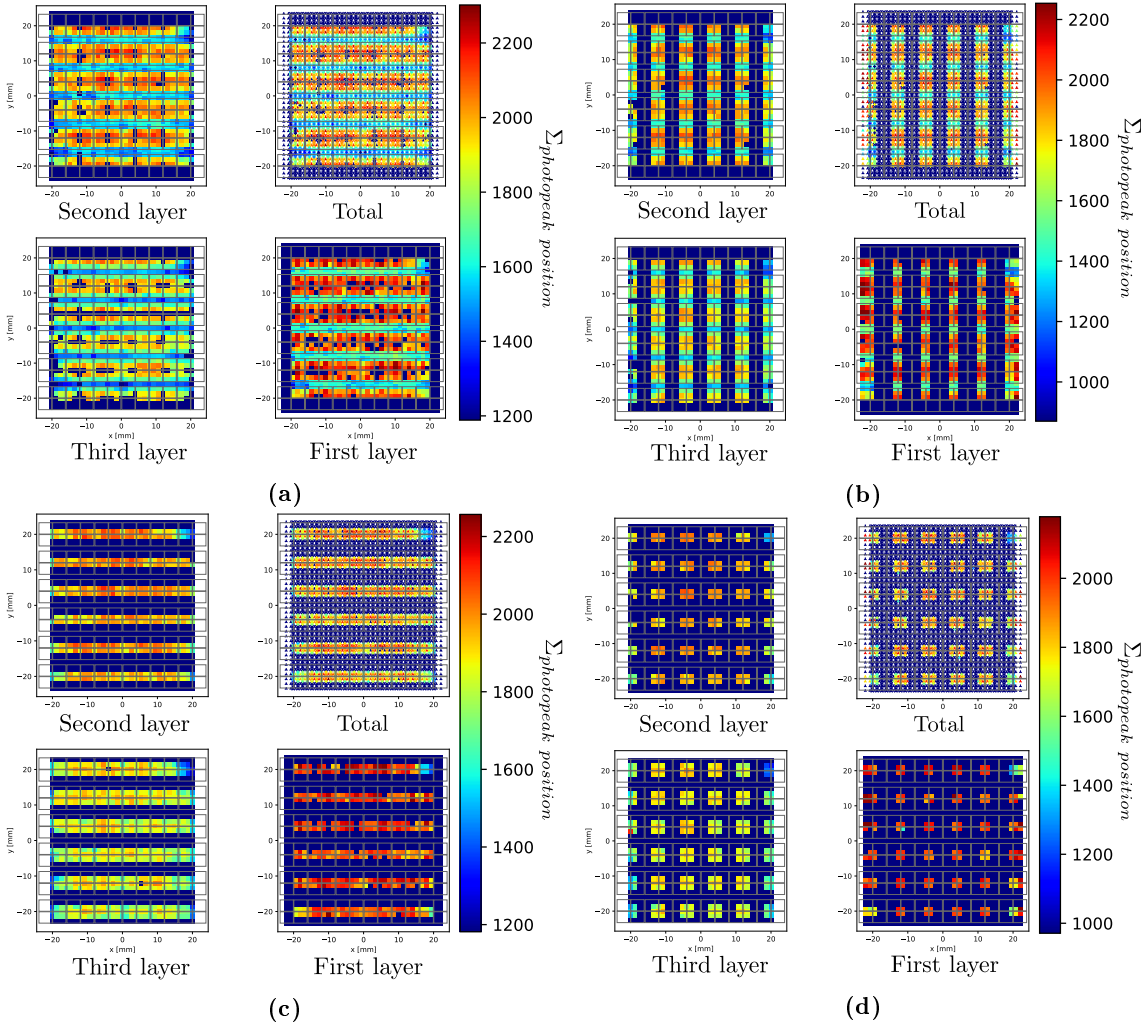


**Figure 6.6:** Sum of optical photons that correspond to the photopeak position in the crystals of the three layers of the scintillator in the front irradiation measurement with coincidences configuration for each of the four selected ROIs: (a) "111"-ROI, (b) "010"-ROI, (c) "100"-ROI and (d) "000"-ROI. The geometrical positions of the crystals in the scintillator are used to plot the values in the three layers.

An enlarged version of the individual figures in Figure 6.6 is shown in Appendix A.1.4. As observed in Figure 6.6, the photopeak positions of the identified crystals within the

## 6.1. ENERGY RESOLUTION EVALUATION

good resolution area of every ROI are returned. Photopeak positions from most of the crystals that suffer from the "ghosting" effect are also obtained.

The position of the photopeak in the different ROIs and layers show a noticeable trend that depends on the geometrical position of the crystals, especially on the crystals from the first layer, as shown in Figure 6.6. The crystals over the bond wires or between the dies tend to have a photopeak with an approximately 20% lower sum of optical photons than crystals located over the center of the dies.

With the photopeak positions, the corresponding calibration factors are calculated. At least one and up to four calibration factors are obtained for every identified crystal. Therefore, the energy of the incoming  $\gamma$ -photons that reach any of the identified crystals can be determined and filled into the energy spectra of the corresponding detector, layer and crystal as shown in Figures 6.3, 6.4 and 6.5, respectively.

While Figure 6.7 compares the energy resolution of the different layers and of the whole detector for the two front irradiation measurements with singles and coincidences configurations, Figure 6.8 shows the energy resolution obtained by each crystal individually for the two front irradiation measurements with singles and coincidences configurations.

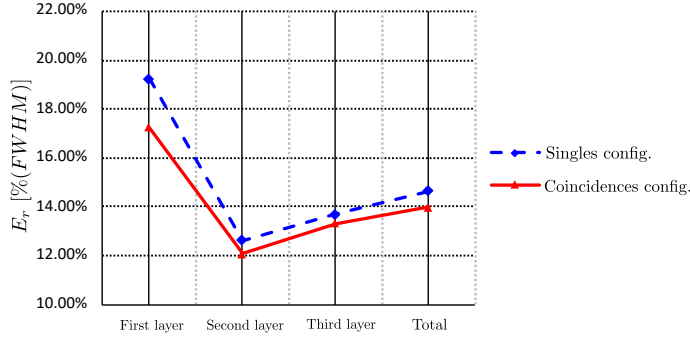


**Figure 6.7:** Energy resolution of the three layers of the scintillator and the total energy resolution of the detector stack in the front irradiation measurements with singles and coincidences configurations. Lines are drawn to guide the eye.

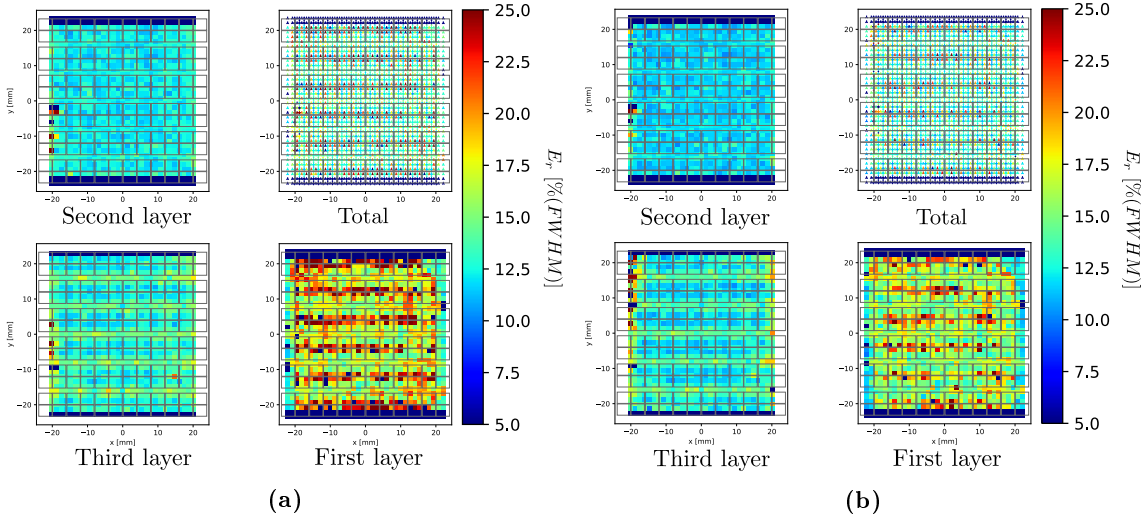


**Figure 6.8:** Energy resolution of the crystals in the three layers of the scintillator in the front irradiation measurement with: (a) singles configuration and (b) coincidences configuration. The geometrical positions of the crystals in the scintillator are used to plot the values in the three layers.

The total energy resolutions of the whole detector for the singles and coincidences

## 6.1. ENERGY RESOLUTION EVALUATION

configuration are 14.65 % and 13.98 %, respectively. The energy resolution of the first, second and third layers for the singles and coincidences configuration are 19.24 % and 17.25 %, 12.61 % and 12.07 %, and 13.70 % and 13.33 %, respectively.

The energy resolution of the second and third layers are close to each other with a relative difference of approximately 1.1 %. However, the energy resolutions of the first layer and the other two layers differ by approximately 5 % of relative difference. As can be observed in Figure 6.8, in both singles and coincidences configurations, the crystals over the central area of the sensor tiles in the first layer exhibit an energy resolution worse by about 7 % of relative difference with respect to the rest of the crystals within the layer.

Moreover, in the third layer, the crystals over the bond wires present a worse energy resolution of about 2 % relative difference with respect to the rest of the crystals within the layer.

In the first layer of the coincidences configuration, around 95 % of the crystals show an energy resolution under 20 %. In the other two layers of coincidences configuration, all the crystals present an energy resolution under 20 %, except for some at the edges.

### 6.1.4 Conclusion and Outlook

The presented routine to evaluate the energy resolution of the HYPMED detector is able to produce meaningful and consistent results. Moreover, it shows that the combination of the four complementary ROIs to assess the energy of a scintillation event is possible.

One possible explanation for the noticeable trend on the different number of optical photons that correspond to the photopeak depending on the geometrical position of the crystal is the following. If the light guide is not thick enough to spread the optical photons over the sensor tile, some of the optical photons that are generated by the crystals over the bond wires are lost and thus a lower sum of optical photons corresponds to the photopeak.

The impact of this trend on the energy resolution is discernible in the energy resolutions of especially the first and third layers. In the first layer, more scattered events due to the concentration of optical photons may be detected in the crystals over the central area of the dies and thus a worse energy resolution is produced. In contrast, in the third layer, fewer scintillation events may be detected in the crystals over the bond wires, which also results in a worse energy resolution.

Furthermore, the number of background events is reduced with the coincidences measurement. Therefore, this trend is less pronounced in the first layer of the detector for this kind of measurement and thus a better energy resolution in the first layer is obtained. As the background events also affect the other two layers, their energy resolutions are better as well. Moreover, the difference in the energy resolution between the first layer and the other two layers is reduced, but it remains large.

The presented routine evaluates all the possible scintillation events that fulfill the corresponding conditions in each ROI. Therefore, a fraction of them may be generated from scattered events that worsen the energy resolution. If this fraction can be reduced in the evaluation of the energy resolution, the detector may show a better performance. To achieve this, two main strategies can be followed: either the analysis of the scintillation events must include a filter of background events, or the measurement setup must be adjusted to avoid background events.

In Section 6.3, both strategies are followed to better understand the performance of the HYPMED detector.

## 6.2 Coincidence Resolution Time Evaluation

At least two detectors are necessary to evaluate the coincidence resolution time of a system. The timestamps of the two  $\gamma$ -photons with opposite directions are assessed with the data provided by the dSiPM from the optical photon generated in the scintillator. The timestamp from the main die (die with more optical photon counts) is selected as the arriving time of the  $\gamma$ -photon. In order to evaluate whether the detector is capable of discerning correctly the difference in time of the moment of arrival in the two active detectors, a calibration is needed. Several factors, such as electronics delays, length of cables, or if the  $\gamma$ -photon interacts with one crystal or another contribute to a possible skew in the returned timestamps from the detectors. A calibration between the time difference of the pair of  $\gamma$ -photons and the expected skew is possible, if the distance from the source to the detector is known. The CRT calibration methodology is described in Section 6.2.1.

After the CRT calibration, the ability of the detector to determine the time difference of the expected  $\gamma$ -photons is evaluated. This ability is called CRT resolution and is described in Section 6.2.2.

### 6.2.1 Time Difference Calibration

To calibrate the measured time difference of the pair of  $\gamma$ -photons and the possible time skew produced by the detector's components, the pair of coincident scintillation events is analyzed. The coincidences are reported by the control software, which is mentioned in Section 4.5, if the scintillation events detected in both detectors are within a coincidence time window of 20 ns. Then, by applying the presented crystal identification algorithm in this thesis, the scintillating crystal in both detectors is identified. In addition, the energy of both  $\gamma$ -photons is calculated. The energy, crystal label, and measured time difference is stored in a listmode file to be processed by the *hitAnalysis* program, mentioned in Section 4.5.3.

A detailed explanation of the following steps can be found in [55]. In *hitAnalysis*, a reference energy window is applied to filter the scintillation events that are not within the range of 350 keV to 650 keV for the calibration procedure. In every filtered scintillation event, the time difference is split and added to both of the crystal time difference spectra. After processing half of the scintillation events in the listmode file, the mean of the time difference histogram of each crystal, which is called the time skew, is determined by fitting a Gaussian function and stored subsequently. Next, the other half of the scintillation events is processed. However, before filling the time difference into the respective time difference spectrum, its value is corrected with the calculated time skew. After all the scintillation events are processed, a time walk model is applied before the final time difference spectrum is obtained with its corresponding CRT.

With the time walk model, the time difference of the scintillation events, whose energy ( $E_{peak}$ ) is different from the expected energy value of 511 keV ( $E_{photopeak}$ ), is corrected. The time walk model is defined in Equation 6.2.1, where  $T'$  is the corrected time difference,  $T$  is the initial time difference and  $\omega$  is the time walk factor [55].

$$T' = T - \omega \left( \frac{E_{photopeak}}{E_{event}} - 1 \right) \quad (6.2.1)$$

Figure 6.9 illustrates the linear dependency of the ratio of the photopeak energy to the measured energy of a scintillation event. As the photopeak energy of 511 keV is used as reference, the walk correction is set to zero for a measured energy equal to the photopeak energy.

## 6.2. COINCIDENCE RESOLUTION TIME EVALUATION

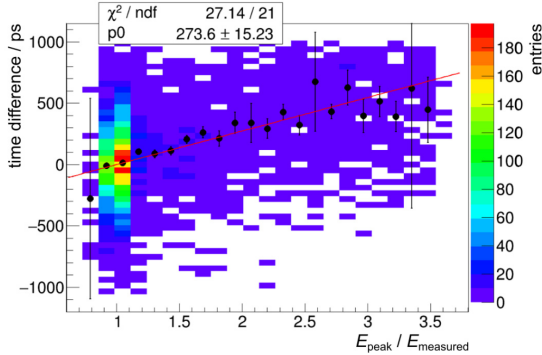


**Figure 6.9:** Example of time walk calibration for the scintillation events of a single crystal. Reprinted from [54].

A single time walk factor  $\omega$  is applied to all the scintillation events. Therefore, to obtain its optimal value, a function of the CRT of the system depending on the time walk factor is calculated. Then, the minimum of the CRT over  $\omega$  is determined and the corresponding  $\omega$  is the selected optimal value.

As the individual crystal time skews are initially unknown and many different time skews contribute to the time difference spectra (from different pairs of crystals), this analysis is run in an iterative manner ten times and the new time skews are added to the time skew value obtained in previous iterations.

### 6.2.2 Coincidence Resolution Time

With all the correction skews calculated per crystal after the ten iterations, a spectrum of the calibrated time difference in all pairs of scintillation events is generated. In this spectrum, an extra energy filter can be applied to the events. Figure 6.10 shows the time difference spectrum of the front irradiation measurement with coincidences configuration and a wide energy window of 250 keV to 625 keV.

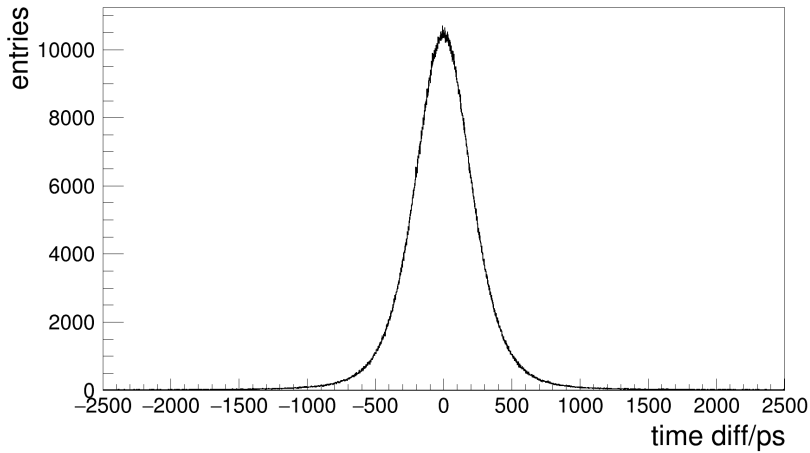


**Figure 6.10:** Time difference spectrum for the scintillation events of the front irradiation measurement in coincidences configuration.

Then, a Gaussian function is fitted in the peak of the time difference spectrum. The coincidence resolution time (CRT) of the detector is thus defined as the FWHM of the fitted peak.

## 6.3. ADDITIONAL METHOD AND MEASUREMENT

### 6.2.3 Results and Discussion

The CRT's results of the front irradiation measurement with coincidences configuration are shown in Table 6.1 for two energy windows and the trigger scheme number 2.

Experimental	Energy window [keV]	CRT [ps]
trigger scheme 2	500-520	418.6
trigger scheme 2	250-625	472.0

**Table 6.1:** CRT results for two different energy windows.

As expected, the CRT of a very narrow energy window from 500 keV to 520 keV is better than the CRT obtained with a wider energy window from 250 keV to 625 keV.

### 6.2.4 Conclusion and Outlook

The presented method to evaluate the CRT of the HYPMED detectors proves to be adequate in the light of the obtained results. The implementation of the crystal identification algorithm together with the use of the energy calculation routine to obtain the corresponding CRT of the system is a success.

Nevertheless, the CRT might be enhanced if during time calibration, crystals situated over the bond wires or between the dies are discarded as they may have larger time skews and thus possibly worse CRT [52].

## 6.3 Additional Method and Measurement

This section extends the understanding of the results obtained for the energy resolution of the detector in the different layers. The motivation is to comprehend the difference in the energy resolution of the first layer compared to the other two layers.

One of the possible factors that may explain this difference is the role of inter-crystal scattering (ICS) events as background events in this kind of detectors, especially for layers close to the photo sensor, as explained in Section 3.3.2. Therefore, Section 6.3.1 presents the use of an ICS filter to reject ICS events, which may enhance the energy resolutions of the different layers of the scintillator.

Another strategy to reduce the ICS and thus the background events is to adjust the measurement setup. If the source is placed besides the detector, the beam of  $\gamma$ -photons can be collimated to irradiate only one of the layers and thus the ICS events may be reduced. Section 6.3.2 provides the measurement setup and the results obtained with the side irradiation in the first layer.

Note that in this section, the analyses are carried out with the data obtained in coincidences configuration to ensure optimal results and reduce the possible interference of further random events.

### 6.3.1 Inter-Crystal Scattering Filter

As explained in Section 3.3.2, if a  $\gamma$ -photon suffers from inter-crystal scattering (ICS), its light distribution over the photo sensor may induce a pair of coordinates in the flood map that corresponds to a wrong scintillating crystal or may not be close to any light accumulation point and thus its respective crystal is not clearly identified. Therefore, these events contribute to the background of the flood map and their energy may not

### 6.3. ADDITIONAL METHOD AND MEASUREMENT

be correctly calculated, which may in fact affect the energy resolution of the identified crystals.

Although with the coincidences configuration the number of background events is reduced in the energy spectra of crystals, layers and detector, the fraction of ICS events can still be significant [5]. Therefore, this section explains a filtering scheme to reduce the ICS events, which may encompass other different background events.

The ICS filter is based on one idea: only the  $\gamma$ -photons whose calculated position is within an area of the flood map that clearly corresponds to an assigned crystal are accepted for the evaluation of the energy resolution. To apply this filter, the corresponding LUTs of each ROI, which are explained in Section 5.3.4, are redefined to include only these areas. Circular areas with a radius of 0.1 mm are selected around the found peak of the corresponding light accumulation point, as shown in Figure 6.11.

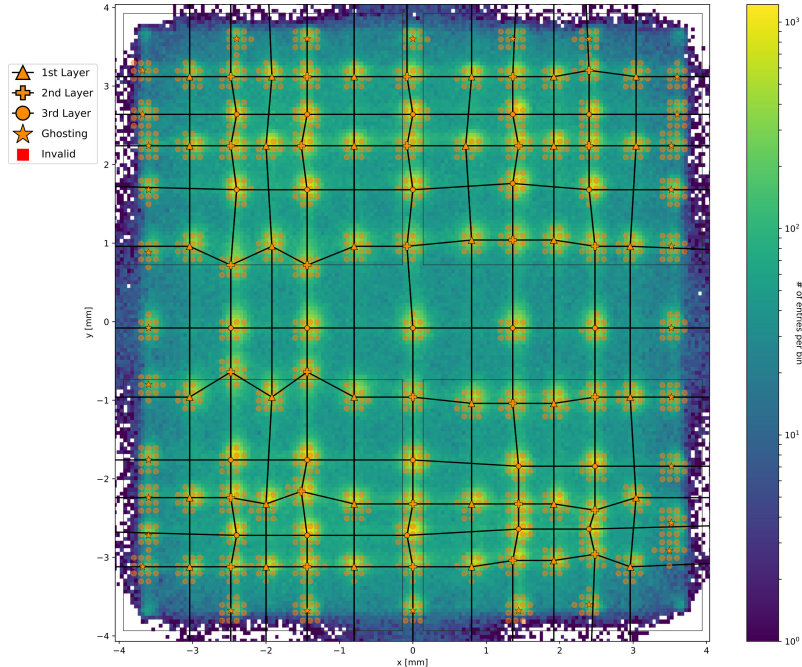


**Figure 6.11:** Flood map of an active area of the "111"-ROI with dwarfed markers for the CPM and enlarged markers for the LUT for illustrations purposes. The LUT is represented by the shadowed orange circles which cover a small radius around the valid peaks of the CPM.

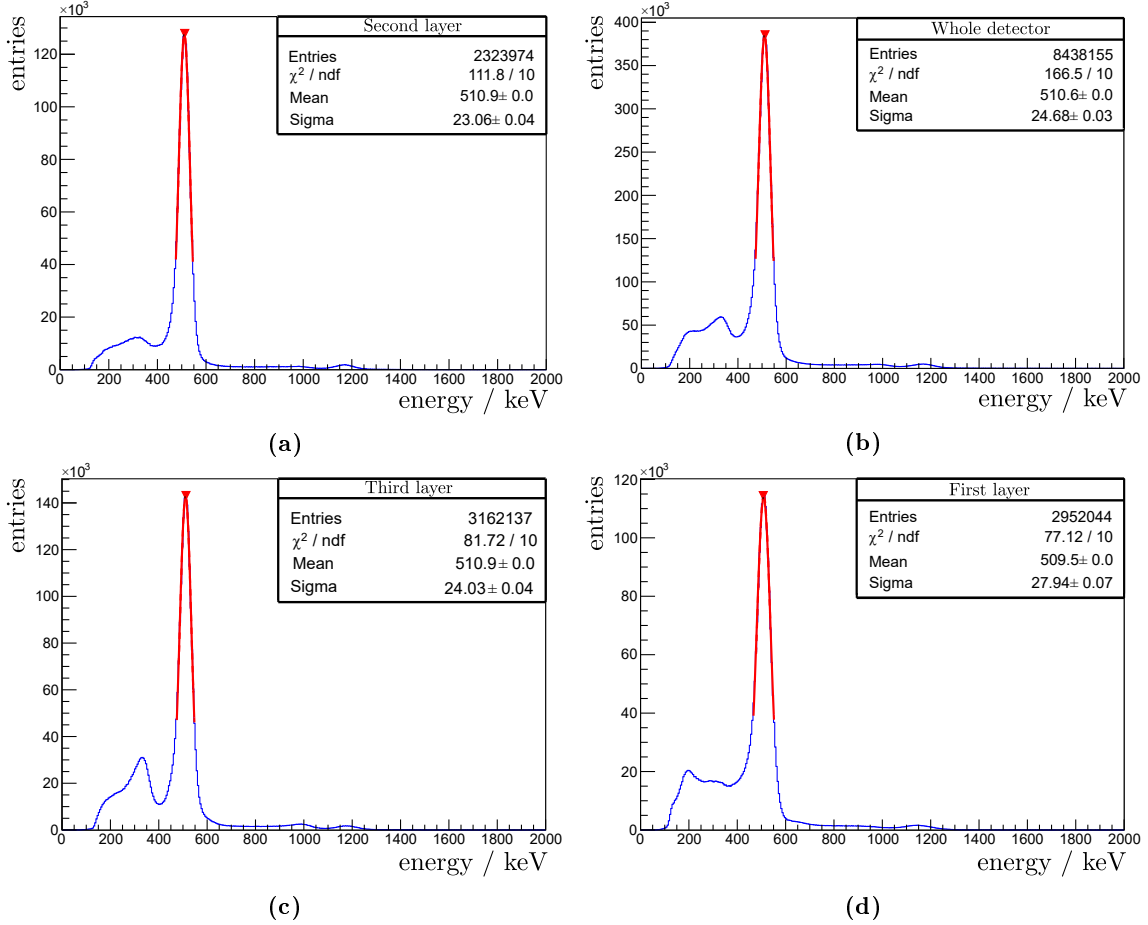
With the new LUTs, the crystal identification procedure, as explained in Section 5.3.5, is computed. Then, the energy resolution is evaluated by following the same steps that are explained in Section 6.1. In addition, the CRT is evaluated as described in Section 6.2.

#### 6.3.1.1 Results and Discussion

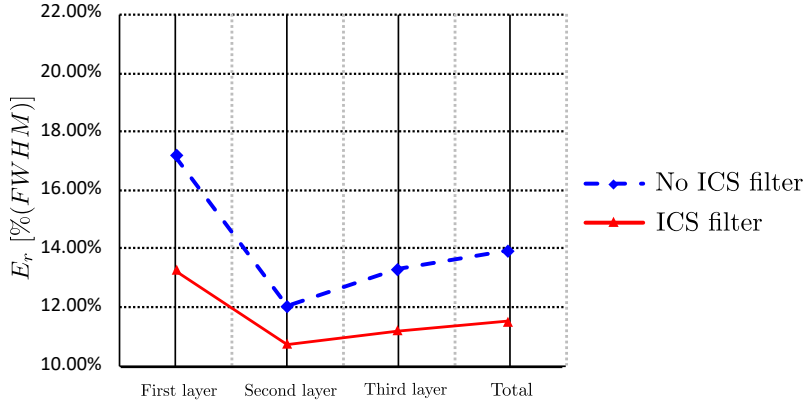
Due to the new LUT, the total number of scintillation events to be analyzed is reduced. Figure 6.12 shows the energy spectra of the whole detector and the three layers with the ICS filter activated. The number of entries is reduced by approximately 60 % compared to the number of entries reported in Figures 6.3 without the ICS filter. However, it can be seen that the number of background events is also reduced.

Figure 6.13 compares the energy resolutions obtained with the ICS filter of the different layers and of the whole detector with the energy resolutions obtained in Section 6.1.3 for the same front irradiation measurement with coincidences configurations. Furthermore, Figure 6.8 shows the energy resolution obtained by each crystal individually for the front irradiation measurement with coincidences configuration and the ICS filter.

### 6.3. ADDITIONAL METHOD AND MEASUREMENT



**Figure 6.12:** Energy spectra of the whole detector in the front irradiation measurement with: (a) singles configuration and (b) coincidences configuration. In both spectra, the photopeak at 511 keV is clearly visible. The Gaussian function, which is fitted to the photopeak to evaluate the energy resolution, is plotted in red within the used fit range.



**Figure 6.13:** Energy resolution of the three layers of the scintillator and the total energy resolution of the detector stack in the front irradiation measurements with coincidences configurations with and without ICS filter. Lines are drawn to guide the eye.

The total energy resolution of the whole detector with the ICS filter activated is 11.54 %. The corresponding energy resolutions of the first, second and third layers are 13.30 %, 10.77 %, and 11.23 %, respectively.

The energy resolution of the second and third layers are close to each other with a relative difference of approximately 0.5 %. However, the energy resolutions of the first layer

### 6.3. ADDITIONAL METHOD AND MEASUREMENT

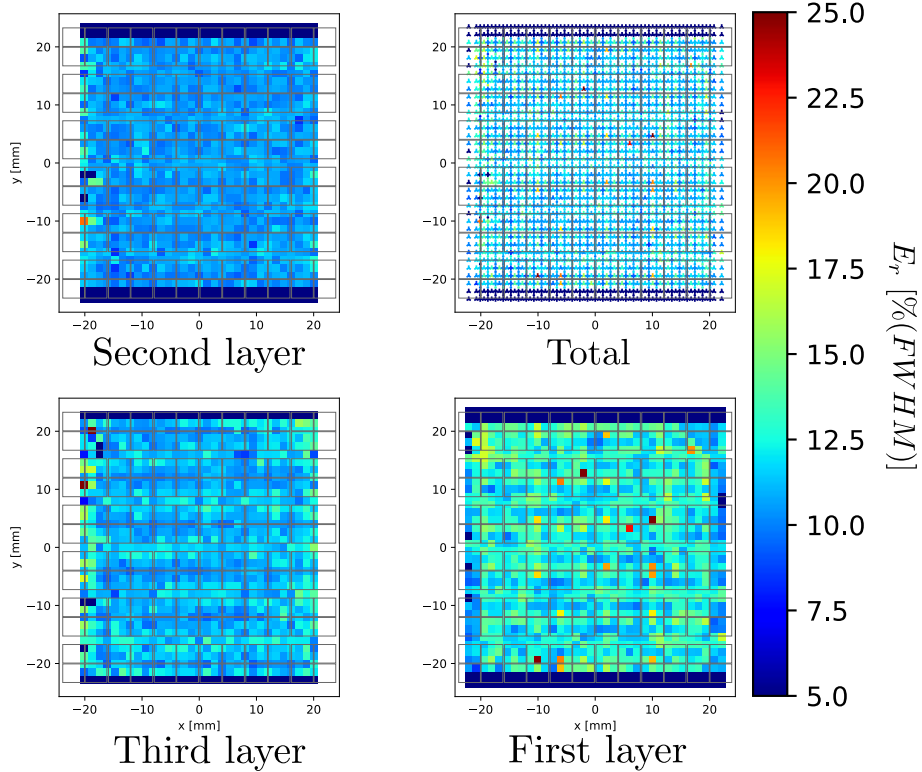


**Figure 6.14:** Energy resolution of the crystals in the three layers of the scintillator in the front irradiation measurement with coincidences configuration and ICS filter activated. The geometrical positions of the crystals in the scintillator are used to plot the values in the three layers.

and the other two layers differs by approximately 2 percent of relative difference. As observed in Figure 6.14, the crystals in the first layer present an approximately homogeneous energy resolution distribution throughout the layer compared to the reported Figures 6.8 in Section 6.1.3. However, for some of the crystals that are located over the central area of the sensor tiles, a relative difference of 5 % is encountered with respect to the rest of the crystals within the layer.

In the whole crystal array, energy resolution is under 20 %, except for some single crystals above the center of the dies in the first layer.

The CRT's results of the front irradiation measurement with coincidences configuration and the ICS filter activated are shown in Table 6.2 for two energy windows and the trigger scheme number 2.

Experimental	Energy window [keV]	CRT [ps]
trigger scheme 2	500-520	387.4
trigger scheme 2	250-625	424.9

**Table 6.2:** CRT results for two different energy windows.

A relative improvement of around 30 ps and 50 ps is found in both energy windows, 500 keV to 520 keV and 250 keV to 625 keV, respectively, compared to the results obtained without the ICS filter.

## 6.3. ADDITIONAL METHOD AND MEASUREMENT

### 6.3.1.2 Conclusion and Outlook

The presented inter crystal scattering filter or, ultimately, background events filter, is able to show that the energy resolution of the HYPMED detector can be further improved if these kinds of events are correctly accounted for.

However, the energy resolution between the first layer and the other two layers still differs, although to a lesser extent than without the ICS filter. This may therefore be an indication that among the scintillation events close to the light accumulation points there may still be background events that this method cannot distinguish.

A more complex method that studies the light pattern of each single scintillation event may be a good solution to account for such events.

### 6.3.2 Side Irradiation Measurement

Normally, the side irradiation measurements in multi-layered scintillators are employed to study the performance of the individual layers separately [27].

The aim of our side irradiation measurement is to determine whether the energy resolution of the first layer can be as good as that of the other two layers. To achieve this, the  $\gamma$ -photons must be collimated towards the first layer. Then, they can reach the first layer without first interacting with the other two layers, which may reduce the number of background events.

The results of this measurement may confirm that the characteristics of the HYPMED detector are adequate and the worsening of the energy resolution, especially in the first layer, is due to the generated background events that are not filtered.

#### 6.3.2.1 Measurement Setup

Figure 6.15 shows a sketch of the measurement setup with the location of the detector stacks and the source for a side irradiation measurement. The mounted setup can be seen in Figure 4.1.

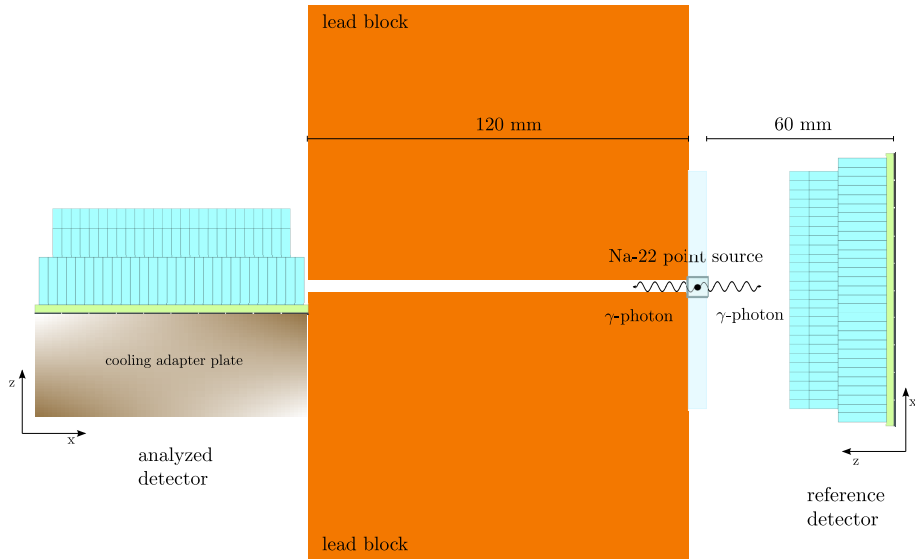


**Figure 6.15:** Sketch of the measurement setup for a side irradiation measurement.

The  $\gamma$ -photons are collimated to the side of the first layer of the scintillator using a pair of lead blocks that are placed on top of each other with a 1.5 mm slit in the center and next to the scintillator. In addition, to ensure a better light collection, the scintillators are wrapped in teflon tape.

### 6.3. ADDITIONAL METHOD AND MEASUREMENT

Table 6.3 reports the selected values for the most significant parameters in this measurement.

Parameter	Value
trigger scheme	2
validation scheme	4
overvoltage	3.0 V
source activity	1.918 MBq
distance to source	120 mm
measurement time	30 min

**Table 6.3:** Selected settings for the side irradiation measurements with coincidences configuration.

As the distance from the analyzed detector to the source is larger than in other setups (see Section 5.1), a longer measurement time is required to acquire sufficient scintillation events. In addition, it is possible that not enough  $\gamma$ -photons reach the crystals on the other side of the scintillator due to collimation and the larger distance they have to travel. Therefore, a further measurement is taken. The same setup is used, but the analyzed detector is rotated 180° in the z-axis, so that the  $\gamma$ -photons can interact with the crystals that were on the other side in the first acquisition. Then, the data from both measurements are pooled together and considered as one single data slot.

Moreover, the overvoltage is now set to 3.0 V to increase the sensitivity of the phototransistor and accept more scintillation events. Due to the longer measurement time and the more sensitive photo sensor, it might be necessary to consider intrinsic irradiation of the  $^{176}\text{Lu}$  in the LYSO crystals of the scintillator [1]. Nevertheless, to avoid these possible background events and generally reduce the number of events that are not originated by the source, the coincidences configuration is selected.

In this case, the coincidence resolution time is not analyzed and thus the reference detector is only used to discriminate the scintillation events that are not produced by the  $\gamma$ -photons from the source. At the same time, to accept the largest number of scintillation events, the projected solid angle of the reference detector towards the analyzed detector should be large enough to cover the entire sensitive area, as shown in Figure 6.16. Therefore, the distance of the reference detector to the source ( $d$ ) is shorter in comparison with the distance from the analyzed detector and the source ( $2d$ ), as shown in Figure 6.15.

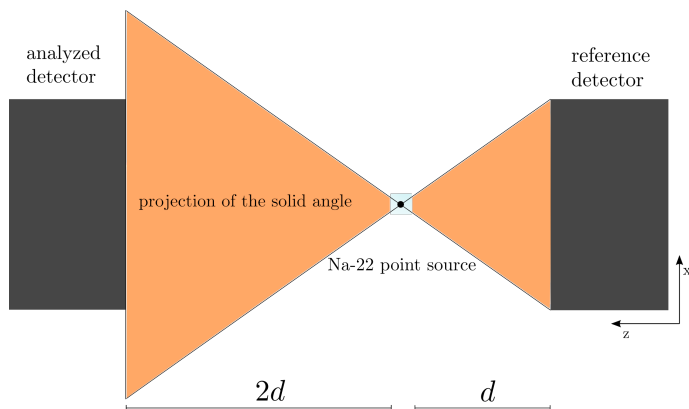


**Figure 6.16:** Sketch of the projected solid angle of the reference detector towards the analyzed detector if the distance from the source to the reference detector is shorter than to the analyzed detector. Figure follows discussions and illustrations in [5].

## 6.3. ADDITIONAL METHOD AND MEASUREMENT

### 6.3.2.2 Analysis

The scintillation events generated in the lateral irradiation measurement are analyzed taking into account that the created flood maps may show only the light accumulation points of the crystals of the first layer, as these crystals are irradiated, but the other crystals are not. The light accumulation points depend on the geometrical position of the crystals in the analyzed scintillator. Therefore, the CPMs and LUTs from previous measurements corresponding to the same detector stack can be used to identify the crystals in the scintillation events and proceed to the evaluation of the energy resolution. In this case, only the crystals in the first layers are expected to return significant results.

Note that the LUTs considered for this analysis are the ones explained in Section 5.3.4, with no ICS filter.

The crystal identification procedure is followed as explained in Section 5.3.5. Then, the energy resolution is evaluated by executing the same steps that are explained in Section 6.1. As mentioned in the previous section, the coincidence resolution time is not analyzed in this measurement.

### 6.3.2.3 Results and Discussion

Due to the irradiation of only one layer and the large distance that the  $\gamma$ -photons travel before reaching the detector, the total number of scintillation events that are analyzed is relatively low in comparison with the front irradiation measurements. However, the number of background events is also reduced, as can be observed in Figure 6.17, which shows the energy spectrum of the first layer.

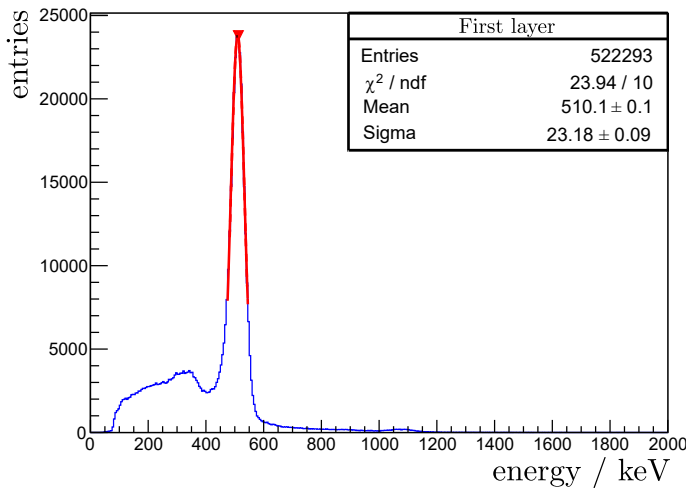


**Figure 6.17:** Energy spectra of the whole detector in the front irradiation measurement with: (a) singles configuration and (b) coincidences configuration. In both spectra, the photopeak at 511 keV is clearly visible. The Gaussian function, which is fitted to the photopeak to evaluate the energy resolution, is plotted in red within the used fit range.

The energy resolution obtained by fitting a Gaussian function to the 511 keV peak of the energy spectrum in Figure 6.17, which corresponds to the first layer of the scintillator, is 10.87%.

Figure 6.8 shows the energy resolution obtained by each crystal individually for the side irradiation measurement with coincidences configuration.

As can be observed in Figure 6.8, the only layer that presents meaningful results is the first layer. The crystals in the first layer present an homogeneous energy resolution distribution throughout the layer, except in the central region. This is expected due to the nature of the measurement. The  $\gamma$ -photons are directed to the crystals from the sides of the

### 6.3. ADDITIONAL METHOD AND MEASUREMENT

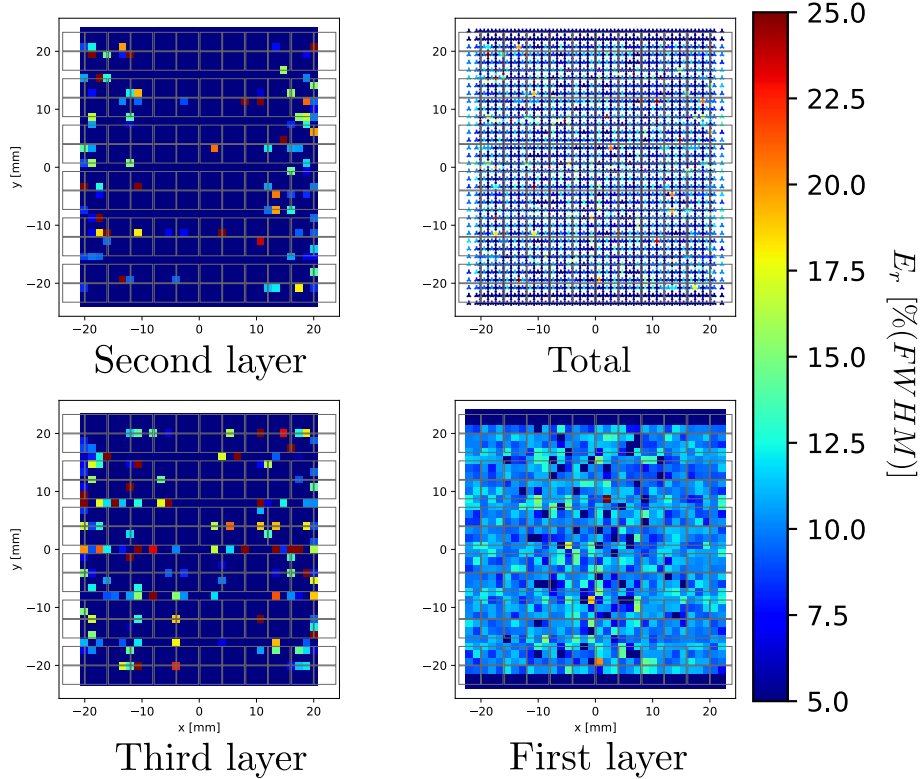


**Figure 6.18:** Energy resolution of the three layers of the scintillator and the total energy resolution of the detector stack in the side irradiation measurement with coincidences configuration.

scintillator and thus most of them may not reach the center region due to the attenuation. Therefore, in the crystals of the central region, the number of scintillation events is not sufficient to fit the 511 keV peak of their energy spectra and thus their energy resolutions are not returned.

#### 6.3.2.4 Conclusion and Outlook

The result of this measurement confirms that the characteristics of the HYPMED detector are adequate and the worsening of the energy resolution, especially in the first layer, is due to the generated background events that are not filtered.

Therefore analyses of the measured scintillation events should take into account further information related to the light pattern to quantify the background events, if improved performance is required.

# Chapter 7

# Outcome and Outlook

After the assessment of the crystal identification algorithm and the evaluation of the energy resolution and CRT of the HYPMED detector, this chapter summarizes the final results. Additionally, possible prospects on the enhancement of the crystal identification algorithm and the evaluation routine for the HYPMED detector are discussed.

## 7.1 Summary and Conclusion

In Chapter 5, the development and assessment of the crystal identification algorithm for the HYPMED detector was described in detail. Its optimization was based on four different CPM that have proven to be complementary. The step-wise procedure to generate the four CPMs yields a reliable, flexible and automatic routine, in which little prior knowledge about the detector is required and no manual correction is needed.

Nevertheless, although an undetermined fraction of identified crystals may not correspond to the scintillating crystal, the crystal identification algorithm shows a confident performance for most of the scintillation events.

Therefore, thanks to the crystal identification algorithm, quick and meaningful evaluations of the energy resolution and the CRT of the HYPMED detector can be carried out. In Chapter 6, the methods to proceed with these evaluations were explained together with their corresponding results.

The first evaluation of the energy resolution in the HYPMED detector yielded a large relative difference between the first layer with respect to the other two layers of the scintillator.

The presented inter-crystal scattering filter or, ultimately, background events filter, is able to show that the energy resolution of the HYPMED detector can be further improved if these kinds of events are correctly accounted for. With this filter, the derived relative difference in energy resolution between the first layer with respect to the other two layers was reduced.

An additional measurement to irradiate only the first layer from the side was carried out to avoid the inter-crystal scattering effect provoked by the other two layers in the front irradiation measurement. With this measurement, the energy resolution in the first layer is comparable to that of the other two layers.

The best energy resolution of 11.54 % for the whole array of crystal in the HYPMED detector is obtained with the front irradiation measurement in the coincidences configuration and an applied filter to reduce the number of background events. For the individual layers, the best energy resolutions were computed with two different setups. In the case of the second and third layer respectively, energy resolutions down to 10.77 % and 11.23 % were reached with the front irradiation measurement in the coincidences configuration and an applied filter to reduce the number of background events. For the first layer, an en-

## 7.2. OUTLOOK

ergy resolution down to 10.87% is obtained with the side irradiation measurement in the coincidences configuration.

The implementation of the crystal identification algorithm together with the use of the energy calculation routine to evaluate the corresponding CRT of the system proved to be adequate in the light of the obtained results.

The best CRT value of 387.4 ps is reached in the system with the front irradiation measurement in the coincidences configuration and an applied filter to reduce the number of background events.

It has been shown that all the layers of the studied scintillator can provide a relative similar energy resolution, either by means of the software (data filters) or by means of the setup, irradiating one single layer. Moreover, the obtained top results in energy resolution and CRT are substantially better than the results reported by similar PET detectors, seen in Table 3.1. Therefore, the studied PET detector has proven to be an auspicious candidate for the HYPMED project.

## 7.2 Outlook

To ensure that the presented crystal identification algorithm works for all possible scintillation events, an additional measurement using an external reference should be performed in posterior analyses. This measurement might be necessary only once to confirm the percentage of correctly identified crystals in the total number of scintillation events.

If the necessary setup to carry out precise measurements with an external reference is built, machine learning or neural network methods may be convenient to simplify the crystal identification process.

Moreover, the crystal identification algorithm can be further enhanced to handle the unassigned crystals in the three upper and lower rows, which are currently not distinguishable in any of the four selected flood maps.

To maintain the top performance parameters results without loss of sensitivity, analyses of the measured scintillation events could take into account further information related to the light pattern to quantify and analyze the background events [31].

Further side irradiation measurements collimating the  $\gamma$ -photons towards the second and third layers individually may prove that their current energy resolution values are indeed top results.

The energy calibration factors from the side measurements could be employed in the front irradiation measurements to check whether the energy resolutions are then enhanced.

Furthermore, the CRT might be improved if during time calibration, crystals situated over the bond wires or between the dies are discarded as they may have larger time skews and thus possibly worse CRT [52].

Finally, a statistic analysis of the performance parameters' values among more detector stacks may be convenient to assess the final system performance.

# Bibliography

- [1] H. Alva-Sánchez et al. “Understanding the intrinsic radioactivity energy spectrum from  $^{176}\text{Lu}$  in LYSO/LSO scintillation crystals”. In: 8.1 (2018), pp. 1–7. ISSN: 20452322. DOI: [10.1038/s41598-018-35684-x](https://doi.org/10.1038/s41598-018-35684-x).
- [2] Hal O. Anger. “Scintillation camera”. In: 29.1 (1958), pp. 27–33. ISSN: 00346748. DOI: [10.1063/1.1715998](https://doi.org/10.1063/1.1715998).
- [3] Dale L Bailey, Joel S Karp, and Suleman Surti. “Physics and Instrumentation in PET”. In: *Positron Emission Tomography: Basic Sciences*. Ed. by Dale L Bailey et al. Springer London, 2005, pp. 13–39. ISBN: 978-1-84628-007-8. DOI: [10.1007/1-84628-007-9\\_2](https://doi.org/10.1007/1-84628-007-9_2). URL: [https://doi.org/10.1007/1-84628-007-9\\_2](https://doi.org/10.1007/1-84628-007-9_2).
- [4] M.J. Berger et al. *XCOM: Photon Cross Sections Database / NIST*. Tech. rep. NIST, PML, Radiation Physics Division, 2010. DOI: <https://dx.doi.org/10.18434/T48G6X>. URL: <https://www.nist.gov/pml/xcom-photon-cross-sections-database>.
- [5] Tim Binder et al. “Performance evaluation of a staggered 3-layer DOI PET detector using a 1 mm LYSO pitch with PETsys TOFPET2 ASIC: Comparison of HAMA-MATSU and KETEK SiPMs”. In: (2021).
- [6] Maria Giuseppina Bisogni, Alberto Del Guerra, and Nicola Belcaro. *Medical applications of silicon photomultipliers*. May 2019. DOI: [10.1016/j.nima.2018.10.175](https://doi.org/10.1016/j.nima.2018.10.175).
- [7] Rene Brun and Fons Rademakers. *ROOT - An Object Oriented Data Analysis Framework*. Apr. 1997. DOI: [10.1016/S0168-9002\(97\)00048-X](https://doi.org/10.1016/S0168-9002(97)00048-X).
- [8] P Bruyndonckx et al. “Performance Study of a PET Detector Module Based on a Continuous Scintillator”. In: 53.5 (Oct. 2006), pp. 2536–2542. ISSN: 0018-9499. DOI: [10.1109/TNS.2006.882799](https://doi.org/10.1109/TNS.2006.882799).
- [9] Niccolò Camarlinghi et al. “Evaluation of Algorithms for Photon Depth of Interaction Estimation for the TRIMAGE PET Component”. In: 63.1 (2016), pp. 70–74. ISSN: 00189499. DOI: [10.1109/TNS.2015.2512986](https://doi.org/10.1109/TNS.2015.2512986).
- [10] Tingting Chang et al. “Reliability of predicting image signal-to-noise ratio using noise equivalent count rate in PET imaging”. In: 39.10 (2012), pp. 5891–5900. ISSN: 00942405. DOI: [10.1118/1.4750053](https://doi.org/10.1118/1.4750053).
- [11] Simon R. Cherry and Magnus Dahlbom. “PET: Physics, Instrumentation, and Scanners”. In: *Pet*. Ed. by Michael E Phelps. Springer New York, 2006, pp. 1–117. ISBN: 978-0-387-34946-6. DOI: [10.1007/0-387-34946-4\\_1](https://doi.org/10.1007/0-387-34946-4_1). URL: [https://doi.org/10.1007/0-387-34946-4\\_1](https://doi.org/10.1007/0-387-34946-4_1).
- [12] G. I. Coats and A. S. Goldin. “Energy alignment of gamma spectrometers.” In: 81.11 (1966), pp. 999–1007. ISSN: 00946214. DOI: [10.2307/4592894](https://doi.org/10.2307/4592894).
- [13] P Conde et al. “Determination of the Interaction Position of Gamma Photons in Monolithic Scintillators Using Neural Network Fitting”. In: 63.1 (Feb. 2016), pp. 30–36. ISSN: 0018-9499. DOI: [10.1109/TNS.2016.2515163](https://doi.org/10.1109/TNS.2016.2515163).

## BIBLIOGRAPHY

- [14] B. M. Coursey et al. “Standardization of  $^{18}\text{F}$  for use in positron emission tomography”. In: 34.8 (1983), pp. 1181–1189. DOI: [https://doi.org/10.1016/0020-708X\(83\)90186-2](https://doi.org/10.1016/0020-708X(83)90186-2). URL: <https://www.sciencedirect.com/science/article/pii/0020708X83901862>.
- [15] Federica Demattè. “Characterization of High Resolution DOI-Capable PET Detectors with Digital SiPM Readout for a Dedicated Breast PET / MRI System”. Master thesis. 2019.
- [16] *Digital Hybrid Breast PET/MRI for Enhanced Diagnosis of Breast Cancer / HYPMED Project / H2020 / CORDIS / European Commission*. URL: <https://cordis.europa.eu/project/id/667211/> (visited on 06/10/2021).
- [17] Peter M. Düppenbecker et al. “Development of an MRI-compatible digital SiPM detector stack for simultaneous PET/MRI”. In: 2.1 (2016), p. 15010. ISSN: 20571976. DOI: 10.1088/2057-1976/2/1/015010. URL: <http://dx.doi.org/10.1088/2057-1976/2/1/015010>.
- [18] E. Fermi. “Versuch einer Theorie der  $\beta$ -Strahlen. I”. In: 88.3-4 (Mar. 1934), pp. 161–177. ISSN: 14346001. DOI: 10.1007/BF01351864. URL: <https://link.springer.com/article/10.1007/BF01351864>.
- [19] S Gambhir et al. “A Tabulated Summary of the FDG PET Literature”. In: 42(S1) (2001), 1S–93S. URL: [http://jnm.snmjournals.org/content/42/5\\_suppl/1S.short](http://jnm.snmjournals.org/content/42/5_suppl/1S.short).
- [20] Benjamin Goldschmidt et al. “Software-based real-time acquisition and processing of PET detector raw data”. In: 63.2 (2016), pp. 316–327. ISSN: 15582531. DOI: 10.1109/TBME.2015.2456640.
- [21] Jan Grahe et al. “Optical Monte-Carlo Simulation to Evaluate Monolithic PET Detector Concepts”. In: (2018). DOI: 10.1109/NSSMIC.2017.8532632.
- [22] Nicolas Gross-Weege et al. “Maximum likelihood positioning algorithm for high-resolution PET scanners”. In: 43.6 (2016), pp. 3049–3061. ISSN: 00942405. DOI: 10.1118/1.4950719.
- [23] Z. Gu et al. “A DOI detector with crystal scatter identification capability for high sensitivity and high spatial resolution PET imaging”. In: 62.3 (2015), pp. 740–747. ISSN: 00189499. DOI: 10.1109/TNS.2015.2408333.
- [24] Samantha J. Holdsworth and Roland Bammer. “Magnetic Resonance Imaging Techniques: fMRI, DWI, and PWI”. In: 28.04 (2008), pp. 395–406. DOI: 10.1055/s-0028-1083697.
- [25] “HYPMED EU Project To Develop Hybrid PET / MRI”. In: (2016).
- [26] Mikiko Ito et al. “Four-layer DOI detector with a relative offset in animal PET system”. In: *2007 IEEE Nuclear Science Symposium Conference Record*. IEEE, 2007, pp. 4296–4299. ISBN: 978-1-4244-0922-8. DOI: 10.1109/NSSMIC.2007.4437066. URL: <http://ieeexplore.ieee.org/document/4437066/>.
- [27] Mikiko Ito et al. “A four-layer DOI detector with a relative offset for use in an animal PET system”. In: 57.3 PART 1 (2010), pp. 976–981. ISSN: 00189499. DOI: 10.1109/TNS.2010.2044892.
- [28] Judith E. Kalinyak et al. “Breast cancer detection using high-resolution breast PET compared to whole-body PET or PET/CT”. In: 41.2 (2014), pp. 260–275. ISSN: 16197089. DOI: 10.1007/s00259-013-2553-1.

## BIBLIOGRAPHY

- [29] Han Gyu Kang, Fumihiro Nishikido, and Taiga Yamaya. “A staggered 3-layer DOI PET detector using BaSO<sub>4</sub> reflector for enhanced crystal identification and inter-crystal scattering event discrimination capability”. In: 7.3 (May 2021), p. 035018. ISSN: 20571976. DOI: 10.1088/2057-1976/abf6a8. URL: [https://iopscience.iop.org/article/10.1088/2057-1976/abf6a8/meta](https://iopscience.iop.org/article/10.1088/2057-1976/abf6a8%20https://iopscience.iop.org/article/10.1088/2057-1976/abf6a8/meta).
- [30] Zhonghua Kuang et al. “Development of depth encoding small animal PET detectors using dual-ended readout of pixelated scintillator arrays with SiPMs”. In: 45.2 (Feb. 2018), pp. 613–621. ISSN: 2473-4209. DOI: 10.1002/MP.12722. URL: <https://aapm.onlinelibrary.wiley.com/doi/full/10.1002/mp.12722%20https://aapm.onlinelibrary.wiley.com/doi/abs/10.1002/mp.12722%20https://aapm.onlinelibrary.wiley.com/doi/10.1002/mp.12722>.
- [31] Fung Chih Lam et al. “An Inter-crystal Scatter Correction Method for DOI PET Image Reconstruction”. In: 26.3 (2006), pp. 118–130.
- [32] Craig S Levin and Edward J Hoffman. “Calculation of positron range and its effect on the fundamental limit of positron emission tomography system spatial resolution”. In: 44.3 (1999), p. 781. URL: <http://stacks.iop.org/0031-9155/44/i=3/a=019>.
- [33] Mohan Li and Shiva Abbaszadeh. “Depth-of-interaction study of a dual-readout detector based on TOFPET2 application-specific integrated circuit HHS Public Access”. In: 64.17 (2019), p. 175008. DOI: 10.1088/1361-6560/ab3866.
- [34] Yanye Lu et al. “Development of a SiPM-based PET imaging system for small animals”. In: 743 (Apr. 2014), pp. 30–38. ISSN: 0168-9002. DOI: 10.1016/J.NIMA.2014.01.010.
- [35] M C Maas et al. “Experimental characterization of novel small animal PET detector modules based on scintillation crystal blocks read out by APD arrays”. In: *IEEE Symposium Conference Record Nuclear Science 2004*. Vol. 5. Oct. 2004, pp. 2942–2946. DOI: 10.1109/NSSMIC.2004.1466303.
- [36] Michelle D. McDonough, Elizabeth R. DePeri, and Betty A. Mincey. “The role of positron emission tomographic imaging in breast cancer”. In: 6.1 (2004), pp. 62–68. ISSN: 15233790. DOI: 10.1007/s11912-996-0011-y.
- [37] R. S. Miyaoka et al. “Performance characteristics for a low cost dual sided position sensitive sparse sensor (DS-PS3) PET detector with depth of interaction positioning”. In: *Proc. IEEE Nucl. Sci. Symp. Med. Imag. Conf. (NSS/MIC)*. 2017.
- [38] I. Mohammadi et al. “Minimization of parallax error in positron emission tomography using depth of interaction capable detectors: Methods and apparatus”. In: 5.6 (2019). ISSN: 20571976. DOI: 10.1088/2057-1976/ab4a1b.
- [39] William W Moses. “Fundamental limits of spatial resolution in PET”. In: 648.SUPPL. 1 (2011). ISSN: 01689002. DOI: 10.1016/j.nima.2010.11.092.
- [40] Florian Muller et al. “Gradient Tree Boosting-Based Positioning Method for Monolithic Scintillator Crystals in Positron Emission Tomography”. In: 2.5 (2018), pp. 411–421. ISSN: 2469-7311. DOI: 10.1109/TRPMS.2018.2837738.
- [41] Patrick Hallen Volkmar Schulz Nicolas Gross-Weege David Schug. “Maximum likelihood positioning algorithm for high[U+2010]resolution PET scanners”. In: 43 (2016), pp. 2691–3227. DOI: <https://doi.org/10.1118/1.4950719>.
- [42] D.G. Nishimura. *Principles of Magnetic Resonance Imaging*. Stanford University, 2010.
- [43] “PDPC Tile-TEK User Manual Version 1.02”. 2016.

## BIBLIOGRAPHY

- [44] L. Pidol et al. “High Efficiency of Lutetium Silicate Scintillators, Ce-Doped LPS and LYSO Crystals for Medical Applications”. In: 555. September (2007), pp. 371–376. ISSN: 1662-9752. DOI: 10.4028/www.scientific.net/msf.555.371.
- [45] *Processing and Visualization Functions*. URL: <https://root.cern.ch/root/html/doc/guides/spectrum/Spectrum.html#peak-searching> (visited on 07/09/2021).
- [46] *Product Website*. 2021. URL: <http://www.tianlephotronics.com/>.
- [47] Akshat C. Pujara et al. “PET/MRI in Breast Cancer”. In: 49.2 (2019), pp. 328–342. ISSN: 15222586. DOI: 10.1002/jmri.26298.
- [48] *ROOT: TSpectrum2 Class Reference*. URL: <https://root.cern/doc/master/classTSpectrum2.html#a6a346c29d38ca4afc72fa9c551d3cef3> (visited on 07/09/2021).
- [49] Gopal B. Saha. *Basics of PET Imaging: Physics, Chemistry, and Regulations*. Springer Science and Business Media, 2010, pp. 1–241. ISBN: 9781441908049. DOI: 10.1007/978-1-4419-0805-6.
- [50] Dennis R Schaart et al. “Advances in digital SiPMs and their application in biomedical imaging”. In: 809 (2016), pp. 31–52. ISSN: 0168-9002.
- [51] Ruth E Schmitz, Adam M Alessio, and Paul E Kinahan. “1 The Physics of PET/CT Scanners”. In: (2019), pp. 1–16. DOI: 10.1055/b-0039-166611.
- [52] D Schug. “About the Calibration and PET Performance of a preclinical PET/MRI insert equipped with digital Silicon Photomultipliers”. PhD Thesis.
- [53] D Schug et al. “First evaluations of the neighbor logic of the digital SiPM tile”. In: *2012 IEEE Nuclear Science Symposium and Medical Imaging Conference Record (NSS/MIC)*. Oct. 2012, pp. 2817–2819. DOI: 10.1109/NSSMIC.2012.6551642.
- [54] D Schug et al. “Data Processing for a High Resolution Preclinical PET Detector Based on Philips DPC Digital SiPMs”. In: 62.3 (2015), pp. 669–678. ISSN: 0018-9499. DOI: 10.1109/TNS.2015.2420578.
- [55] David Schug et al. “Crystal Delay and Time Walk Correction Methods for Coincidence Resolving Time Improvements of a Digital-Silicon-Photomultiplier-Based PET/MRI Insert”. In: 1.2 (Mar. 2017), pp. 178–190. ISSN: 2469-7311. DOI: 10.1109/TNS.2017.2654920. URL: <https://ieeexplore.ieee.org/document/7835275/>.
- [56] V Schulz et al. “Improving the Diagnosis of Breast Cancer using a dedicated PET/MRI – The EU Project HYPMED”. In: *58. Jahrestagung der Deutschen Gesellschaft für Nuklearmedizin*. Vol. 59. 02. © Georg Thieme Verlag KG, Apr. 2020, P43. DOI: 10.1055/s-0040-1708301. URL: <http://www.thieme-connect.com/products/ejournals/html/10.1055/s-0040-1708301>.
- [57] V Schulz et al. “A dedicated PET insert for a 1.5T MR system for simultaneous breast PET/MRI”. In: *59. Jahrestagung der Deutschen Gesellschaft für Nuklearmedizin*. Vol. 60. 02. Georg Thieme Verlag KG, Apr. 2021, p. L17. DOI: 10.1055/s-0041-1726709. URL: <http://www.thieme-connect.com/products/ejournals/html/10.1055/s-0041-1726709>.
- [58] *SCIONIX RTV 481 Datasheet*. Tech. rep. SCIONIX HOLLAND BV, 2020.
- [59] J. Anthony Seibert and John M. Boone. “X-Ray Imaging Physics for Nuclear Medicine Technologists. Part 2: X-Ray Interactions and Image Formation”. In: 33.1 (2005), pp. 3–18. ISSN: 00914916.
- [60] Steven H. Simon. “Solid State Basics”. In: 53.9 (2013), pp. 1689–1699. ISSN: 1098-6596. eprint: [arXiv:1011.1669v3](https://arxiv.org/abs/1011.1669v3).
- [61] Antonio Soriano et al. “Minimization of parallax error in dedicated breast PET”. In: 60.2 (2013), pp. 739–745. ISSN: 00189499. DOI: 10.1109/TNS.2012.2226749.

## BIBLIOGRAPHY

- [62] Giancarlo Sportelli et al. “The TRIMAGE PET Data Acquisition System: Initial Results”. In: 1.2 (2016), pp. 168–177. ISSN: 2469-7311. DOI: 10.1109/tns.2016.2633237.
- [63] Justin Stiles et al. “Evaluation of High-Sensitivity Organ-Specific Positron Emission Tomography (PET) System”. In: *2019 IEEE Nuclear Science Symposium and Medical Imaging Conference (NSS/MIC)*. IEEE, Oct. 2019, pp. 1–3. ISBN: 978-1-7281-4164-0. DOI: 10.1109/NSS/MIC42101.2019.9059644. URL: <https://ieeexplore.ieee.org/document/9059644/>.
- [64] *The HDF5® Library File Format - The HDF Group*. 2021. URL: <https://www.hdfgroup.org/solutions/hdf5> (visited on 07/05/2021).
- [65] Jocelyn E C Towson and Stefan Eberl. “Radiation Protection and Dosimetry in PET and PET/CT”. In: *Positron Emission Tomography: Clinical Practice*. Ed. by Peter E Valk et al. Springer London, 2006, pp. 41–62. ISBN: 978-1-84628-187-7. DOI: 10.1007/1-84628-187-3\_4. URL: [https://doi.org/10.1007/1-84628-187-3\\_4](https://doi.org/10.1007/1-84628-187-3_4).
- [66] Jane M. Ussher, Janette Perz, and Emilee Gilbert. “Changes to sexual well-being and intimacy after breast cancer”. In: 35.6 (Nov. 2012), pp. 456–465. ISSN: 0162220X. DOI: 10.1097/NCC.0b013e3182395401. URL: <https://pubmed.ncbi.nlm.nih.gov/22222680/>.
- [67] I G Valais et al. “Luminescence Emission Properties of(Lu, Y)<sub>2</sub>SiO<sub>5</sub>:Ce (LYSO:Ce) and(Lu, Y)AlO<sub>3</sub>:Ce (LuYAP:Ce) Single Crystal Scintillators Under Medical Imaging Conditions”. In: 55.2 (2008), pp. 785–789. ISSN: 0018-9499. DOI: 10.1109/TNS.2008.918737.
- [68] Carel W.E. Van Eijk. “Inorganic scintillators in medical imaging detectors”. In: 509.1-3 (2003), pp. 17–25. ISSN: 01689002. DOI: 10.1016/S0168-9002(03)01542-0.
- [69] Stefaan Vandenberghe, Pawel Moskal, and Joel S. Karp. “State of the art in total body PET”. In: 7.1 (2020). ISSN: 21977364. DOI: 10.1186/s40658-020-00290-2.
- [70] Don Vernekohl. “Small Animal Positron Emission Tomography with Gas Detectors Simulations, Prototyping, and Quantitative Image Reconstruction”. In: April (2014), p. 194. URL: [https://www.uni-muenster.de/imperia/md/content/physik\\_kp/agwessels/thesis\\_db/ag\\_wessels/vernekohl\\_2014\\_dissertation.pdf](https://www.uni-muenster.de/imperia/md/content/physik_kp/agwessels/thesis_db/ag_wessels/vernekohl_2014_dissertation.pdf).
- [71] S van der Walt, S C Colbert, and G Varoquaux. “The NumPy Array: A Structure for Efficient Numerical Computation”. In: 13.2 (2011), pp. 22–30. ISSN: 1521-9615. DOI: 10.1109/MCSE.2011.37.
- [72] Qingyang Wei et al. “A neighborhood standard deviation based algorithm for generating PET crystal position maps”. In: c (2013), pp. 9–12. ISSN: 10957863. DOI: 10.1109/NSSMIC.2013.6829273.
- [73] Qingyang Wei et al. “Crystal Identification in Dual-Layer-Offset DOI-PET Detectors Using Stratified Peak Tracking Based on SVD and Mean-Shift Algorithm”. In: 63.5 (2016), pp. 2502–2508. ISSN: 00189499. DOI: 10.1109/TNS.2016.2590505.
- [74] Qingyang Wei et al. “Crystal identification for a dual-layer-offset LYSO based PET system via Lu-176 background radiation”. In: *2017 IEEE Nuclear Science Symposium and Medical Imaging Conference (NSS/MIC)*. IEEE, Oct. 2017, pp. 1–3. ISBN: 978-1-5386-2282-7. DOI: 10.1109/NSSMIC.2017.8533093. URL: <https://ieeexplore.ieee.org/document/8533093/>.
- [75] B Weißler. “Digital PET/MRI for Preclinical Applications”. PhD Thesis.
- [76] B et al. Weißler. “A Digital Preclinical PET/MRI Insert and Initial Results”. In: 34.11 (2015), pp. 2258–2270. DOI: 10.1109/TMI.2015.2427993. URL: <http://ieeexplore.ieee.org/stamp/stamp.jsp?tp=&arnumber=7097723&isnumber=7310891>.

## BIBLIOGRAPHY

- [77] B Weissler et al. “Hyperion III – A flexible PET detector platform for simultaneous PET/MRI”. In: *58. Jahrestagung der Deutschen Gesellschaft für Nuklearmedizin*. Vol. 59. 02. © Georg Thieme Verlag KG, Apr. 2020, p. V93. DOI: 10.1055/s-0040-1708245. URL: <http://www.thieme-connect.com/products/ejournals/html/10.1055/s-0040-1708245%20http://www.thieme-connect.de/DOI/DOI?10.1055/s-0040-1708245>.
- [78] Fred L. Wilson. “Fermi’s Theory of Beta Decay”. In: 36.12 (Dec. 1968), pp. 1150–1160. ISSN: 0002-9505. DOI: 10.1119/1.1974382.
- [79] W. A. Worthoff, Yun S. D., and N. J. Shah. *Introduction to Magnetic Resonance Imaging*. 2018. ISBN: 9781788013062.
- [80] Eiji Yoshida et al. “Calibration procedure for a DOI detector of high resolution PET through a gaussian mixture model”. In: 51.5 II (2004), pp. 2543–2549. ISSN: 00189499. DOI: 10.1109/TNS.2004.835746.
- [81] Habib Zaidi and Alberto Del Guerra. “An outlook on future design of hybrid PET/MRI systems”. In: 38.10 (2011), pp. 5667–5689. ISSN: 00942405. DOI: 10.1118/1.3633909.
- [82] Claudia Christina Zanella. “Methods to Enhance Nuclear Magnetic Resonance Sensitivity at High Magnetic Field”. PhD Thesis. 2021.

# Appendix A

## Appendix

### A.1 Enlarged Figures

In this section enlarged version of already shown figures can be observed.

#### A.1.1 Flood Maps

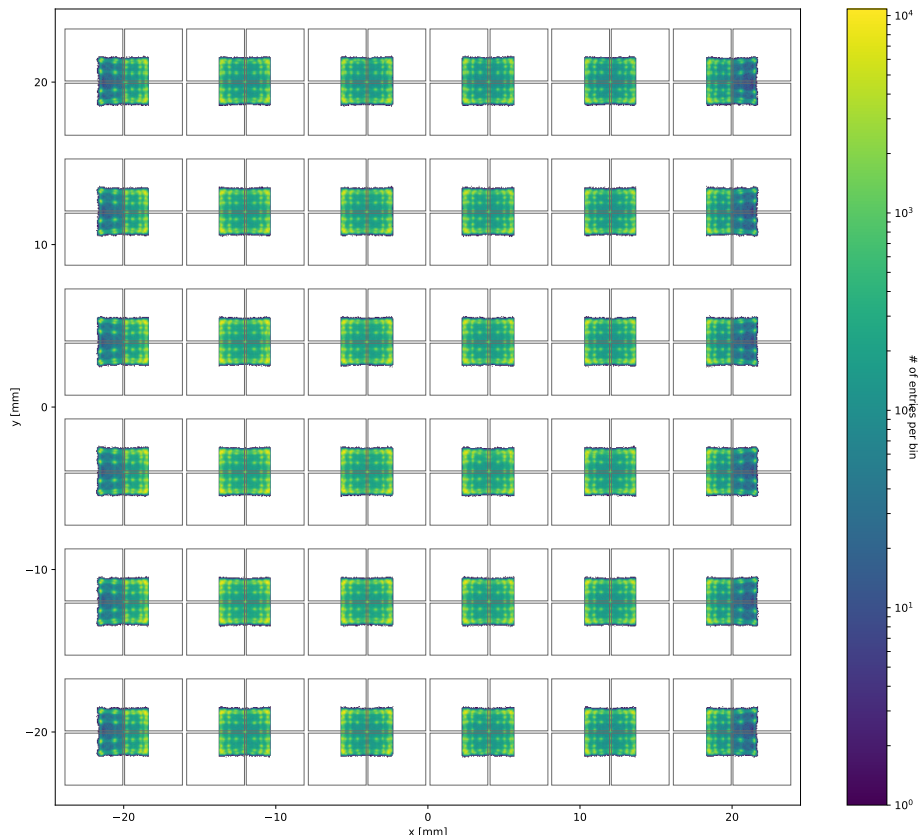


**Figure A.1:** Generated flood map of the "000"-ROI.

## A.1. ENLARGED FIGURES

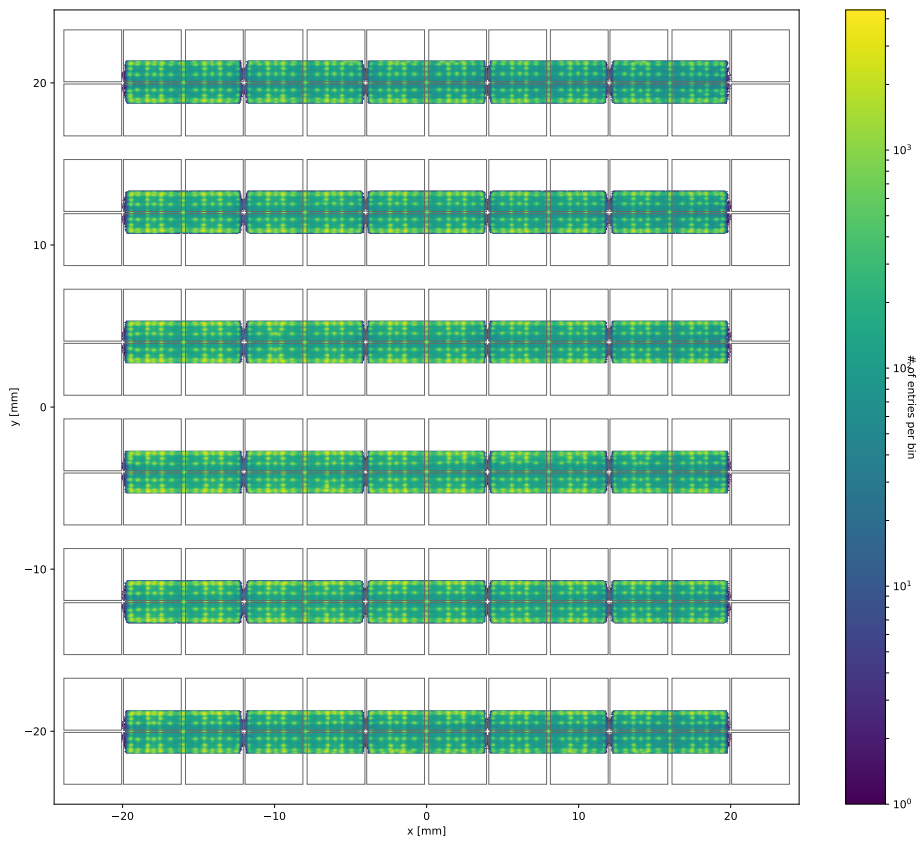


**Figure A.2:** Generated flood map of the "100"-ROI.

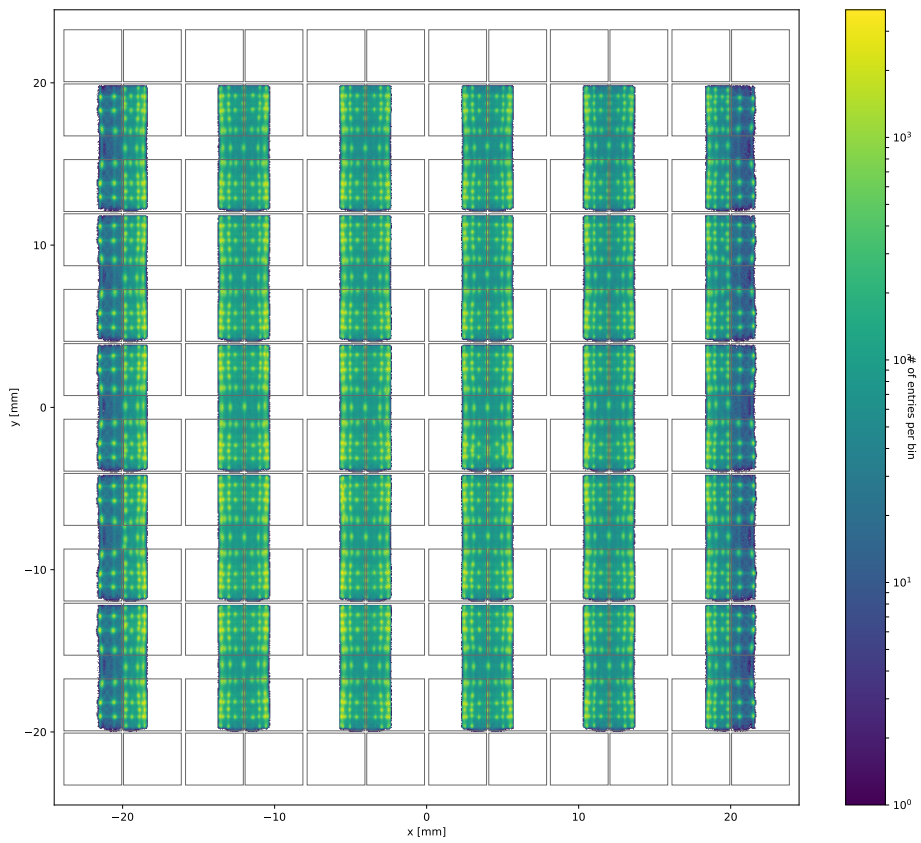


**Figure A.3:** Generated flood map of the "010"-ROI.

## A.1. ENLARGED FIGURES

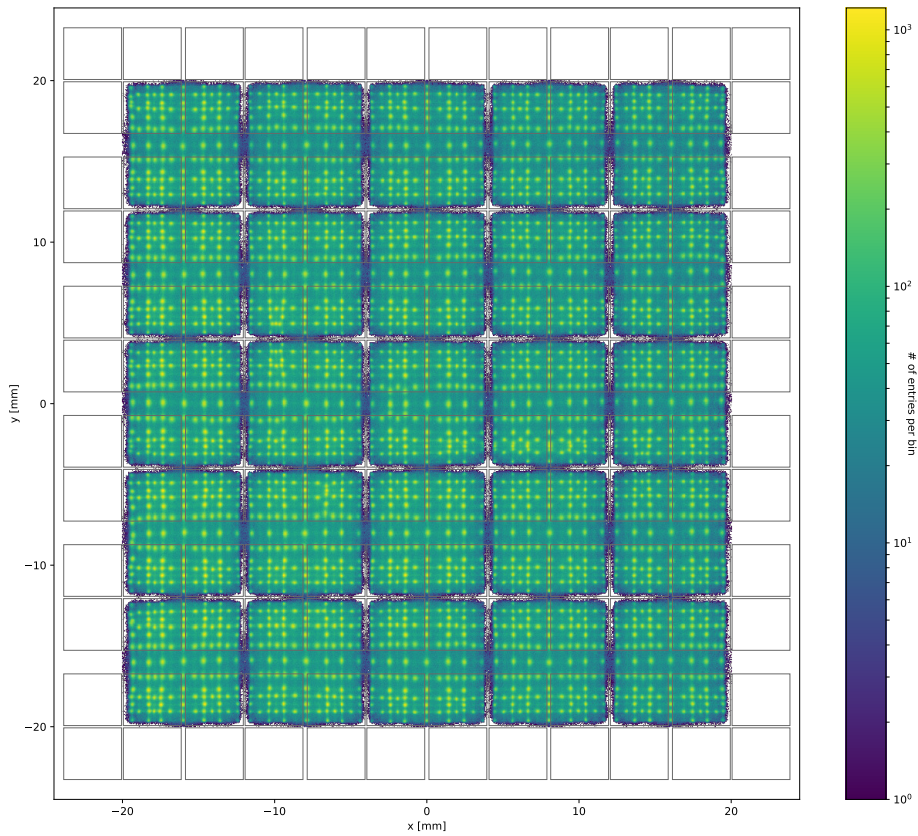


**Figure A.4:** Generated flood map of the "111"-ROI.

### A.1.2 CPMs

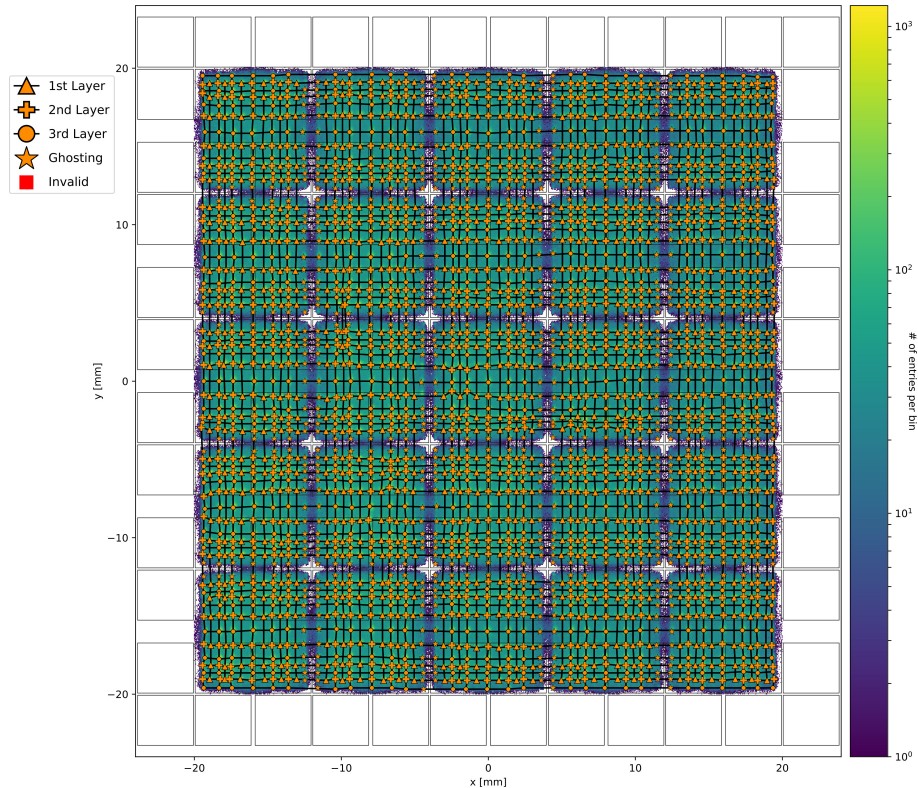


**Figure A.5:** Generated CPM of the "111"-ROI.

## A.1. ENLARGED FIGURES

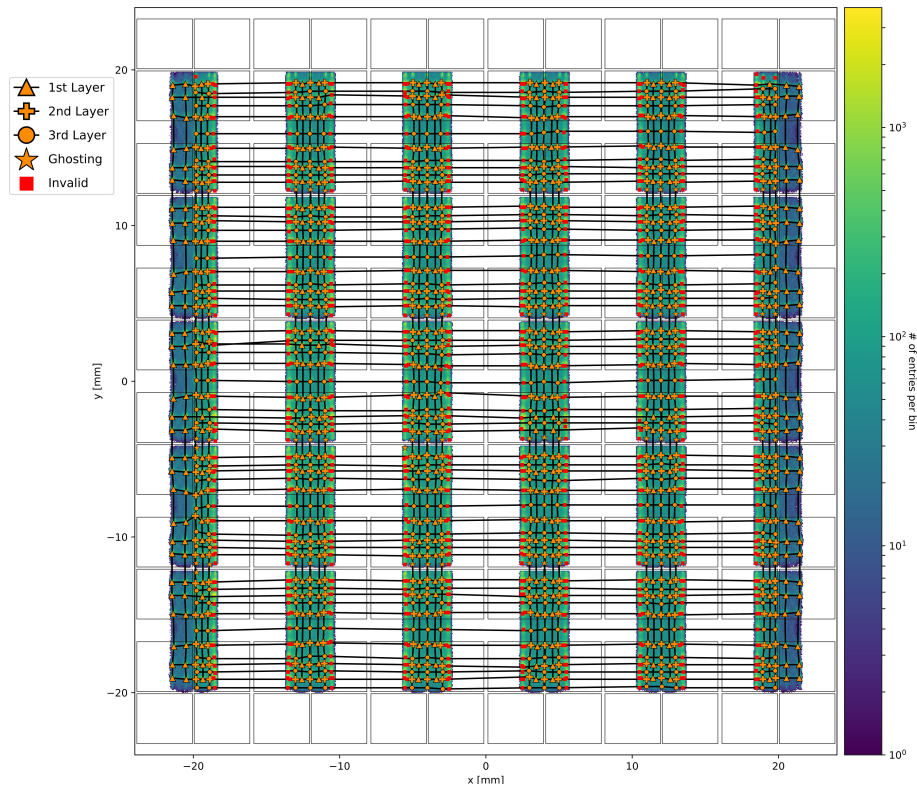


**Figure A.6:** Generated CPM of the "111"-ROI.

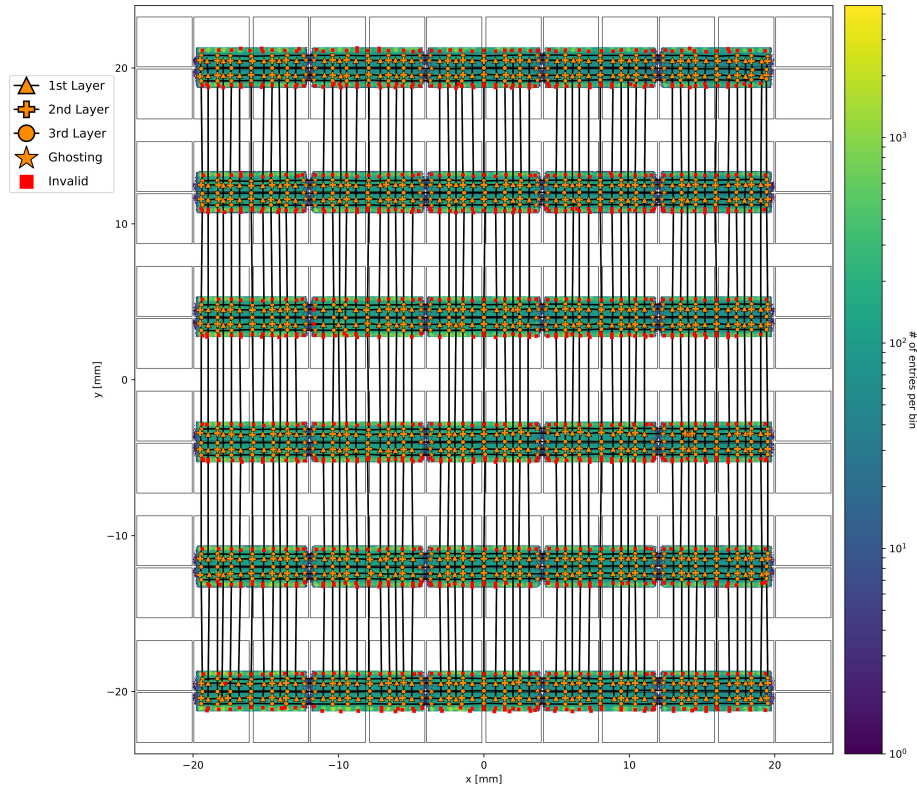


**Figure A.7:** Generated CPM of the "111"-ROI.

## A.1. ENLARGED FIGURES

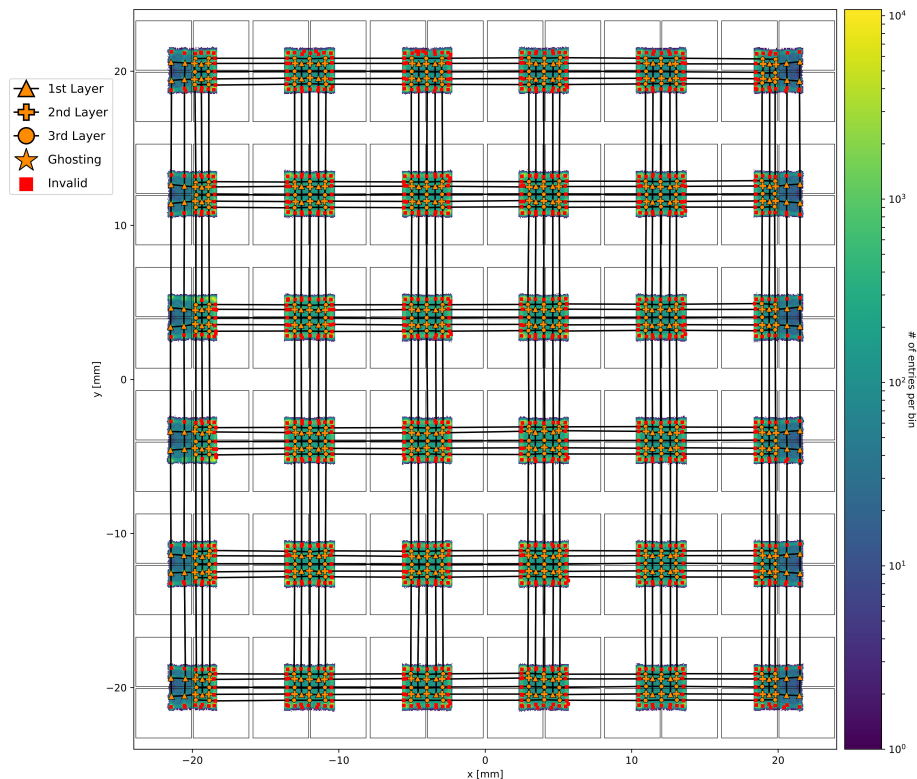


**Figure A.8:** Generated CPM of the "111"-ROI.

### A.1.3 Flood map with layered filtered scintillation events

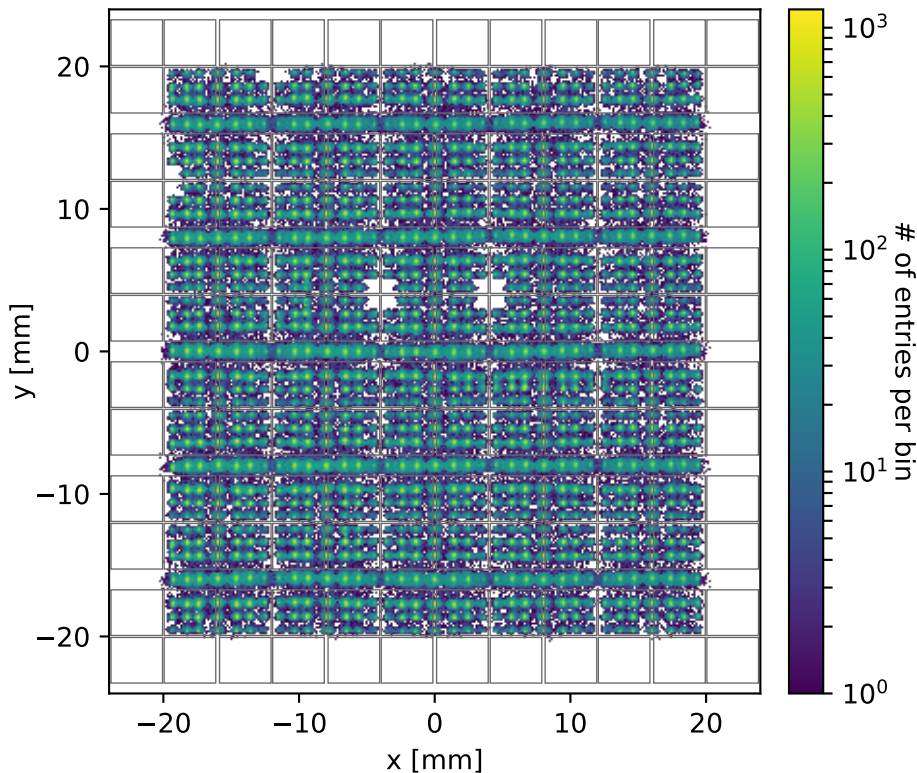


**Figure A.9:** Flood map originated from the "111"-ROI with calculated clusters of scintillation events whose identified crystal labels belong to the third layer.

## A.1. ENLARGED FIGURES

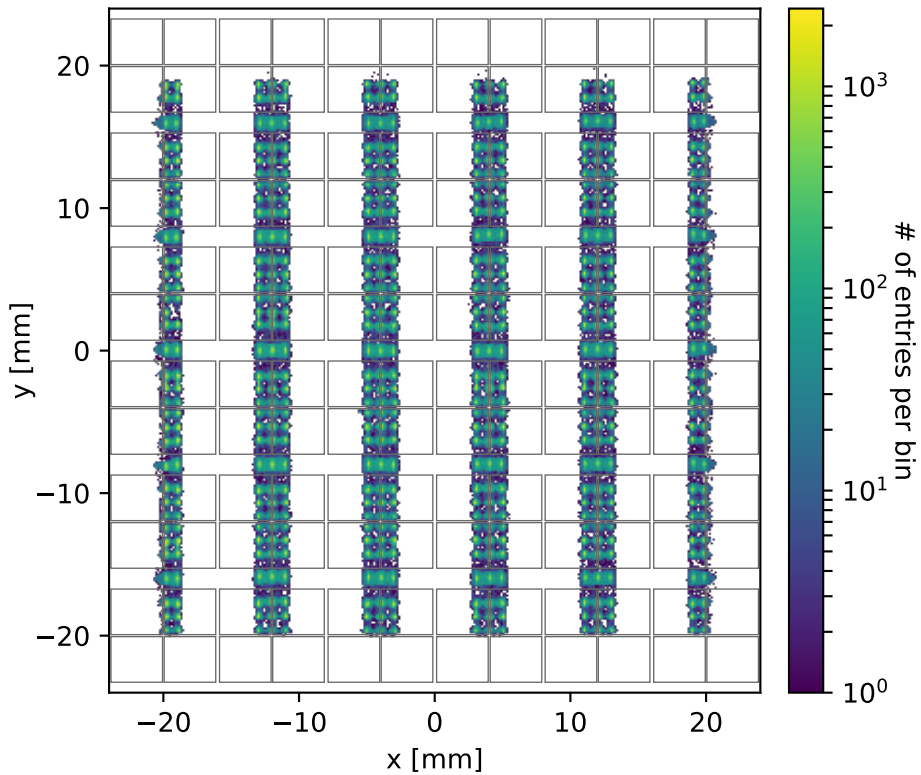


**Figure A.10:** Flood map originated from the "010"-ROI with calculated clusters of scintillation events whose identified crystal labels belong to the third layer.

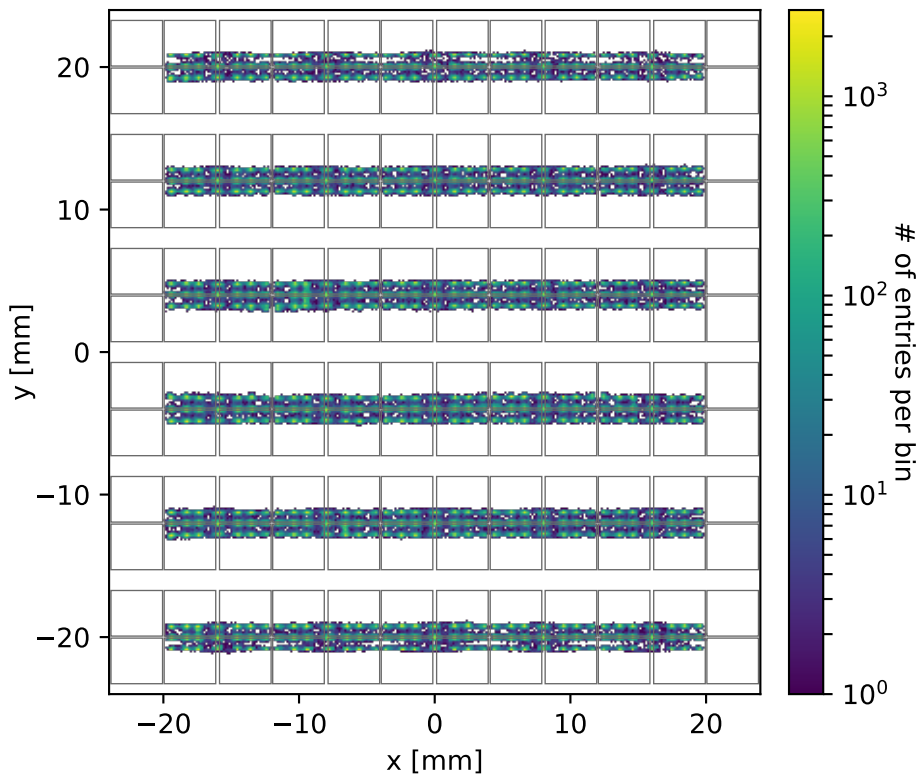


**Figure A.11:** Flood map originated from the "100"-ROI with calculated clusters of scintillation events whose identified crystal labels belong to the third layer.

## A.1. ENLARGED FIGURES

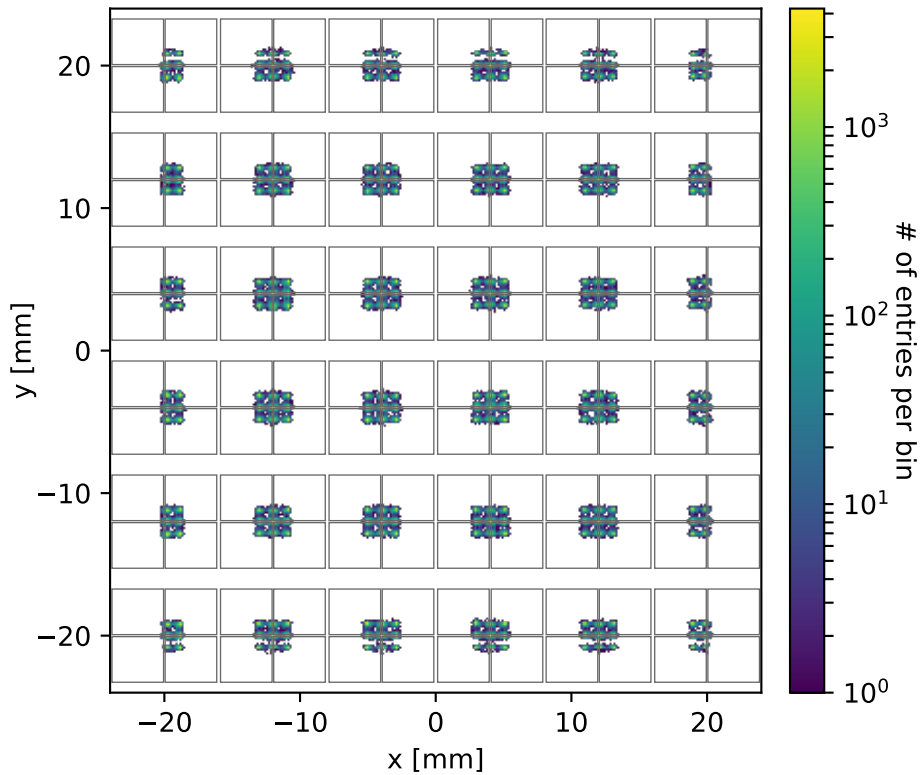


**Figure A.12:** Flood map originated from the "000"-ROI with calculated clusters of scintillation events whose identified crystal labels belong to the third layer.

### A.1.4 Optical photon counts for photopeak position

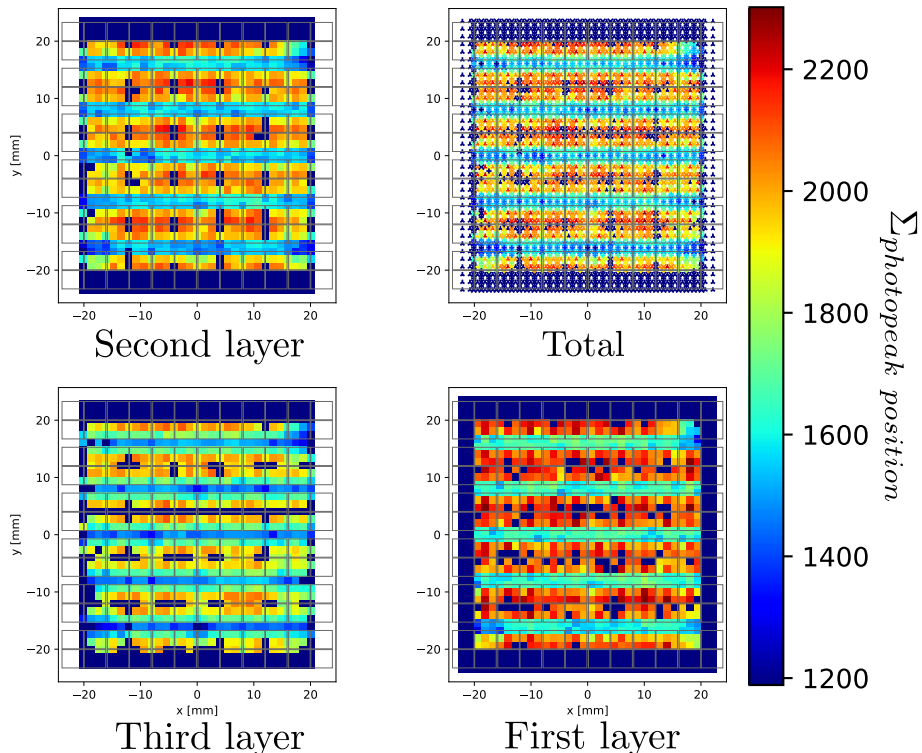


**Figure A.13:** Sum of optical photons that correspond to the photopeak position in the crystals of the three layers of the scintillator in the front irradiation measurement with coincidences configuration in "111"-ROI.

### A.1. ENLARGED FIGURES

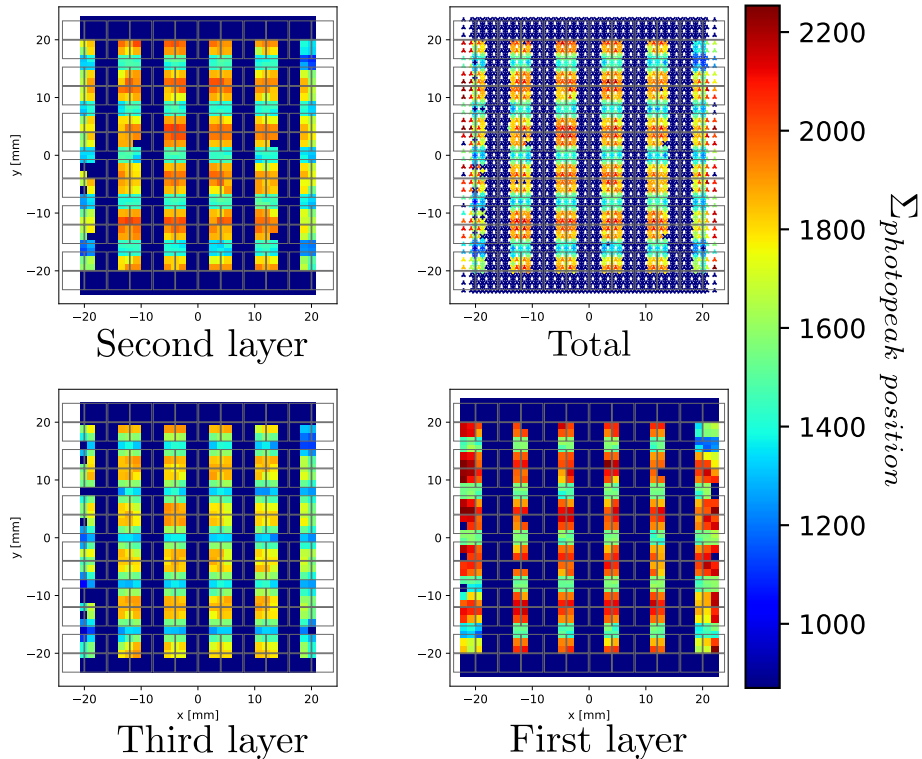


**Figure A.14:** Sum of optical photons that correspond to the photopeak position in the crystals of the three layers of the scintillator in the front irradiation measurement with coincidences configuration in "010"-ROI.

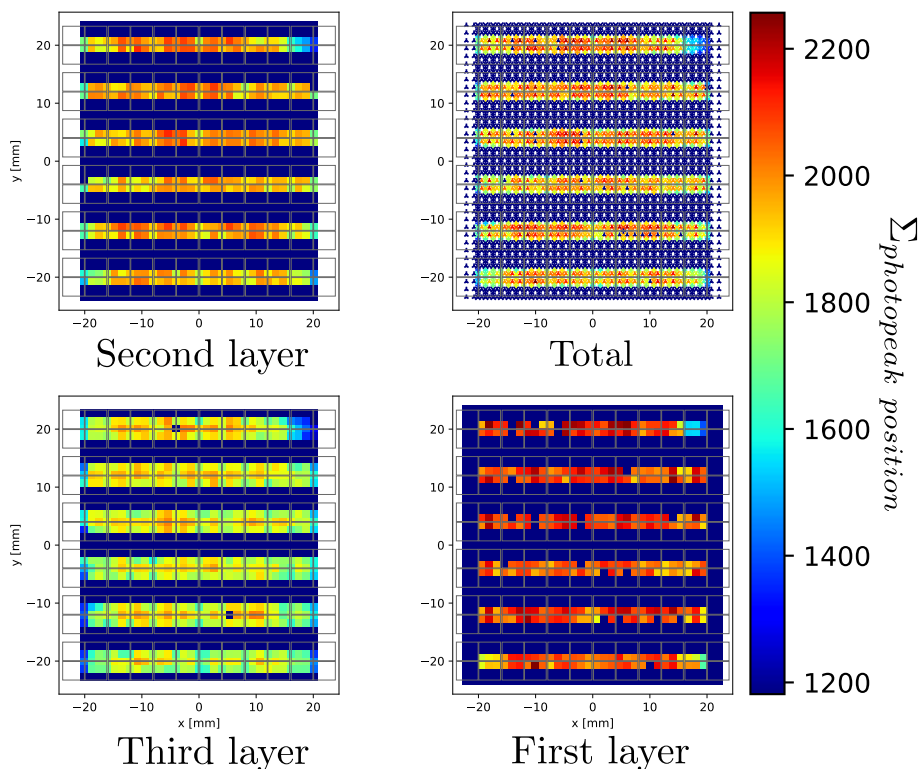


**Figure A.15:** Sum of optical photons that correspond to the photopeak position in the crystals of the three layers of the scintillator in the front irradiation measurement with coincidences configuration in "100"-ROI.

## A.1. ENLARGED FIGURES

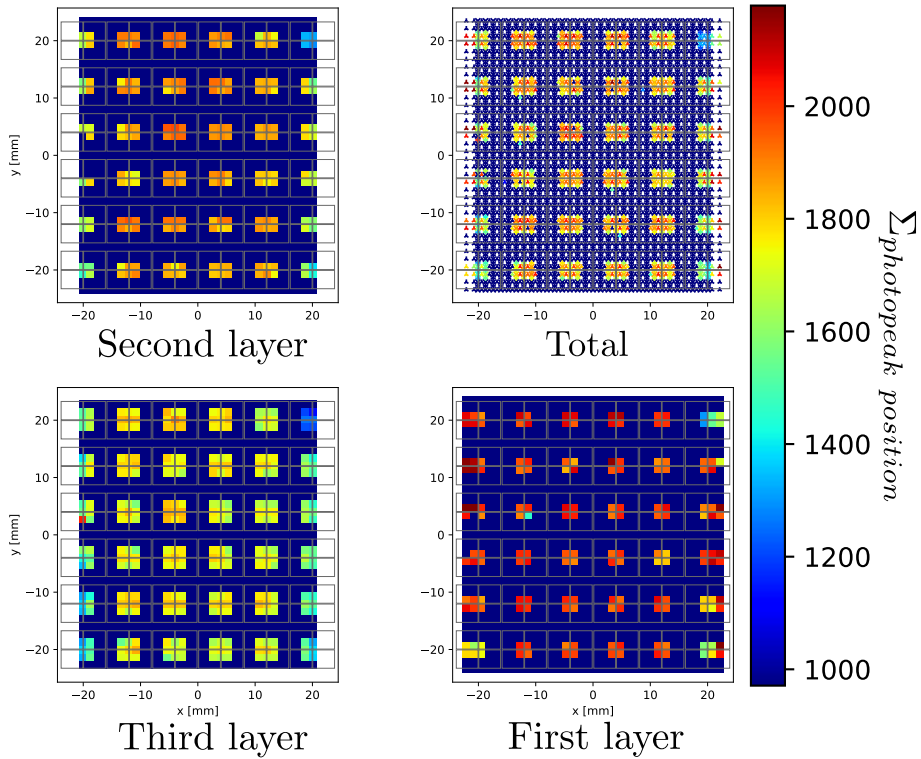


**Figure A.16:** Sum of optical photons that correspond to the photopeak position in the crystals of the three layers of the scintillator in the front irradiation measurement with coincidences configuration in "000"-ROI.